Nozzle Analysis and Heat Transfer Model for Spray Cooling of Glass Fibers

by

Matthew Sweetland

B.S., Mechanical Engineering
Purdue University, 1993

Submitted to the Department of Mechanical Engineering
in partial fulfillment of the requirements for the degree of

Master of Science in Mechanical Engineering

at the

MASSACHUSETTS INSTITUTE OF TECHNOLOGY

May 1998
[June 1998]
© Massachusetts Institute of Technology 1998. All rights reserved.

Author .....
Department of Mechanical Engineering
May 15, 1998

Certified by .....
John H. Lienhard V
Associate Professor of Mechanical Engineering
Thesis Supervisor

Accepted by .....
Ain Sonin
Chairman of Graduate Studies
Department of Mechanical Engineering

MASSACHUSETTS INSTITUTE OF TECHNOLOGY

AUG 04 1998

LIBRARIES

ARCHIVES

Nozzle Analysis and Heat Transfer Model for Spray Cooling of Glass Fibers

by

Matthew Sweetland

Submitted to the Department of Mechanical Engineering
on May 15, 1998, in partial fulfillment of the
requirements for the degree of
Master of Science in Mechanical Engineering

Abstract

Glass fibers are manufactured by forcing molten glass through a small orifice and then drawing the glass onto a spinning reel. Multiple fibers are produced by using an array of orifices in a heated bushing plate. The cooling of the glass fiber from the glass solidification temperature to room temperature is a rate limiting step in the production process. In order to increase the heat transfer from the glass fibers, a series of humidification nozzles are used to produced a water spray cloud within the fiber bundle. This increases the cooling rate through evaporative cooling.

The spray nozzles used on fiber production lines were studied using a Phase Doppler Particle Analyzer over a wide range of operating pressures. The nozzle spray clouds were characterized in terms of droplet diameter and velocity distributions. All the nozzles produce a sheath of large slower droplets around a core of small higher velocity particles. For all nozzles, the largest improvement in nozzle atomization quality is obtained between 345 kPa(50 psi) and 690 kPa(100 psi), with only a small additional improvement from 690 kPa(100 psi) to 1034 kPa(150 psi). The spray distribution beyond 5 to 10 cm from the nozzles is dominated by external air currents, regardless of injection pressure. At low pressures (< 690 $kPa/100$ psi), the Hago B-50 nozzle produces better atomization with a smaller diameter distribution than the Hago B-37 or Hago B-75. At high pressures, the diameter distribution is very similar between all the nozzles.

A theoretical model for fiber heat transfer enhancement due to spray droplets was developed using a Karman-Pohlhausen technique. The model uses a no-spray solution to the fiber velocity boundary layer as the basis for evaluating the thermal boundary layer and the spray evaporation rate. This model was combined with a radiation model and the results were used to develop a computer program that calculates the fiber temperature profile along the length of a fiber for various environmental and spray conditions. A number of simulations were run to determine the effects of changing process parameters. For a constant total spray volume, decreasing the size of the diameter distribution and increasing the droplet density will increase the cooling rate of the drawn fibers. The majority of the evaporative cooling takes place around the outer edges of the fiber boundary layer and the ambient air temperature does not affect the cooling rate of the fibers over the first 20 cm of drawing length. The additional cooling obtained from the spray is achieved over a fairly short fiber length and physical placement of the spray in the process does not make a noticeable difference in the final fiber temperature (i.e. the final fiber temperature at the surfactant applicator will be the same if the spray comes in contact with the fiber at 20 cm or at 60 cm, but both will be lower than if no spray cooling is used). The degree of spray cooling depends on the fiber configuration. Less cooling is achieved with smaller high speed fibers than for large, slow fibers. The contribution of radiative heat transfer to the cooling of the glass fibers is very small compared to the convection and spray cooling terms. This is due to small fiber surface area and very short time constants.

Thesis Supervisor: John H. Lienhard V
Title: Associate Professor of Mechanical Engineering

Acknowledgements

I would like to acknowledge and thank PPG Industries, Fiber Glass Research Center for the support and sponsoring of the research presented in this report. In particular, I want to thank Dr. R. Allen Roach and Dr. Jerome A. Burgman for their assistance and patience in answering questions and providing direction for the work.

I also want to thank Professor John H. Lienhard V for providing me with the opportunity to contribute to this project and for his help in developing this work. I also want to express my gratitude at his patience over last summer during my stay in the hospital.

Contents

List of Figures

List of Tables

Nomenclature

Symbol	Description
a	fiber radius $[m]$
$a_1,\ a_2,\ a_3$	β series expansion coefficients for small α values
A_c	nozzle flow rate parameter $[fracmlmin\ \sqrt{psi}]$
A_i	nozzle inlet port cross sectional area $[m^2]$
A_1	evaporation curve fit coefficient $[\frac{m^2}{sec\ K^2}]$
B_1	evaporation curve fit coefficient $[\frac{m^2}{sec\ K}]$
Bi	Biot number - Eqn.(4.19)
C_1	evaporation curve fit coefficient $[\frac{m^2}{sec}]$
C_D	nozzle discharge coefficient
C_D	local fiber drag coefficient - Eqn.(4.14)
C_p	air specific heat $[\frac{J}{kg\ K}]$
C_{p_f}	fiber specific heat $[\frac{J}{kg\ K}]$
C_{p_e}	air/spray mixture specific heat $[\frac{J}{kg\ K}]$
D_0	initial droplet diameter $[m]$
D	droplet diameter $[m]$
$\mathfrak{D}_{12}$	binary diffusion coefficient $[\frac{m^2}{sec}]$
F_{1-2}	radiation view factor from surface 1 to surface 2
$g_{m,1}$	mass transfer conductance $[\frac{kg}{m^2\ sec}]$
h_c	convective heat transfer coefficient $[\frac{W}{m^2\ K}]$

$\overline{h_c}$	average convective heat transfer coefficient $[\frac{W}{m^2\ K}]$
h_{fg}	latent heat of vaporization $[\frac{J}{kg}]$
k	air thermal conductivity $[\frac{W}{m\ K}]$
k_{evap}	evaporation coefficient $[\frac{m^2}{sec}]$
l	geometric dimension in radiation view factor $[m]$
L	incremental fiber length $[m]$
Le	Lewis number
m_L	nozzle mass flow rate $[\frac{kg}{sec}]$
m_w	mass of water spray per unit volume of bulk air $[kg]$
m_{H_2O}	water vapor saturation mass $[kg]$ - Eqn.(6.35)
$m_{1,s}$	mass fraction of H_2O vapor at drop surface
$m_{1,e}$	mass fraction of H_2O vapor at environmental conditions
$m_{1,r}$	reference mass fraction point - Eqn.(6.12)
$\dot{m}_{drop}$	mass of entrained air in boundary layer $[\frac{kg}{m^2\ sec}]$
$\dot{m}_f$	mass flow rate of glass $[\frac{kg}{sec}]$
$\dot{m}_{air}$	mass of entrained air in boundary layer $[\frac{kg}{sec}4]$
n_o	environmental spray density $[\frac{drops}{m^3}]$
n	boundary layer spray density $[\frac{drops}{m^3}]$
Nu	Nusselt number
p	boundary layer temperature profile coefficient
p_i	static pressure in nozzle chamber $[Pa(psi)]$

ΔP	nozzle gage pressure $[Pa(psi)]$
Pr	Prandtl number
q_c	convective heat transfer $[W]$
q_{rad}	radiative heat transfer $[W]$
$\dot{q}_e$	energy of vaporization $[\frac{W}{m^3}]$
q	boundary layer temperature profile coefficient
Q	nozzle volume flow rate $[\frac{ml}{min}]$
r	geometric dimension in radiation view factor $[m]$
R	geometric dimension in radiation view factor $[m]$
R	universal gas constant
Re	Reynolds number
R_i	nozzle inlet radius $[m]$
R_o	nozzle orifice radius $[m]$
R_{oac}	air core radius in nozzle orifice $[m]$
SMD	Sauter mean diameter of spray cloud $[m]$ - Eqn.(2.7)
t	time $[sec]$
T	boundary layer air temperature $[K]$
T_e	environmental air temperature $[K]$
T_f	fiber temperature $[K]$
T_{film}	average boundary layer film temperature $[K]$
T_p	bushing plate temperature $[K]$

T_r mass transfer reference temperature $[K]$ - Eqn.(6.13)

ΔT_f total change in fiber temperature $[K]$

$\overline{\Delta T}$ average temperature difference between fiber and environment $[K]$

u axial boundary layer velocity $[\frac{m}{sec}]$

u_o nozzle orifice axial velocity $[\frac{m}{sec}]$

U fiber velocity $[\frac{m}{sec}]$

U_e bulk air velocity $[\frac{m}{sec}]$

v radial boundary layer velocity $[\frac{m}{sec}]$

v, v_i nozzle radial liquid velocity $[\frac{m}{sec}]$

x axial distance from bushing plate $[m]$

y radial distance from fiber surface $[m]$

z_1, z_2 cell dimensions in bulk air analysis $[m]$

Greek Symbols

α velocity profile parameter

β temperature profile parameter

γ Euler's constant [.5772...]

δ velocity boundary layer thickness $[m]$ - $\left(\frac{u(y)}{U} = 0\right)$

δ_T thermal boundary layer thickness $[m]$ - $\left(\frac{\Theta}{\Theta_f} = 0\right)$

δ_{equiv} equivalent boundary layer thickness $[m]$ - Eqn.(6.32)

ϵ fiber emissivity

η dimensionless volumetric energy ratio - Eqn.(4.30)

Θ boundary layer air temperature defect $[K]$ - Eqn.(4.23)

Θ_f fiber temperature defect $[K]$ - Eqn.(4.23)

μ dynamic viscosity $[\frac{kg}{m\ sec}]$

ν kinematic viscosity $[\frac{m^2}{sec}]$

ρ air density $[\frac{kg}{m^3}]$

ρ_e combined air and spray mixture density $[\frac{kg}{m^3}]$

ρ_f fiber density $[\frac{kg}{m^3}]$

ρ_w water density $[\frac{kg}{m^3}]$

σ Stefan Boltzmann constant $[5.67 * 10^{-8}\ \frac{W}{m^2\ K^4}]$

Chapter 1

Introduction

In the glass fiber forming process, molten glass is forced through orifices in a platimun bushing plate which is electrically heated to maintain a fixed glass temperature. On small production facilities, gas pressure is used to maintain a constant glass pressure at the orifice entrance, while large high volume production stations use a constant molten glass depth to maintain a constant hydrostatic head. As the glass exits the orifice, it is pulled onto a take-up reel. This causes the molten glass to neck down until the glass solidifies at the final diameter. Initial glass temperatures at the bushing plate are around 1500 $K(2240°F)$ and the glass solidifies at 1390 $K(1860°F)$. The fiber is pulled down across a surfactant applicator and then onto a take-up reel. The fiber must be cooled below 367 $K(200°F)$ before the surfactant is applied.

Typical drawing lengths, between the bushing plate and surfactant applicator, required for adequate cooling are on the order of 1 m. Fiber diameters produced using this method vary between 5 μm and 30 μm with drawing speeds varying between 15 m/sec and 90 m/sec. The smaller fibers are generally pulled at higher velocities than the larger fibers, but the same sized fiber may be drawn at different speeds on different production stations. A production station, shown in Fig. 1.1, will have a series of orifices arrayed on a bushing plate with spacing between orifices of .6 cm to 1 cm. A bushing plate can be configured to manufacture 100 to several thousand fibers at a time depending on the fiber type and size of production station. The multiple fibers are collected into a bundle after having the surfactant applied and are then pulled onto the take-up reel.

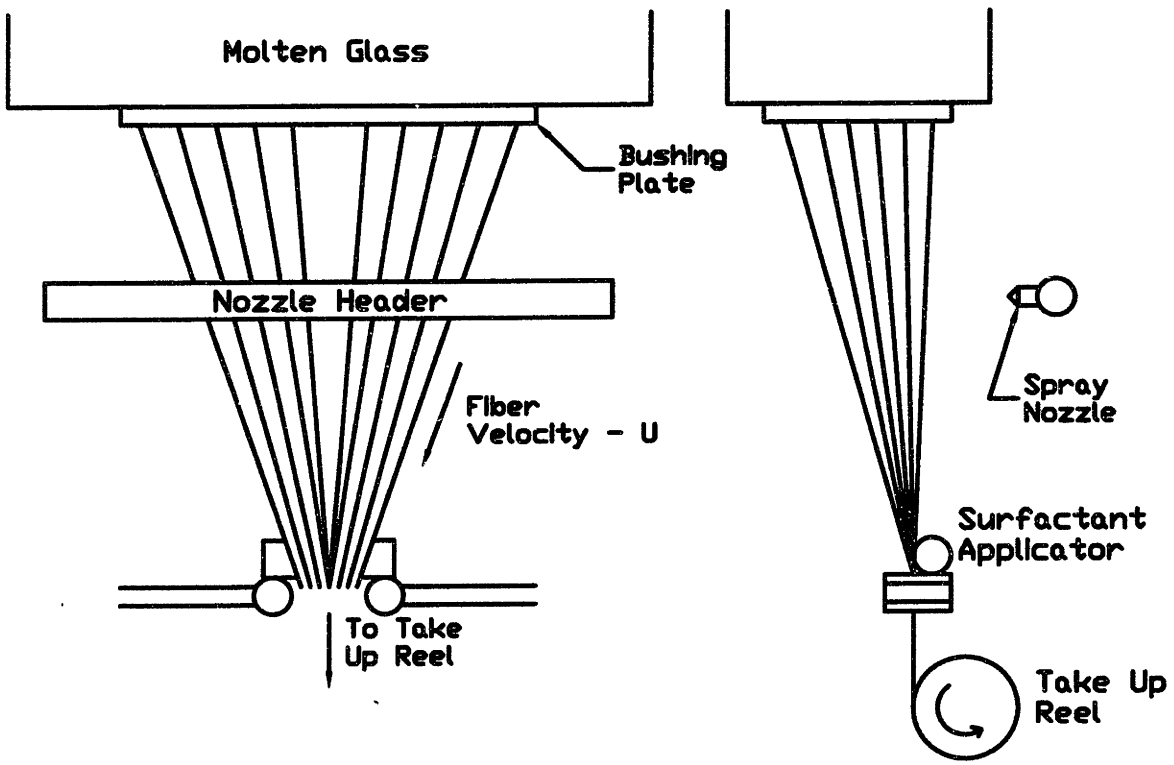

Figure 1.1: Glass fiber production station.

The fibers produced with this technique are used for a variety of purposes. The fibers are spun into fiberglass cloth for use in the automotive industry. They are used to reinforce plastics and composites. Fibers are also chopped into short sections and imbedded in epoxy to form circuit boards.

The heat transfer by convection and radiation to the environment is a major controlling factor in the production process. In order to enhance the heat transfer from the fibers, a series of humidification nozzles are set up and generate a spray cloud of water in and around the fiber bundle. Nozzle placement, number, type, and operating pressures vary between manufacturing stations and between production facilities.

A substantial amount of research has been performed on the various parts of the fiber forming process. Research on the initial drawing section where the fiber necks down and solidifies into the final diameter has received substantial attention because this area is also of interest to the fiber optics and textile industries. Some work has been performed on the evaluation of the velocity and thermal boundary layers of a long thin cylinder moving through still air. This work is mostly for lower velocity fibers ($v \sim 1 - 2\ m/sec$) and very

little has been done to quantify the effects of crossflow on the boundary layers. Some work also exists for spray cooling, but most is for the spray cooling of large heated surfaces, often involving boiling of the liquid at the surface.

The current glass-fiber facility set-ups have been developed by trial and error over many years, because no model exists to quantify the effect of all process parameters. The goal in manufacturing is to produce uniform diameter fibers at the lowest possible cost. In order to achieve this, the production rate must be high (i.e. fast drawing speeds, high heat transfer rates) while fiber breakages must be kept to a minimum. Direct experimentation on a production line has been the only means of investigating effects of process changes on production rate and quality. This is both expensive and time consuming. The present work is intended to create an alternative means of process improvement.

This thesis consists of two parts. The first section (Chapters 2-3) focuses on analysis and characterization of the nozzles used on fiber production lines. A series of nozzles are characterized based on droplet diameter and velocity distributions over a wide range of operating pressures. The second part (Chapters 4-8) of this thesis develops an analytical heat transfer model for the spray cooling of glass fibers. This model is based on a Karman-Pohlhausen technique combined with mass transfer analysis of spray evaporation. The resulting model was used to generate a computer code to determine fiber temperature as a function of distance from the bushing plate, fiber parameters (size, drawing speed, etc.), and spray conditions.

Chapter 2

Nozzle Theory and Test Equipment

This chapter covers the theoretical background of the type of nozzles used on the glass fiber production lines. An equation for nozzle flow rate is developed and a correlation for droplet diameter distribution is presented. Also covered in this chapter is a description of the equipment and procedure used to characterized the nozzles.

2.1 Theoretical Background of Spray Nozzles

The spray nozzles tested are hollow cone pressure swirl atomizers, also known as simplex nozzles. These nozzles produce a wide spray angle compared with plain orifice atomizers. Simplex nozzles impart a high angular velocity to the liquid in a swirl chamber [Fig. 2.1]. As the fluid exits the final orifice, the angular velocity causes the liquid to expand in a conical film which then breaks up into ligaments and drops. The spray development of pressure swirl atomizers has been separated into 5 stages [1]. The first two stages, the dribble stage and distorted pencil stage, are the same as spray patterns from plain orifice atomizers [Fig. 2.2]. In these stages, the flow rate is insufficient to produce any noticeable angular velocity in the exiting fluid. As the flow rate is increased, the nozzles shift into the onion stage that is characterized by a smooth film that forms a bubble before breaking up into a narrow and course spray pattern. The tulip stage produces a smooth film cone pattern which breaks up into a wide and course spray pattern. Fully developed spray

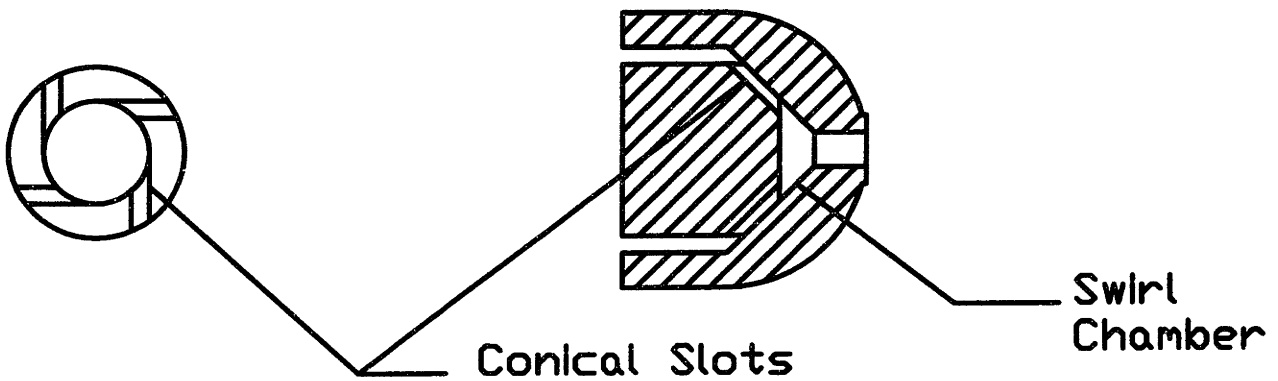

Figure 2.1: Pressure swirl atomizer.

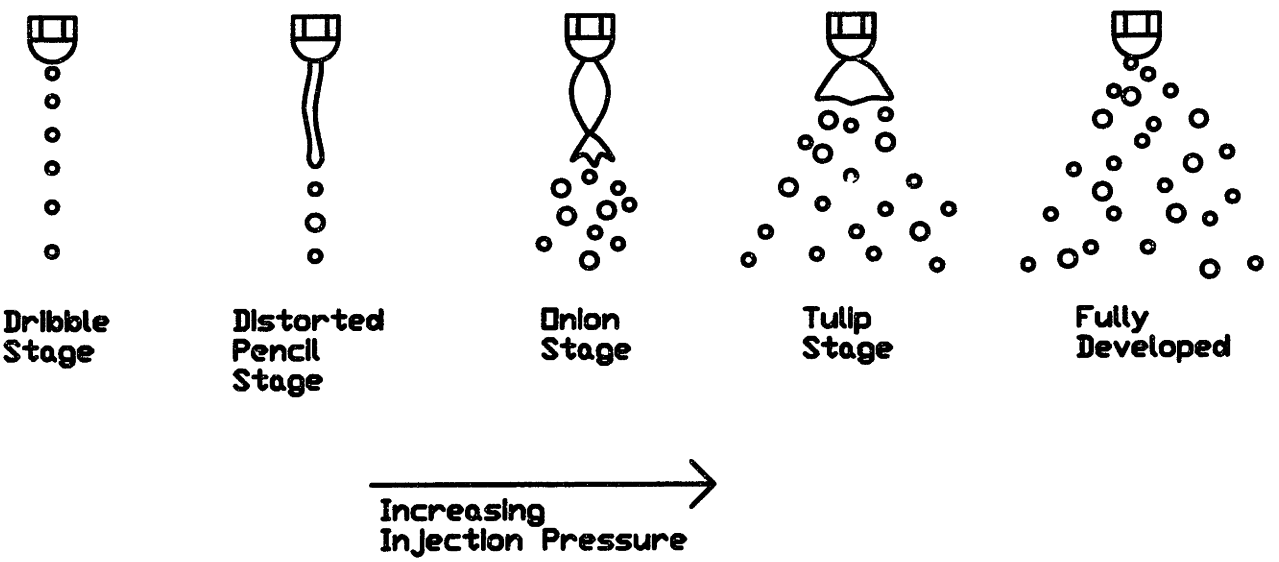

Figure 2.2: Five stages of flow through a simplex nozzle.

produces a very short break-up length and fine atomization over a prescribed cone angle.

The break up of liquid jets and liquid sheets has been studied extensively. Of main interest for simplex nozzles is the primary break up of a liquid sheet into ligaments and the secondary break up of ligament and large drops into small drops. The final diameter distribution is a strong function of break-up length. Mao and Cheuch [2] have found short break-up lengths correspond to thin film thicknesses and wide film angles. Also as injector pressure increases, the film thickness and therefore the break-up length approach a constant value. Shorter break-up lengths lead to smaller droplets and finer atomization.

Tokuoka et al. [3] have developed a good description of the general spray structure of simplex nozzles. Tokuoka et al. found the spray consists of a sheath of large drops with high momentum surrounding a core of fine drops. The trajectory angle of small drops in the sheath is less than for large drops. The decrease in mean velocity with axial distance is less in the central core than in the sheath due to entrained air.

2.2 Flow Rate and Velocity

Basic inviscid theory can be used to develop a relationship between pressure and flow rate. Figure 2.3 is a diagram of inviscid flow inside a pressure-swirl nozzle. Radial velocity is assumed negligible. The total pressure at any point in the flow can be found using Bernoulli's equation[1], and gives

$$\Delta P = \frac{1}{2}\rho_w(v^2 + u^2) + p_i = constant \tag{2.1}$$

where ρ_w is the liquid density, v is the tangential velocity component of the flow, u is the axial component of the flow, p_i is the static pressure, and ΔP is the injection gage pressure. Conservation of angular momentum yields

$$vR = v_i R_i \tag{2.2}$$

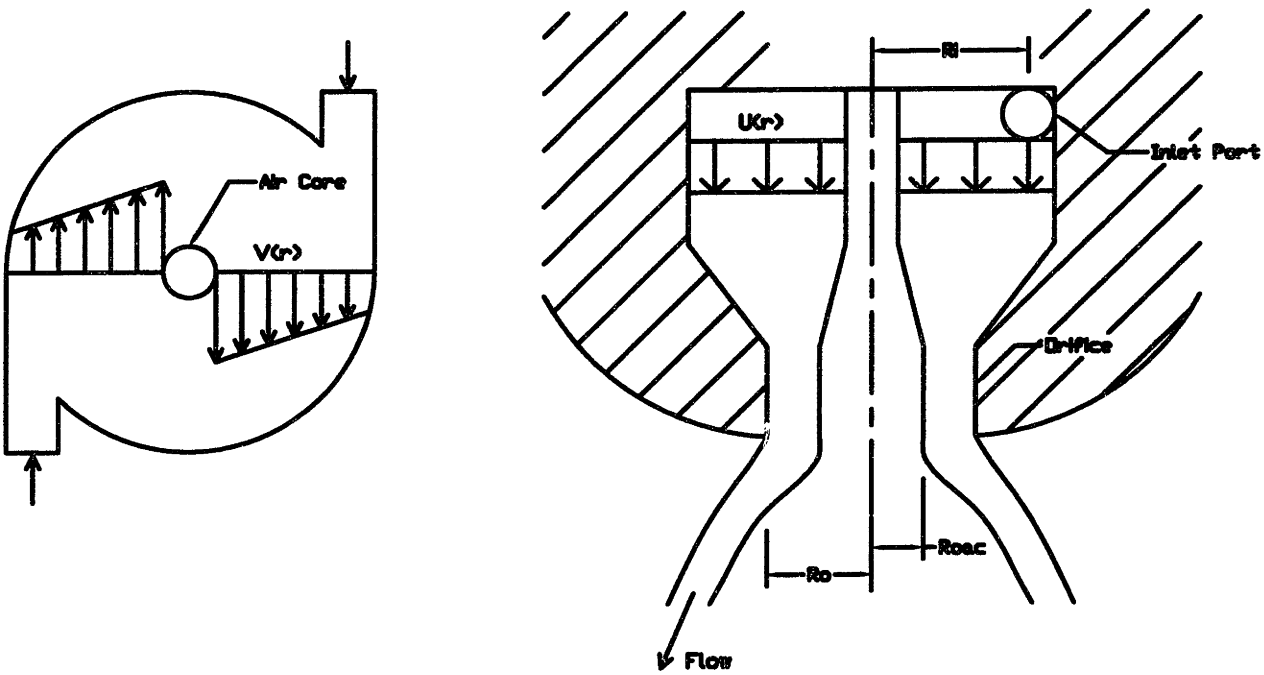

Figure 2.3: Inviscid flow in pressure-swirl atomizer.

where v_i is the inlet port velocity at an inlet radius of R_i. An air core develops at the center of the nozzle, otherwise as R approaches zero the tangential velocity, v, would become infinite. For inviscid flow, u is uniform with radius and mass conservation across the orifice can be written as

$$Q = \pi u_o (R_o^2 - R_{oac}^2) \tag{2.3}$$

where Q is the volume flow rate, u_o is the orifice axial velocity, R_o is the orifice radius, and R_{oac} is the radius of the air core in the orifice. Defining a discharge coefficient, C_D such that

$$Q = \pi C_D R_o^2 \sqrt{\frac{2\Delta P}{\rho_w}} \tag{2.4}$$

and assuming the air core is at atmospheric pressure, equation (2.1) can be expanded to

$$\frac{\rho_w Q^2}{2\pi^2(R_o^2 - R_{oac}^2)^2} + \frac{\rho_w Q^2 R_i^2}{2A_i^2 R_{oac}^2} = \Delta P \tag{2.5}$$

where A_i is the inlet port cross sectional area. This equation can be solved by making the additional assumption that for any injection gage pressure ΔP, the resulting air core radius will yield the maximum flow rate[4]. This assumption can be satisfied by solving equation (2.5) for Q and setting $\partial Q/\partial R_{oac} = 0$. From this, it can be shown that C_D is independent of pressure and that it is a function of nozzle geometry only. Equation (2.3) can then be rewritten as

$$Q = A_c\sqrt{\Delta P} \tag{2.6}$$

for an incompressible liquid, where A_c is a constant dependent on the specific nozzle type.

The flow rate does not increase linearly with axial velocity due to two competing effects. As the injection pressure is increased, the axial velocity increases, but the cross sectional flow area decreases. This is due to the tangential velocity in the nozzle increasing along with the axial velocity. As the tangential velocity of the water increases, the size of the air core in the nozzle orifice also increases and the cross sectional area of fluid flow decreases.

2.3 Diameter

The primary goal in the analysis of spray data is to obtain information necessary for a heat transfer model of the glass fiber production process. For this reason, the most applicable representative droplet diameter used to describe the droplet distribution is the Sauter mean diameter (SMD). The SMD is the diameter of a droplet with the same surface area to volume ratio as the entire spray cloud. This diameter can be calculated from [1]

$$SMD = \frac{\sum n_i D_i^3}{\sum n_i D_i^2} \tag{2.7}$$

where n_i is the drop count in the bin with average diameter D_i. The evaporation rate from a spray cloud is based on total surface area of the spray drops, and the SMD is an easy and explicit input into evaporation equations.

Several empirical equations for the SMD of a pressure swirl atomizer have been established. One of the first proposed was [1]

$$SMD = 7.3\sigma^{.6}\nu_L^{.2}m_L^{.25}\Delta P^{-.4} \tag{2.8}$$

where σ is the fluid surface tension, ν_L is the liquid kinematic viscosity, m_L is the nozzle mass flow rate in kg/sec, and ΔP is the injection pressure in Pa. Most of the more recent correlations have been with hydrocarbon fluids and higher flow rate nozzles in the range of 2 to 10 gallons per hour, vs. .5 to 1 gallon per hour nozzles used in the glass forming process. One immediate problem with SMD correlations is the variation in SMD across the spray cloud. Depending on where a measurement is taken, the SMD can vary by an order of magnitude for the same nozzle. A spray cloud averaged SMD can be obtained, but this is very time consuming and inefficient, and this number may still not represent the portion of the spray that is active in the process. Correlations are useful to see how general trends in the spray should react, but cannot be used to evaluate specific values at specific points.

2.4 Equipment

2.4.1 Test Chamber

The test apparatus for measuring the parameters of the PPG cooling nozzles was designed to simulate operating conditions of the production facility. The primary measurement tool is a Phase Doppler Particle Analyzer (PDPA) manufactured by Aerometrics Inc. Due to precise focusing requirements of the PDPA, the system was designed to move the spray nozzle through the field of the stationary PDPA. The size of the test chamber was limited by the optics of the PDPA and the length of an available linear rail system. Output from the PDPA is optimized by using forward scatter and a 30° offset angle between the transmitter and detector. The PDPA is mounted on a 24" by 48" optical table to aid in alignment and focusing, and to limit signal degradation due to thermal expansion of the mounting base during operation. The optical table is mounted on four cork/rubber anti-vibration pads.

The nozzle traverse and test chamber (Fig. 2.4) are mounted on a transverse rail to allow motion perpendicular to the PDPA axis. The rail system is driven by a variable speed DC motor mounted to a lead screw. The system is capable of 44" of motion. Unlike most test chambers, the nozzle is mounted with a horizontal spray axis to preserve the effects of gravity present in PPG facilities. The nozzle rail is mounted to an X-Y traversing table that provides motion of the nozzle in a vertical plane. This system permits full motion of the spray around the PDPA measurement volume. The X-Y positions are controlled by hand cranks attached to 10 tpi lead screws. Positions in all three axes are measured relative to the PDPA measurement volume and are repeatable to ± 1 mm.

The test chamber is constructed with 1/2" plexiglass sides. This provides a wide viewing area into the chamber while protecting the electronics and optics from water spray. Thick plexiglass was used to avoid warping and bending of the sides which would cause the detector to lose focus with the measurement point. The internal dimensions of the chamber are 32" vertical by 36" horizontal. The base of the test chamber is a 3" deep aluminum pan for water collection. The chamber at the nozzle end is left open to the atmosphere to allow for air entrainment by the nozzle. The other end of the chamber is also left open to the atmosphere, but a sheet of lexan is placed at a slight angle to the horizontal with its base in the aluminum pan. This

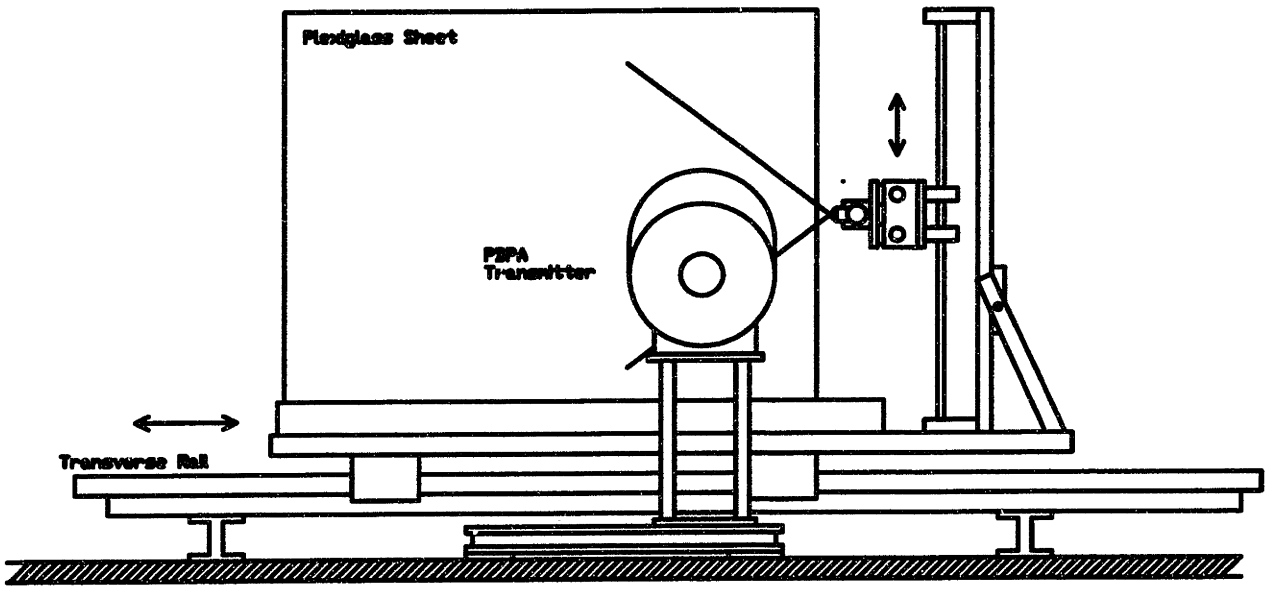

Figure 2.4: Side view of test chamber with flow loop removed.

allows for entrained air to escape the test chamber, but catches most of the spray overshoot and returns it to the collection pan. The top of the chamber, a sheet of 1/8" lexan, is unattached and easily removed. The plexiglass and lexan sides are supported by a steel framework constructed from Dexion angle bracket.

2.4.2 Flow Loop

The flow loop (Fig. 2.5) is a closed circuit designed which covers a wide range of operating conditions, from low pressure single nozzle operation to high pressure multiple nozzle flow. Water is stored in two 50 gallon reservoirs that feed into a common supply header for the pump. The pump is a gear pump powered by a 1 1/2 h.p., 230 VAC electric motor capable of pumping 5 gpm at 100 psi. Pump speed is fixed, so the flow rate is controlled via a bypass line from the pump exit to the pump intake. Pump pressure pulsations are reduced using a 20 gallon surge tank. The tank has an independent air supply line to vary the degree of capacitance. The flow is passed through two particle filters to remove contaminants before being piped to the nozzle header. Flow rate is measured using a rotameter accurate to $\pm$ 2.2 cc/min ($\pm$.034 GPH). A pressure gauge ($\pm$11 kPa/1.6 psi) and dial thermometer ($\pm 1.1°C/2°F$) are mounted directly to the nozzle header. The high pressure system is constructed from 3/4" schedule 80 PVC pipe. Flow is returned to the

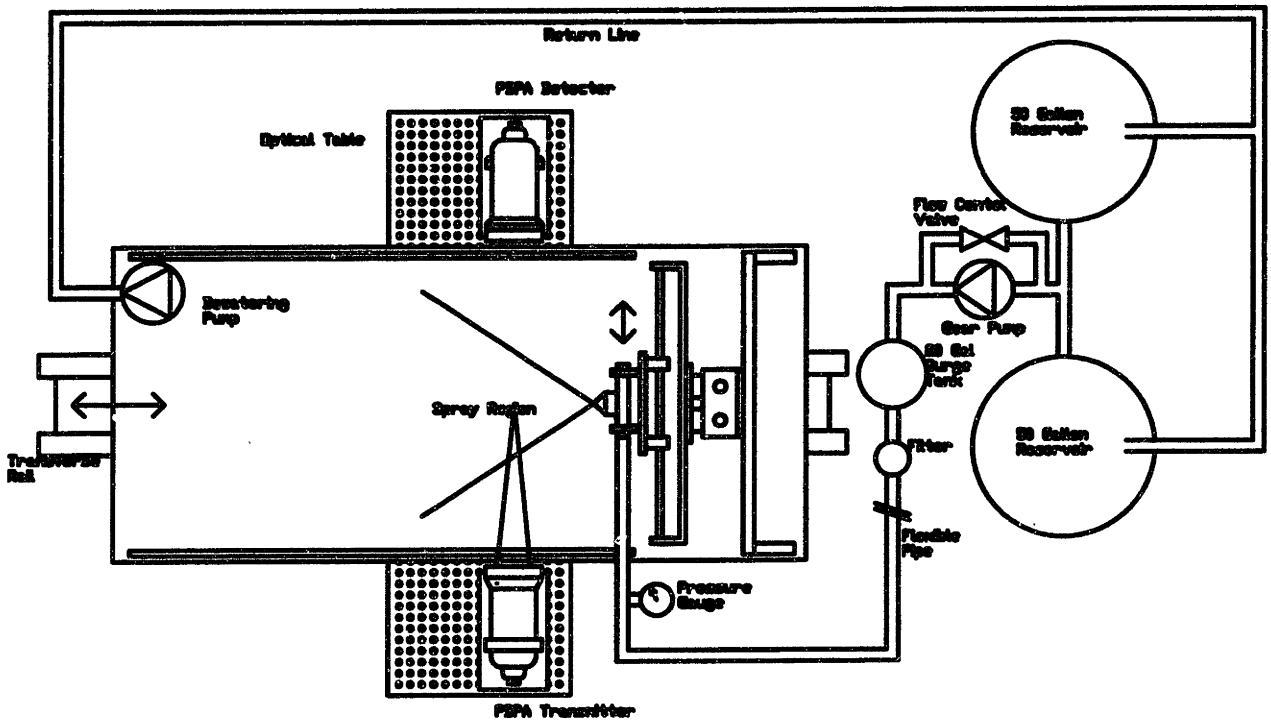

Figure 2.5: Test chamber and flow loop.

reservoirs from the collection pan by a high volume, low pressure sump pump that is capable of pumping down to a 1/8" water depth.

2.4.3 Phase Doppler Particle Analyzer

The PDPA can be used for simultaneous measurements of particle size and velocity. An interference fringe pattern is produced by intersecting laser beams. When a particle traverses this pattern, refracted light produces a signal in the photomultiplier tubes. By measuring the frequency of the received signal and knowing the fringe pattern spacing from the laser wavelength, the particle velocity can be calculated. With the use of multiple detectors (three photomultiplier tubes) with fixed spacing, the phase shift of a particle signal from one detector to another can be used to calculate particle size. This calculation can be done with only two detectors, but by using three detectors, two separate size calculations can be made and compared. If the two values do not match, the signal is rejected. Accuracy of the diameter measurement varies with the optical set-up of the system and the range of particle diameters being measured.

The PDPA is a single particle measurement device. This means only one particle can be in the measurement volume at any one time for the measurement to be valid. Edwards and Marx [5] have described this restriction as a pair of Poisson filters acting on the data. The data point will be rejected if the particle spacing is sufficiently small that two particle are in the measurement volume at the same time. Also, the data point will be rejected if a particle in the measurement volume does not exit the space before another particle with a different velocity enters. These two effects cause increasing errors in the PDPA measurement of volume flux and particle density with increasing particle density and increasing particle velocity range. The actual measurement volume of the system varies depending on the particle size. Smaller particles must transit closer to the center of the measurement volume to produce a detectable signal. The combination of these effects can lead to large errors in volume flux and particle density calculations. Software algorithms attempt to correct for these effects, but become substantially less effective with increasing droplet density. It is important to note however, that as particle density and volume flux increase, the errors in diameter and velocity measurements do not change. While the number of rejections increase, as long as a sufficient number of valid samples are obtained, the diameter and velocity distributions will be correct. A final restriction on the PDPA is that the particles must be spherical for accurate size calculations. This leads to data rejection in regions of high velocity gradients where the drops are distorted by aerodynamic forces.

The requirement of knowing the exact spacing from the measurement volume to the detectors for particle size measurements necessitates precise focusing of the detector on the measurement point. Loss of focus on this point will result in lost and incorrect data. For this reason, quality control of the received signal is critical. The two primary means of checking the data are through software monitoring of data rejection flags and by monitoring the data signals on oscilloscopes. The system software provides automatic monitoring of data validations as well as cumulative information of data rejections. If the detector is out of focus, the majority of data rejections will be due to excessive phase discrepancies between the multiple detectors. Data quality can also be monitored by observing the raw and processed signals from each photomultiplier tube on oscilloscopes. Two dual channel scopes are used in this set-up. One is a 60 MHz analog scope and the other is a 100 MHz digital scope. Signals from two separate photomultiplier tubes can be displayed on each screen and compared. The signals (both raw and processed) between detectors should have matching shapes

with a phase shift. Large variations in shape or magnitude are good indicators that the detector is out of focus. A full analysis of the errors in droplet diameter and droplet velocity are covered in the nozzle results sections. Droplet diameter results are in Section 3.2.1 and the droplet velocity results are in Section 3.2.2.

2.5 Experimental Procedure

The spray pattern of the Hago B-50 nozzle was analyzed by looking at vertical planes normal to the spray direction for operating pressures from 345 kPa(50 psi) to 1034 kPa(150 psi). Measurements were made on a 1 cm grid within each plane, at 5 cm intervals from the nozzle exit. The grid was expanded from the nozzle centerline in each plane until the data points obtained had either a negative average velocity, or the data rate was below 1000 points in three minutes. The negative average velocity corresponded to points below the nozzle axis where the flow was recirculating. Low data rate corresponded to the top and outer edges of the spray cone. At each plane, the spray was measured over the full vertical distance, but only across half the horizontal distance (from nozzle centerline to one outer edge). The spray distribution is assumed to be symmetrical on the horizontal axis, but not on the vertical axis owing to the effect of gravity.

Only a partial characterization was performed on the Hago B-37 and Hago B-75 nozzles, for use as a basic comparison tool. Data on the Hago B-37 and Hago B-75 was taken at four positions in the spray cloud, for pressures ranging from 276 kPa (40 psi) to 1034 kPa (150 psi). The positions where data was obtained were on the nozzle centerline 5 cm from the nozzle, on the nozzle centerline 20 cm from the nozzle, in the plane of the nozzle at a 5 cm axial distance and 5 cm horizontally from the nozzle centerline, and in the plane of the nozzle at a 20 cm axial distance and 15 cm below the nozzle centerline.

Water was supplied from the surge tank by applying compressed air at a set pressure. The pump was used for initially charging the tank with water. This method completely eliminated pressure pulsations from operating with the pump. Water temperature and pressure were measured at the nozzle header. Room temperature remained constant at $22°C(72°F)$, but the relative humidity varied with atmospheric conditions. Ambient temperature ($\pm.6°C/1°F$) and relative humidity ($\pm 3\%$ in 20-90% range at $25°C$) were measured with an Omega digital thermo-hygrometer (model RH-411).

Initial investigations of the spray yielded optimal settings for the PDPA. For the fixed transmitter and receiver spacing, best results for the B-50 nozzles were obtain with the largest laser intersection angle and an imposed velocity offset on the fringe pattern of 5 m/sec. The PDPA is limited by a 35:1 maximum to minimum diameter ratio so the measurement range was varied to accommodate the spray distribution at each point. Near the nozzle centerline, the spray distribution was dominated by small, high velocity particles so the maximum diameter was reduced to include these particles. Away from the nozzle centerline, the spray distribution shifted to larger particles and the maximum diameter was increased. At all points, the sample range was shifted to include the largest occurring droplets, even if this resulted in losing some small particle data. Lewis et al. [6] have shown that the exclusion of one large drop in 1000 samples may affect the average diameter by as much as 100%, therefore the inclusion of large drops is important for accurate spray distribution information.

Upon initial investigation of these nozzles, a problem was encountered with corrosion and rust deposits in the nozzle passages. This problem was reduced by adding a second particle filter to the flow loop and installing a flow bypass line that allowed for easy flushing of the entire system before use each day. While this reduced the corrosion problem, the nozzles still tended to accumulate rust and scale deposits within a couple day's time. These deposits severely altered the flow pattern of the nozzle and made repeatability virtually impossible. This issue was addressed by changing to a new nozzle when a change in spray pattern became evident. Changes could often be seen in a visual inspection of the spray cone, specifically the liquid film next to the nozzle exit, but an additional check was made each day by repeating points from the previous day's run and comparing values.

Chapter 3

Nozzle Characterization Results

This chapter presents and discusses the results from the nozzle investigation. It starts with a description of the general spray structure of the B-50 nozzle. It then goes on to cover a full spatial description of the droplet diameter and velocity distributions for the B-50 nozzle at 345 kPa(50 psi), 690 kPa(100 psi), and 965 kPa(140 psi). Finally, a basic description of the Hago B-37 and Hago B-75 spray structures is compared to the Hago B-50 results.

3.1 Hago B-50

3.1.1 General Spray Structure

The general spray structure of the spray nozzles was investigated by using a video camera to look at vertical and horizontal planes within the spray clouds. The images in the video were obtained by diluting a small amount of flourescein, sodium salt in the water supply. A 3 *watt* argon laser was used to create a light sheet that illuminated the droplets in a given plane. The laser was positioned 1.5 m from the test cell and the beam was passed through two half cylindrical lenses to produce a flat sheet, 4 mm thick. One side of the test chamber was removed to permit an unobstructed view of the flow field. The laser sheet was aligned with the nozzle centerline and could be rotated from a vertical plane to a horizontal plane by rotating the cylindrical lenses by 90°.

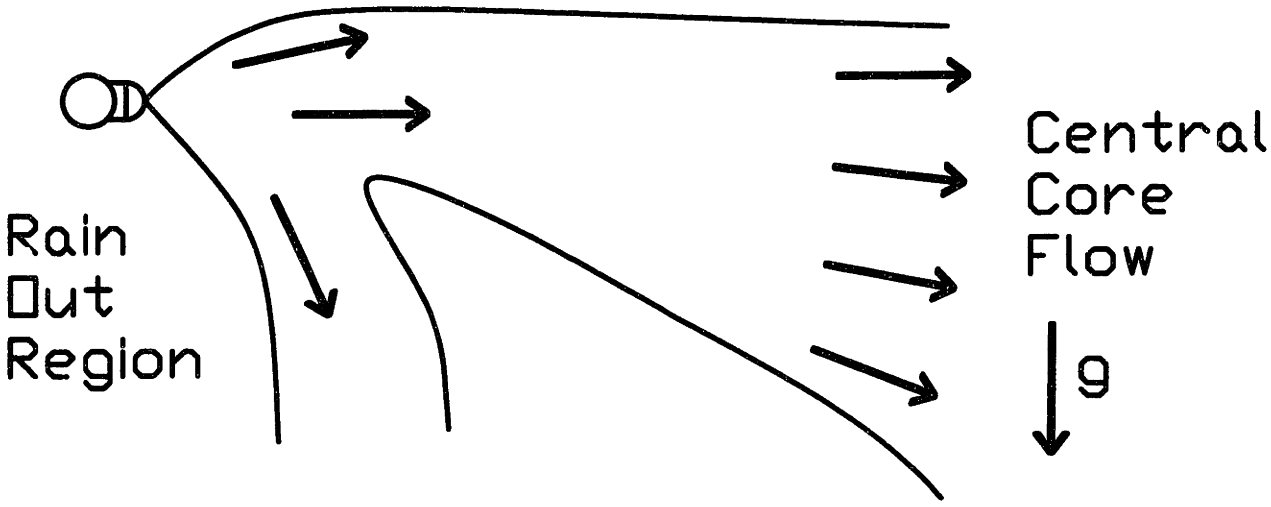

Figure 3.1: Spray structure for Hago nozzles.

The cloud was found to consist of a central high velocity core that projects horizontally out from the nozzle and a region of flow where a large portion of the droplets have little horizontal velocity and rain out of the flow (Fig. 3.1). The most interesting information obtained from the flow visualization was the effect of external disturbances on the spray cloud. The disturbance itself was fairly small, but the effect on the spray cloud was quite large. The disturbance consisted of an individual blowing on the spray cloud from approximately 1 m away. The external disturbance would completely shift the flow field at all pressures. Vertical plane video showed how close to the nozzle the disturbance had an effect. As pressure was increased, the region unaffected by the disturbance became somewhat larger, but the majority of the flow was still disrupted. The most noticeable change with increasing pressure was the reduction in time required for the flow to return to normal once the disturbance was stopped. The horizontal plane video demonstrated that the flow was not completely shattered by the external disturbances, but that the flow was shifted to the far side of the test chamber. With this large sensitivity to a fairly small disturbance, it is obvious that the central core flow will be dominated by external air currents in any practical situation. In particular, fiber induced air flow will entirely govern the dispersion of droplets in fiber forming stations.

3.1.2 Diameter and Velocity Evolution

Figures 3.2, 3.3, and 3.4 show the evolution of droplet size distributions with distance from the B-50 nozzle for operating pressures of 345 kPa(50 psi), 690 kPa(100 psi), and 965 kPa(140 psi). Figures 3.5, 3.6, and 3.7 show the evolution of droplet axial velocity with distance from the B-50 nozzle for operating pressures of 345 kPa(50 psi), 690 kPa(100 psi), and 965 kPa(140 psi). For all three operating pressures, the diameter and velocity ranges flatten out with increasing distance from the nozzle. At 345 kPa(50 psi), the spray cloud completely disintegrates beyond 20 cm from the nozzle and repeatable measurements are impossible to obtain. The rain out can be seen in the 690 kPa (Fig. 3.3) and 965 kPa (Fig. 3.4) plots around the 15 cm and 20 cm positions. The plots become extended in the vertical direction with the majority of the spray in the lower regions having a SMD in the 70 to 80 μm range with little or no horizontal velocity component.

The B-50 nozzle produces a sheath of larger slow droplets around a central core of small high velocity drops. This general structure remains unchanged for all pressures. As pressure increases, the maximum velocity measured along the nozzle centerline increases and the size distribution becomes more uniform with decreasing SMD. The effect of increasing pressure on the size distribution in the primary rain out region is small. Increasing the injection pressure increases the depth of penetration into still air for the spray cloud, but the spray is still largely dominated by the external air currents beyond 5 to 10 cm from the nozzle.

3.1.3 Nozzle Consistency and Repeatability

Ten B-50 nozzles were chosen at random and tested to determine the consistency of different nozzles. Diameter and velocity data was obtain for the B-50 nozzle at multiple points in each plane and the average values and standard deviations for the ten nozzles are presented in Table 3.1.

Figure 3.8 plots the diameter and velocity values and their standard deviations for the B-50 on the nozzle centerline at 345 kPa(50 psi). As the axial distance from the nozzle increased, the standard deviation of the SMD increased, but the standard deviation of the velocity decreased.

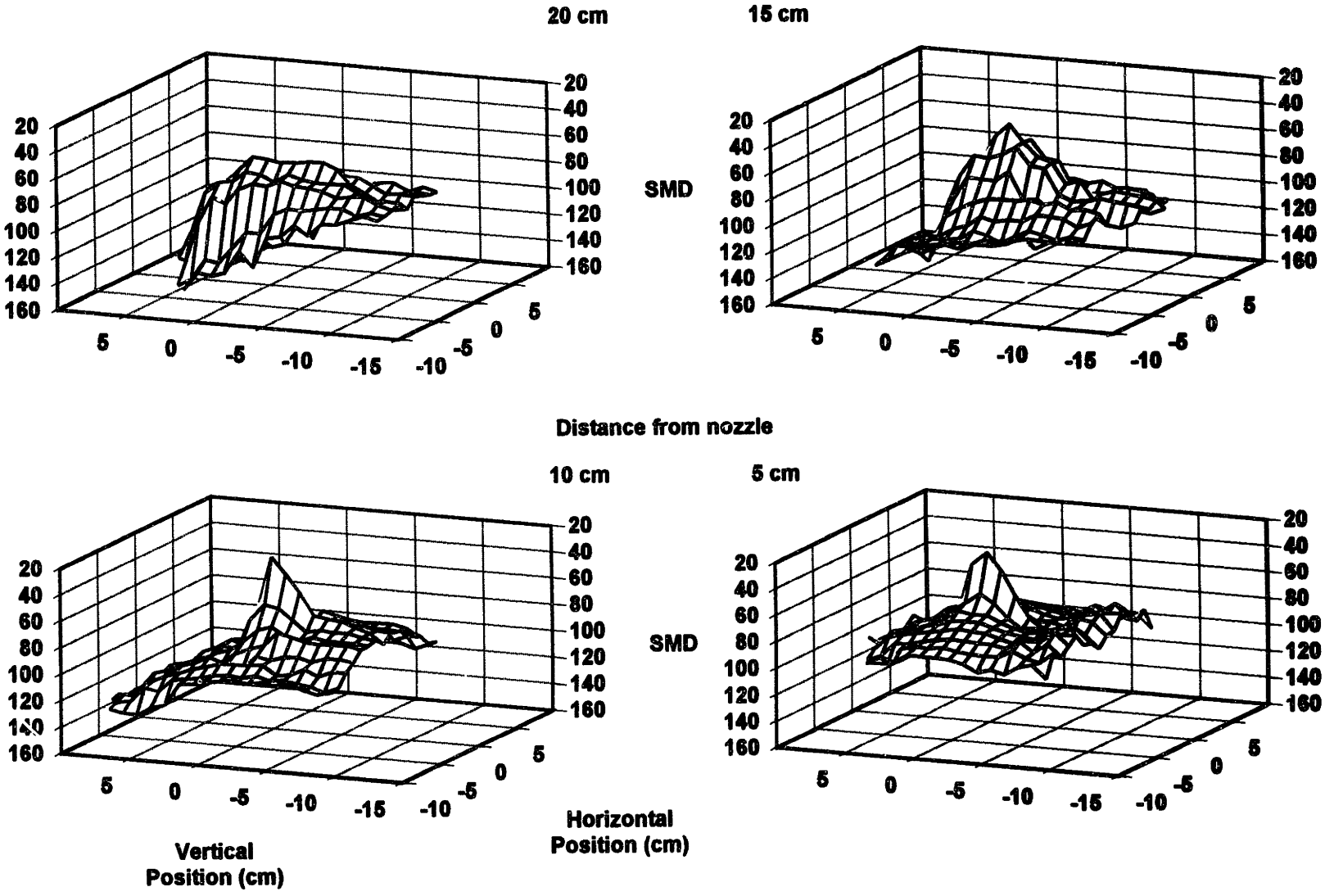

Figure 3.2: Hago B-50 at 345 *kPa*(50 *psi*). SMD evolution with distance from nozzle.

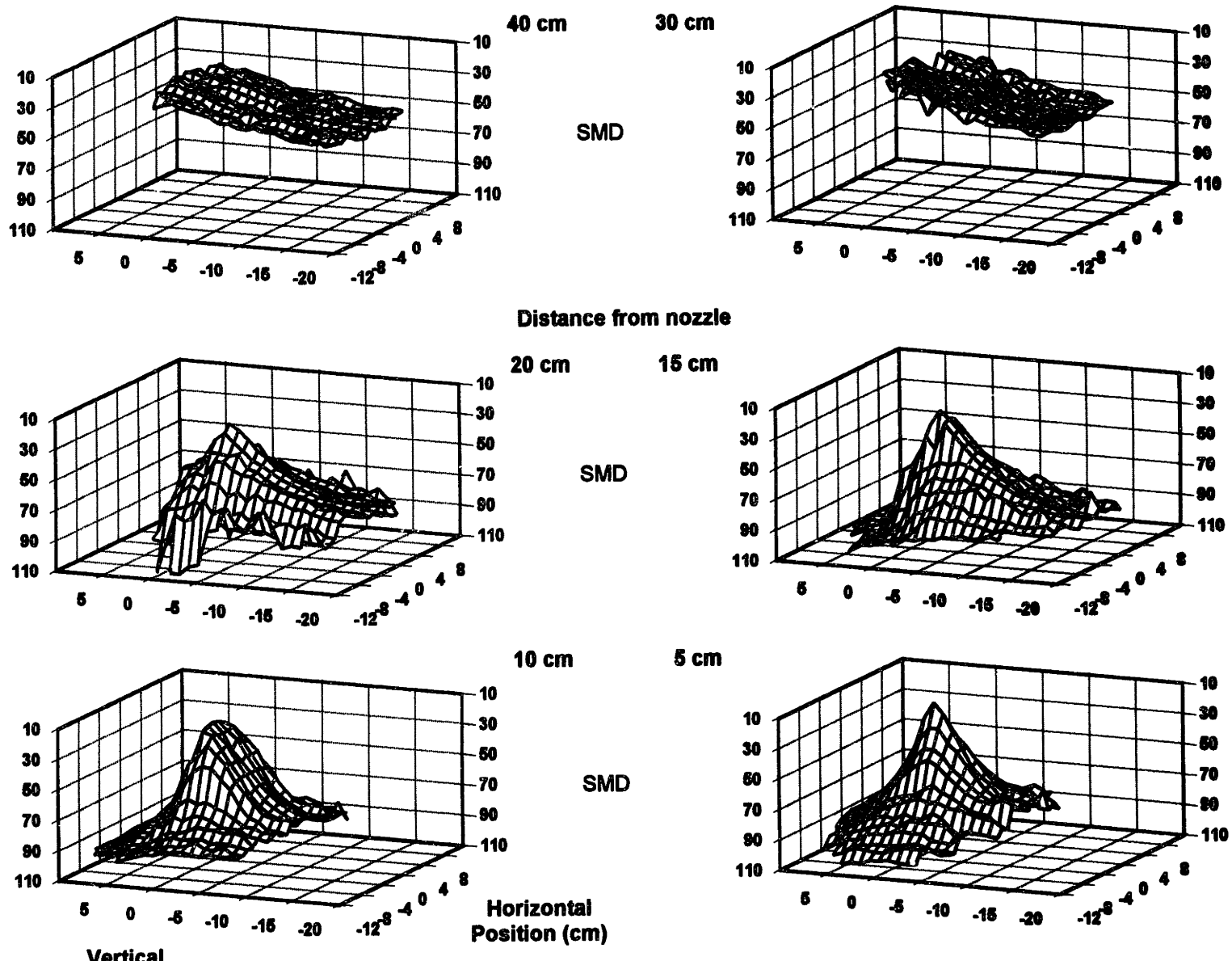

Figure 3.3: Hago B-50 at 690 *kPa*(100 *psi*). SMD evolution with distance from nozzle.

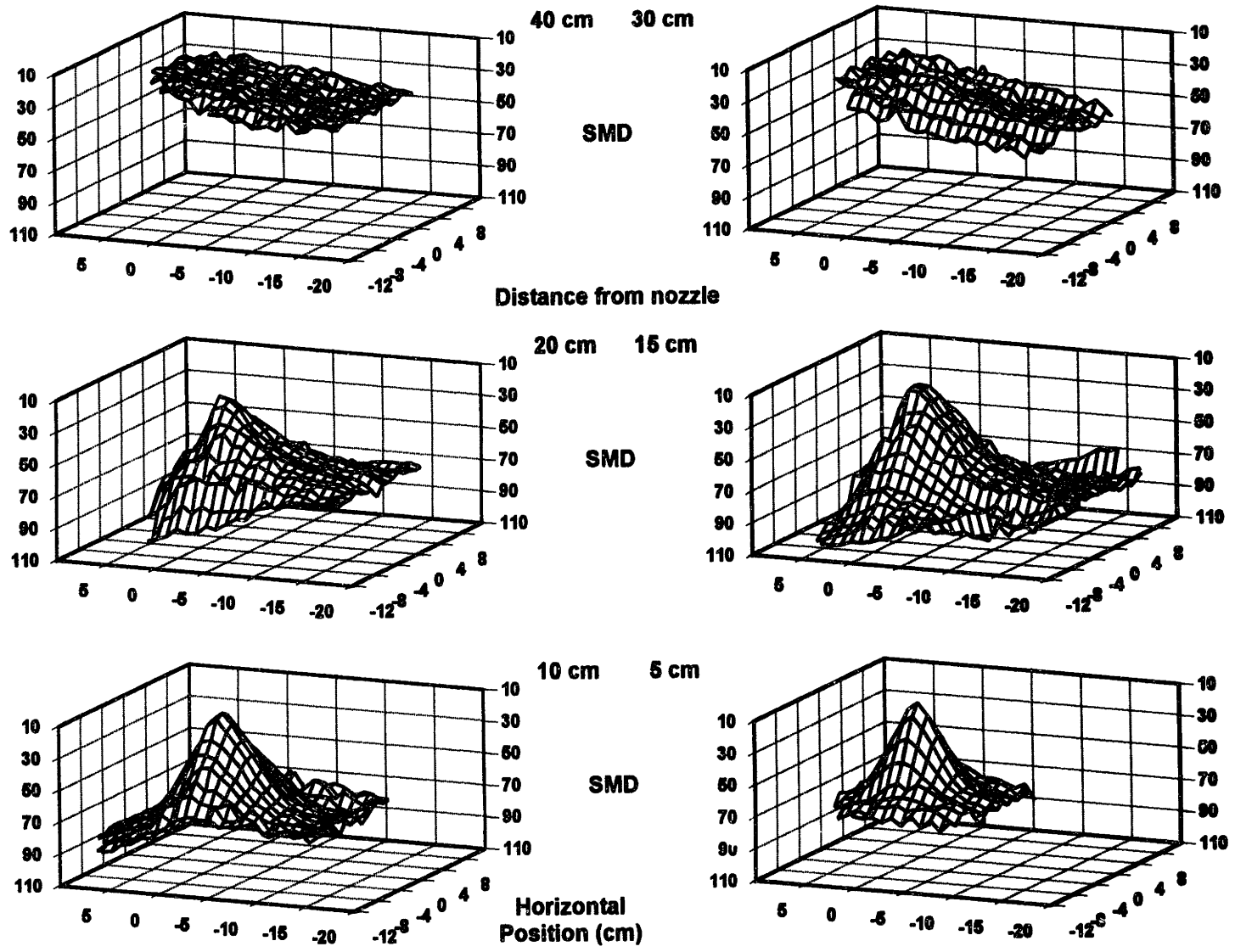

Figure 3.4: Hago B-50 at 965 *kPa*(140 *psi*). SMD evolution with distance from nozzle.

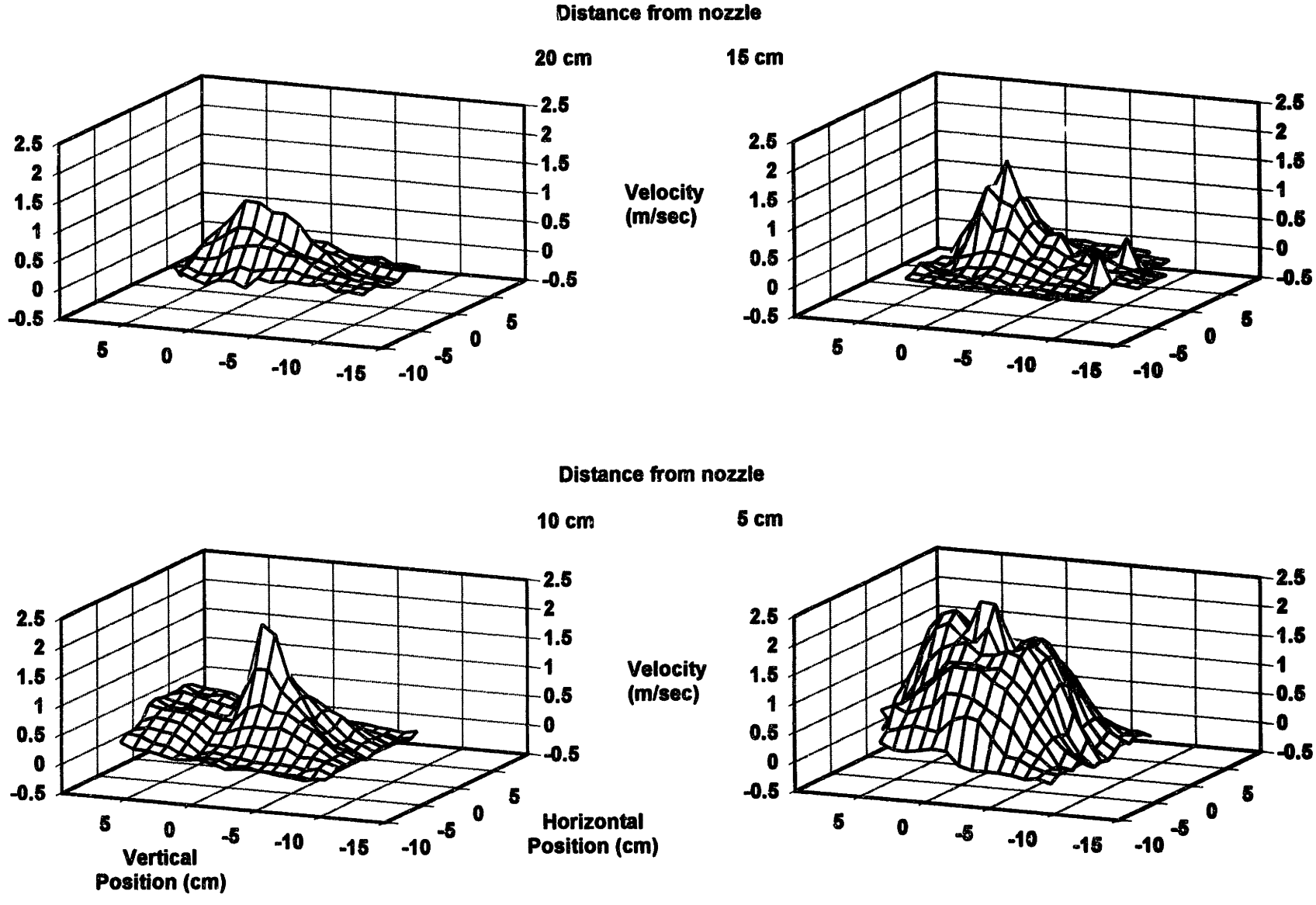

Figure 3.5: Hago B-50 at 345 *kPa*(50 *psi*). Velocity evolution with distance from nozzle.

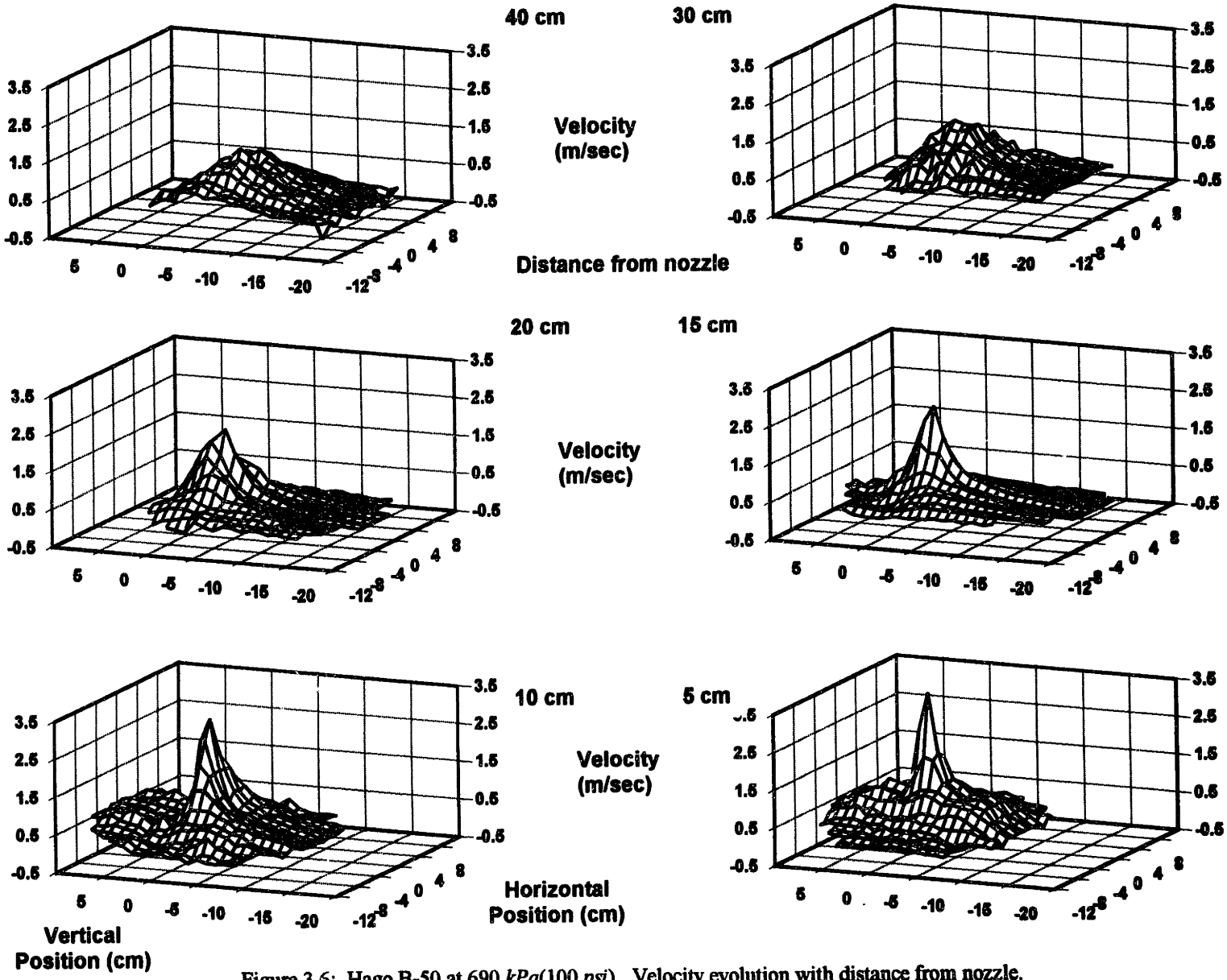

Figure 3.6: Hago B-50 at 690 *kPa*(100 *psi*). Velocity evolution with distance from nozzle.

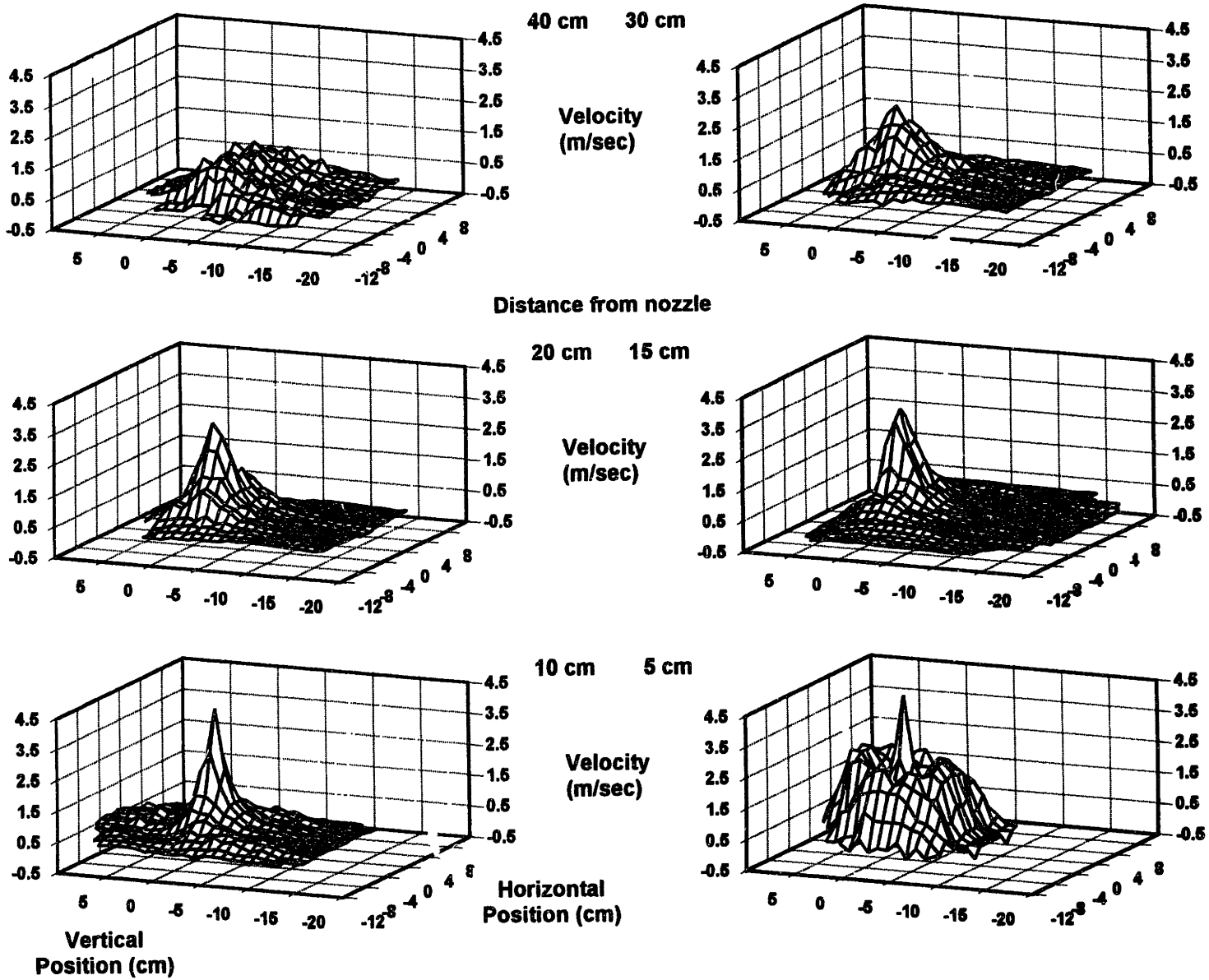

Figure 3.7: Hago B-50 at 965 *kPa*(140 *psi*). Velocity evolution with distance from nozzle.

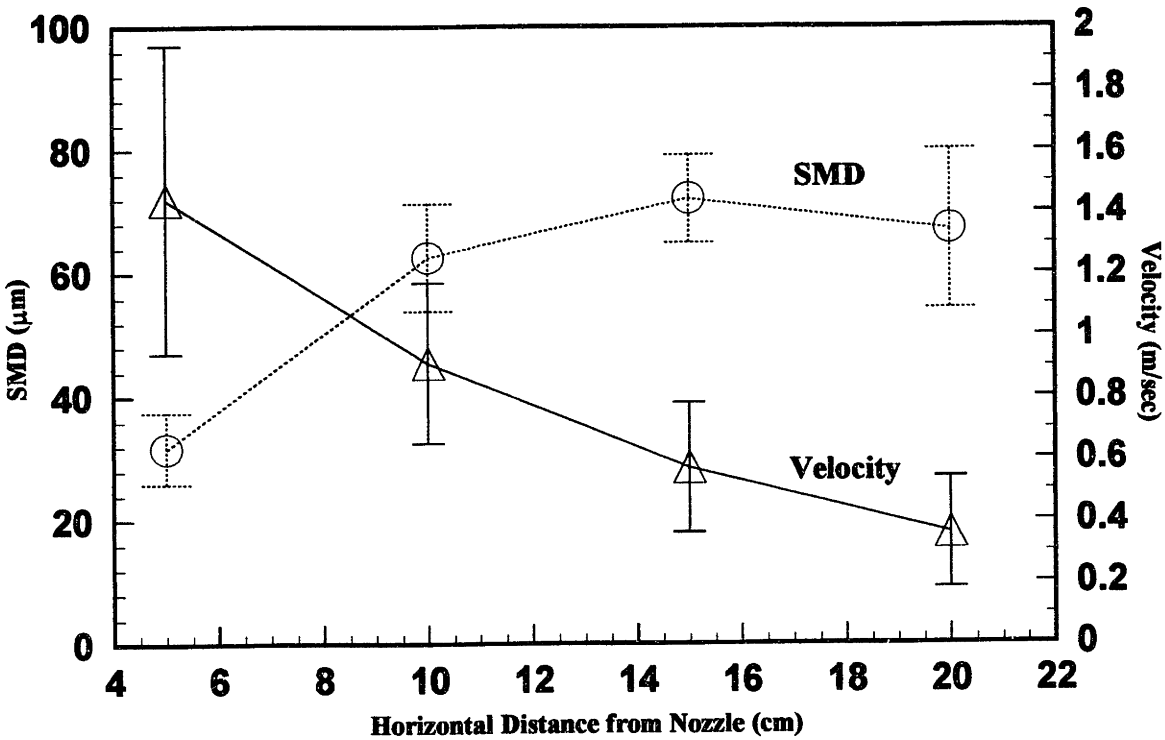

Figure 3.8: Velocity and SMD values with standard deviations for the Hago B-50 nozzle at 345 *kPa*(50 *psi*). Data position is on the nozzle centerline, 5 *cm* from the nozzle. The error bars represent one standard deviation above and below mean values.

Axial Position (cm)	Horizontal and Vertical Position (cm)	SMD (μm)	SMD Std. Dev.	Velocity (m/sec)	Velocity Std. Dev.
5	(0,0)	31.7	5.8	1.44	.50
5	(0,5)	97.1	3.3	1.61	.26
5	(0,-6)	88.8	4.9	.93	.15
5	(5,0)	85.0	2.4	.98	.17
10	(0,0)	62.6	8.7	.91	.26
10	(0,5)	101	5.6	.37	.17
10	(0,-5)	66.0	8.8	.52	.10
15	(0,0)	72.1	7.1	.57	.21
15	(0,2)	101	13.1	.29	.21
15	(0,-8)	70.6	9.5	.23	.08
20	(0,0)	67.2	12.9	.36	.18
20	(0,-8)	71.1	10.3	.24	.09
20	(4,0)	114	24.8	.04	.19

Table 3.1: Hago B-50 average values and standard deviations of diameter and velocity measurements for nozzles 7 through 16 at 345 kPa(50 psi).

3.2 Hago B-37, B-75 and B-50

3.2.1 Droplet Diameter

Figure 3.9 shows the variation in droplet SMD for the Hago B-37 nozzle on the nozzle centerline, 5 cm from the nozzle exit. Figure 3.10 presents the same information for the Hago B-75 nozzle, and Figure 3.11 for the Hago B-50 nozzle. Figure 3.12 shows the data from the Hago B-37, Hago B-50, and Hago B-75 plotted on the same graph.

The droplet SMD on the nozzle centerline, 5 cm from the nozzle can be calculated for each nozzle from

$$SMD_{B-37} = 1.1398 * 10^{-6}\Delta P^4 - 5.0965 * 10^{-4}\Delta P^3 + 8.5815 * 10^{-2}\Delta P^2 - 6.6091\Delta P + 223.22 \quad (3.1)$$

$$SMD_{B-75} = 9.0473 * 10^{-7}\Delta P^4 - 4.2146 * 10^{-4}\Delta P^3 + 7.4631 * 10^{-2}\Delta P^2 - 6.0595\Delta P + 207.21 \quad (3.2)$$

$$SMD_{B-50} = -1.1101 * 10^{-5}\Delta P^3 + 4.7045 * 10^{-3}\Delta P^2 - .69017\Delta P + 49.787 \quad (3.3)$$

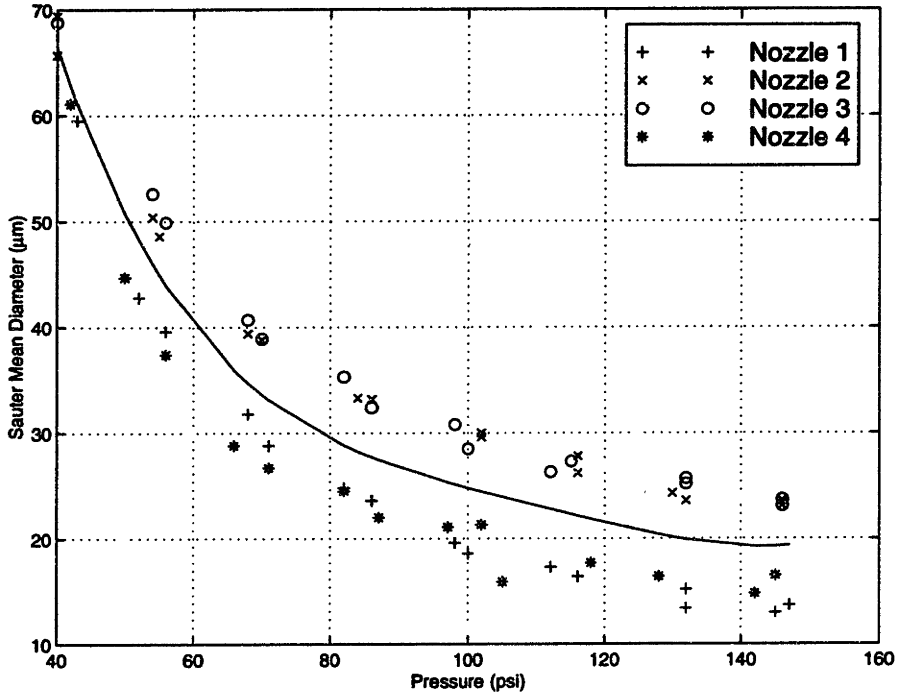

Figure 3.9: Hago B-37. Pressure vs. SMD on nozzle centerline, 5 cm from nozzle.

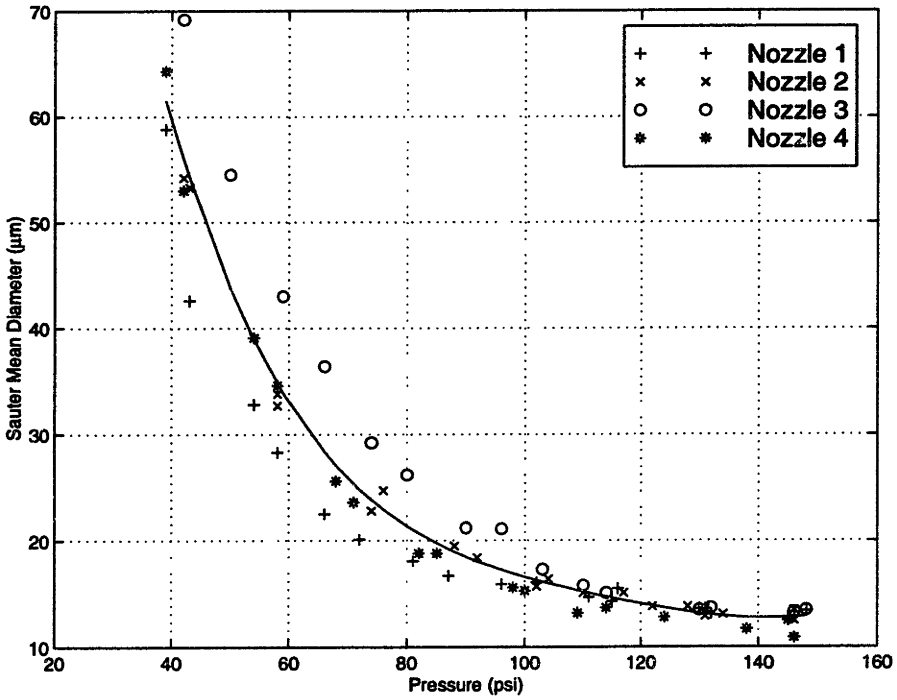

Figure 3.10: Hago B-75. Pressure vs. SMD on nozzle centerline, 5 cm from nozzle.

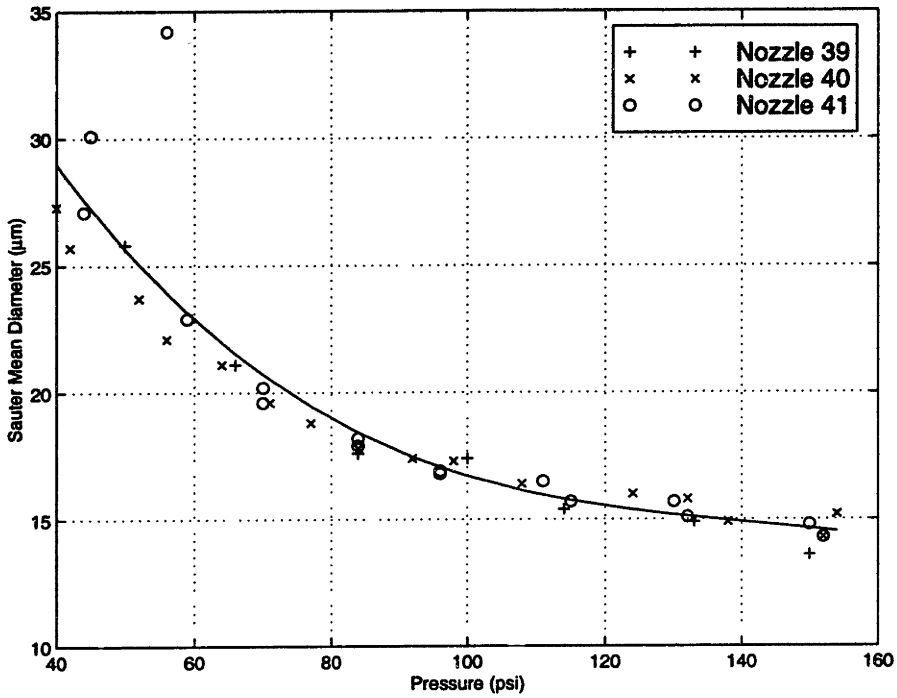

Figure 3.11: Hago B-50. Pressure vs. SMD on nozzle centerline, 5 cm from nozzle.

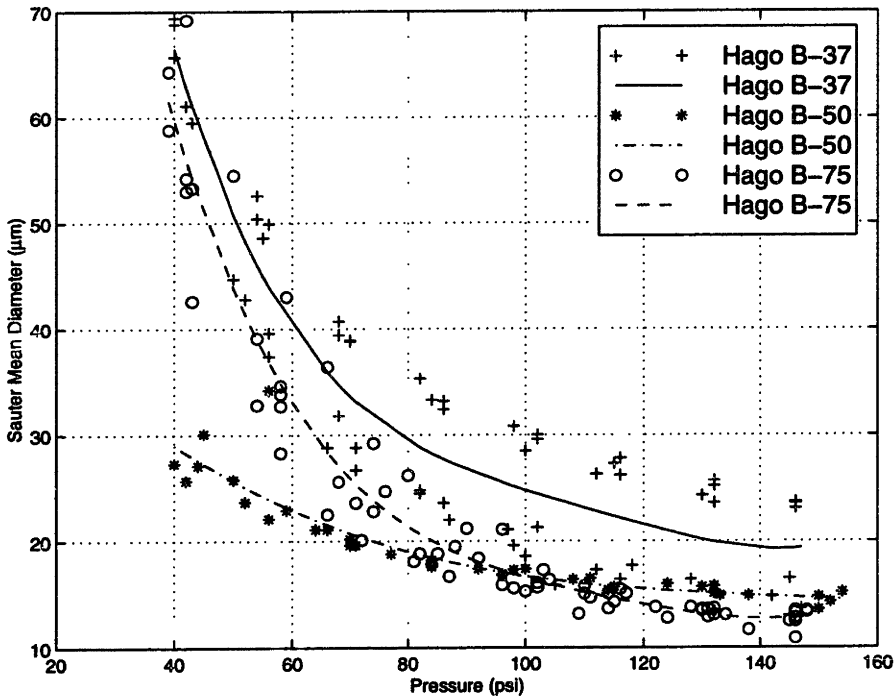

Figure 3.12: Hago B-37, B-50, and B-75. Pressure vs. SMD on nozzle centerline, 5 cm from nozzle. Plot represents data from 4 Hago B-37 nozzles, 3 Hago B-50 nozzles, and 4 Hago B-75 nozzles.

where ΔP is in *psi* and *SMD* is in μm. Using these correlations as mean values, 97% of the data is within 20% of the mean value for the Hago B-50. The B-75 has 91% of the data within 20% of the mean, and the B-37 has only 68% of the data within 20% of the mean.

Nonn and Haugen [7] estimate the maximum error in measurement of the diameter distribution to be 3% for a PDPA set up for 30° forward scatter data collection. At higher pressures, with $SMD \sim 15\ \mu m$, the error introduced by the PDPA is $\sim .15\ \mu m$. The variations observed on the B-50 and B-75 nozzle centerline, 5 *cm* from the nozzle, are fairly small ($\sim 1-2\ \mu m$), so variations in the nozzles have a fairly small effect on the diameter distributions at high pressures. At lower pressures ($\sim 413\ kPa/60\ psi$), the B-50 nozzles still remain fairly uniform, but the B-75 starts to show larger variations between nozzles ($\sim 15\ \mu m$). This is probably due to the B-75 not being in the fully developed spray region until a higher pressure compared to the B-50. The B-37 nozzles show large variations in SMD across the entire pressure range. Even at high pressures, the variation between the four tested nozzles is around 10 μm, but if the nozzles are separated into two groups, then the variation within each group is small. The upper grouping varies by $\sim 1\ \mu m$, while the lower grouping varies by $\sim 4\ \mu m$. The B-37 is more senstive to variations between nozzles than the B-50 or B-75.

In all three nozzles, the SMD decreases from initially large values and approaches a constant value as the pressure increases. For all three nozzles, the largest change in the SMD is between 276 *kPa* (40 *psi*) and 690 *kPa* (100 *psi*). Above 690 *kPa* (100 *psi*), only a small decrease in SMD is obtained with increasing pressure. There is a fairly large difference between the nozzles at low pressures. Both the B-37 and B-75 nozzles produce a spray SMD in the $60-70\ \mu m$ range at 40 *psi*, but the B-50 nozzle produces a SMD around 30 μm at this pressure. At higher pressures ($> 590\ kPa/80\ psi$), the B-50 and B-75 nozzles produce almost identical SMD distributions, while the B-37 nozzle produces a spray cloud with a SMD around 10 μm greater than the B-50/B-75 nozzles. The standard deviation of the SMD on the nozzle centerline, 5 cm from the nozzle, is plotted in Figures 3.13, 3.14, and 3.15 for the B-37, B-50, and B-75 respectively. As the standard deviation of the SMD decreases, the spray diameter distribution becomes more uniform. For all three nozzle types, the SMD standard deviation decreases with increasing injection pressure. Again at high pressures, the SMD standard deviations are all very similar with values around 5 μm, but at low pressures the B-37 and

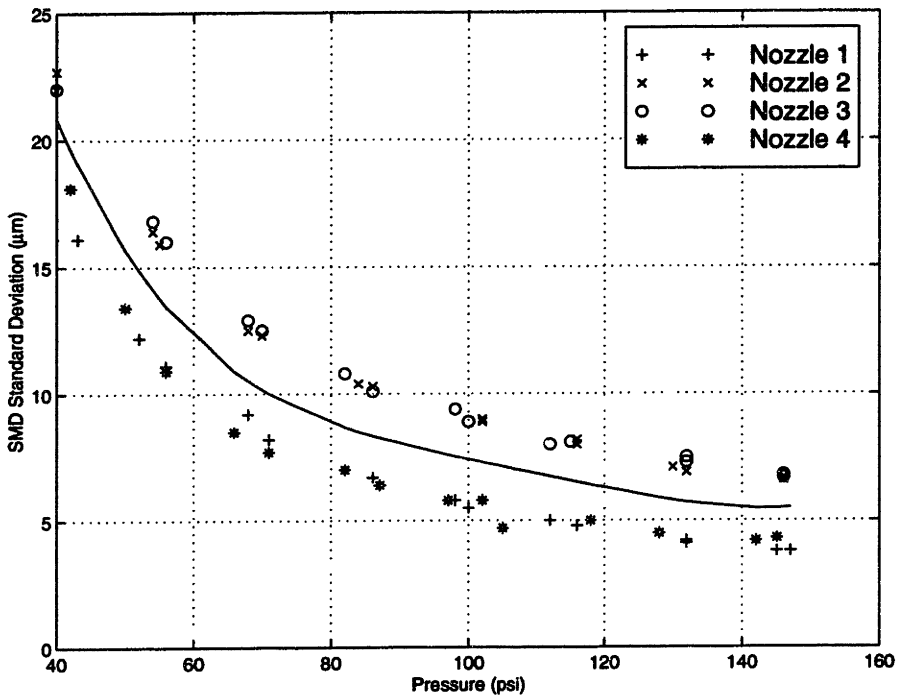

Figure 3.13: Hago B-37. Pressure vs. SMD standard deviation on nozzle centerline, 5 cm from nozzle.

B-75 nozzles have standard deviations in the range of 20 μm while the B-50 standard deviation is around $6-7$ μm at these pressures.

Figures 3.16, 3.17, and 3.18 show the SMD variation with pressure on the nozzle centerline, 20 cm from the nozzle, for the Hago B-37, B-75, and B-50 respectively. For all three nozzles, the SMD decreases with increasing pressure, but the scatter of data points is much greater for the B-37 nozzle than for either the B-50 or B-75. The B-75 has very uniform and repeatable data points, indicating that the central spray cone is still coherent and has not started to break up. The correlation proposed by Lefebvre[1] can be fit to the Hago nozzles at this position for higher pressures ($\Delta P > 694\ kPa/100\ psi$) with only small changes. After converting units and modifying the constant at the beginning of equation(2.8), the correlations for the Hago nozzles become

$$SMD_{B-37} = 7.63 * 10^{-3} \sigma^{.6} \nu_L^{.2} Q^{.25} \Delta P^{-.4} \tag{3.4}$$

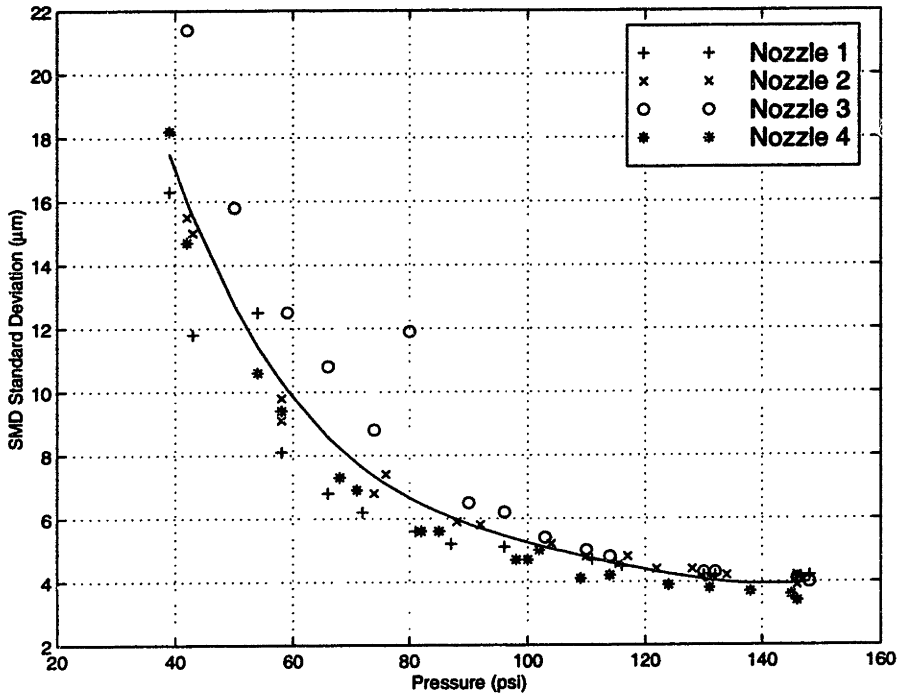

Figure 3.14: Hago B-75. Pressure vs. SMD standard deviation on nozzle centerline, 5 cm from nozzle.

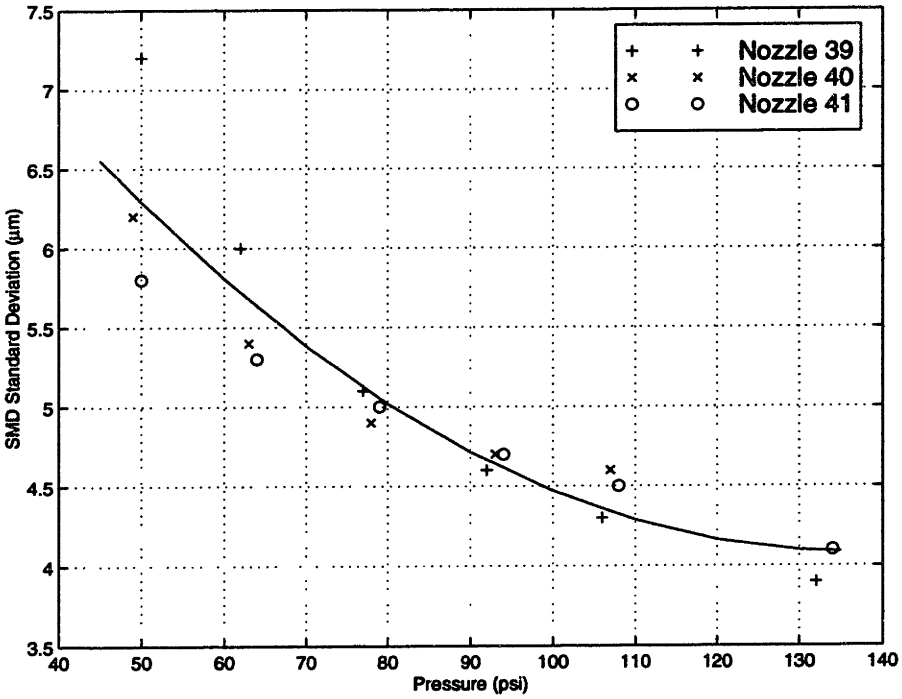

Figure 3.15: Hago B-50. Pressure vs. SMD standard deviation on nozzle centerline, 5 cm from nozzle.

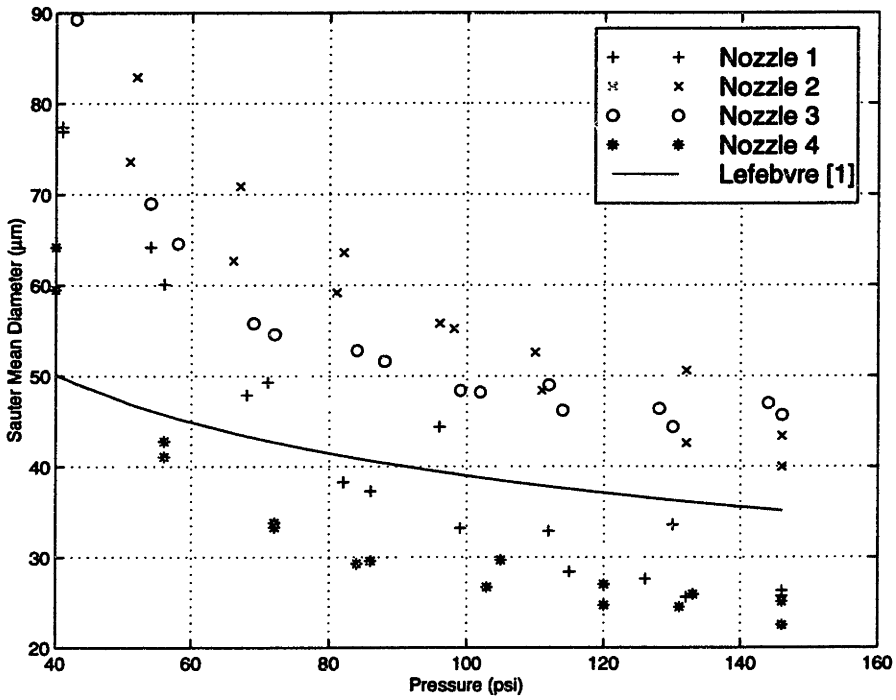

Figure 3.16: Hago B-37. Pressure vs. SMD on nozzle centerline, 20 cm from nozzle.

$$SMD_{B-75} = 4.65 * 10^{-3} \sigma^{.6} \nu_L^2 Q^{.25} \Delta P^{-.4} \tag{3.5}$$

$$SMD_{B-50} = 6.03 * 10^{-3} \sigma^{.6} \nu_L^2 Q^{.25} \Delta P^{-.4} \tag{3.6}$$

where Q is the nozzle volume flow rate in ml/min, ΔP is the injection pressure in psi, σ is the liquid surface tension in N/m, and ν_L is the liquid kinematic viscosity in m^2/sec. These equations are all plotted on Figures 3.16-3.18. These correlations can be modified by changing the exponent on the ΔP term to $-.7$ for the B-50 and -1.2 for the B-75 to obtain a better fit of the data, but this is really only repeating the polynomial curve fits already performed in equations (3.1) to (3.3).

Figures 3.19, 3.20, and 3.21 show the variation of the SMD with pressure in the rain-out region of the nozzles for the B-37, B-75, and B-50 respectively. There is a clear correlation between pressure and the SMD in the rain-out region of the B-37 nozzle, but no noticeable correlation in the B-50 and B-75 nozzles. The B-50 SMD in this region has a small range of values ($60 - 70\ \mu m$), while the B-75 varies over $80 - 100\ \mu m$

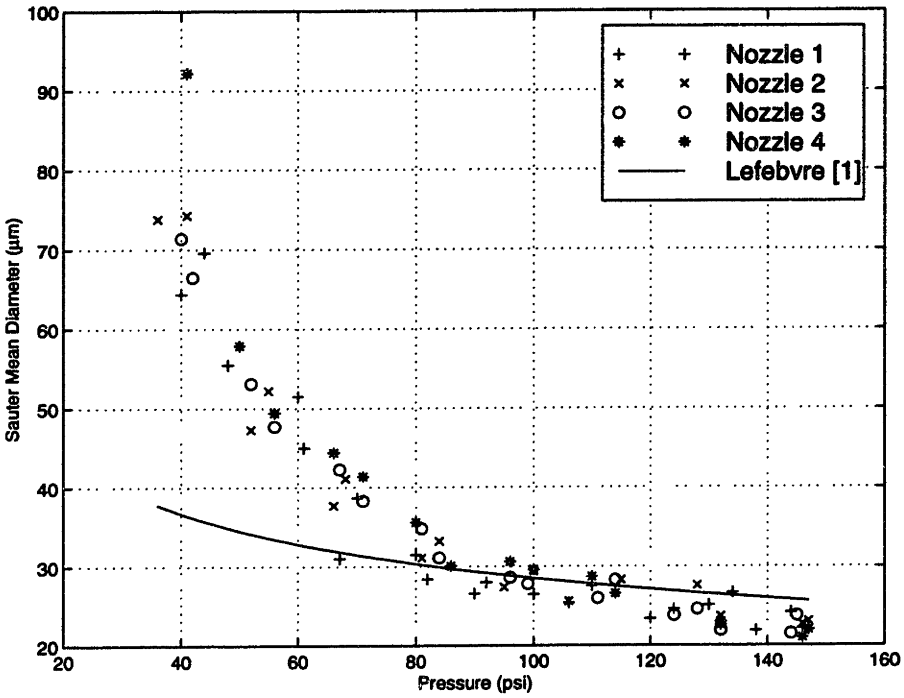

Figure 3.17: Hago B-75. Pressure vs. SMD on nozzle centerline, 20 cm from nozzle.

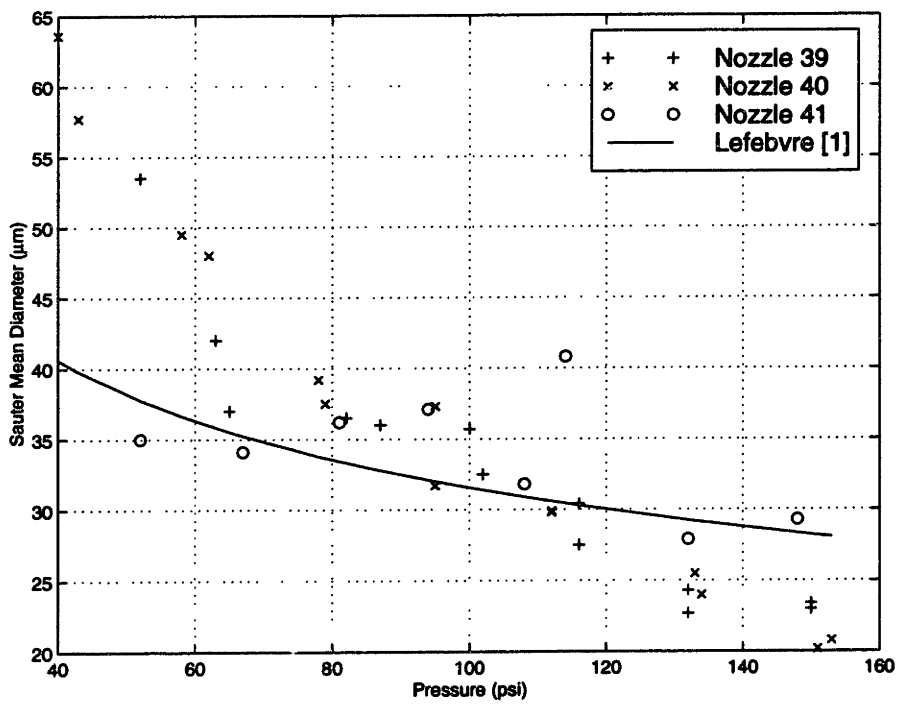

Figure 3.18: Hago B-50. Pressure vs. SMD on nozzle centerline, 20 cm from nozzle.

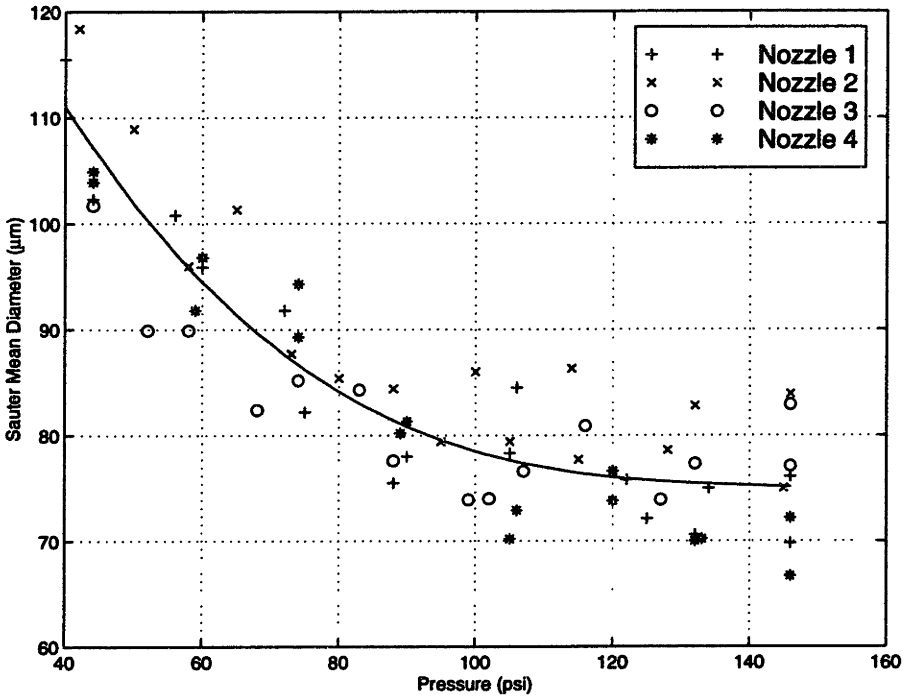

Figure 3.19: Hago B-37. Pressure vs. SMD in nozzle rain-out region.

and the B-37 varies over $60 - 120\ \mu m$.

3.2.2 Droplet Velocity

Figure 3.22 shows the variation of droplet velocity with pressure for the Hago B-37 on the nozzle centerline, 5 cm from the nozzle. Figure 3.23 shows the same information for the Hago B-75 nozzle, and Figure 3.24 for the Hago B-50 nozzle. Figure 3.25 is an overlay of the velocity data. Droplet velocity on the nozzle centerline, 5 cm from the nozzle, can be calculated from

$$V_{B-37} = -3.3938 * 10^{-5}\Delta P^2 + 1.9050 * 10^{-2}\Delta P + 2.3418 \tag{3.7}$$

$$V_{B-75} = -9.9027 * 10^{-5}\Delta P^2 + 4.2390 * 10^{-2}\Delta P + 3.0315 \tag{3.8}$$

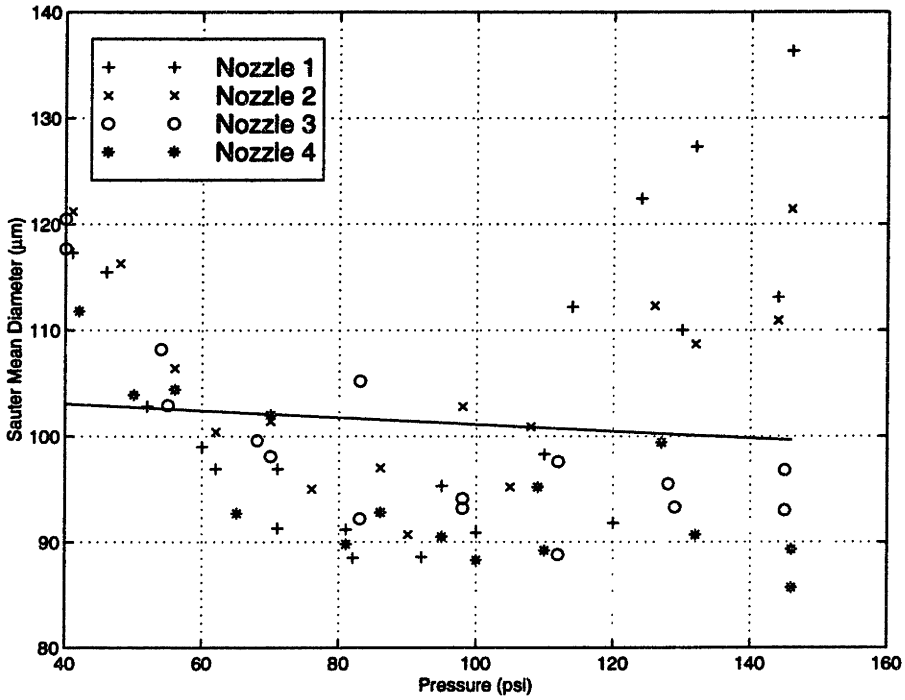

Figure 3.20: Hago B-75. Pressure vs. SMD in nozzle rain-out region.

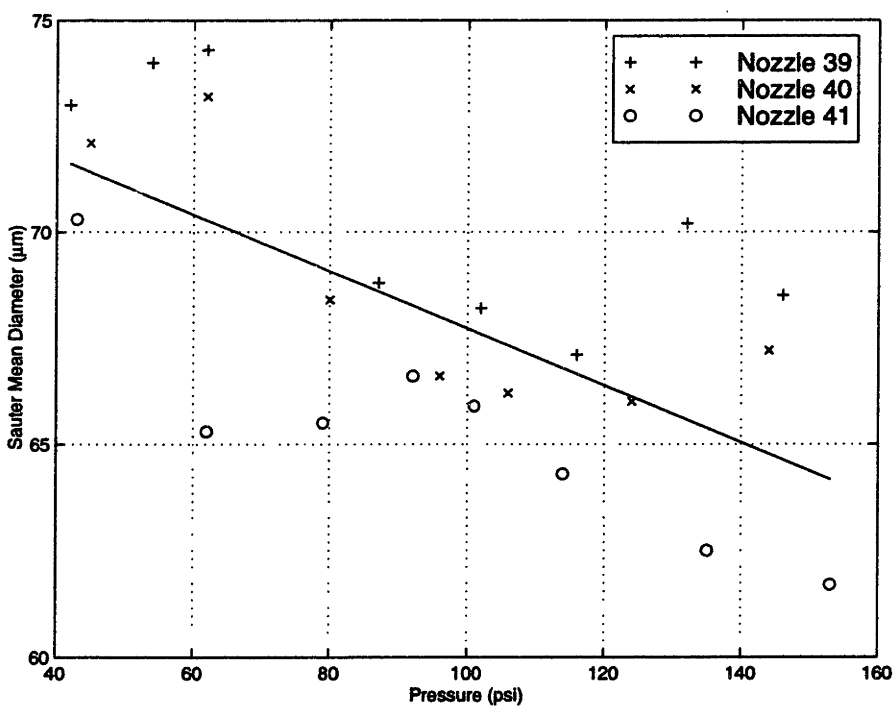

Figure 3.21: Hago B-50. Pressure vs. SMD in nozzle rain-out region.

$$V_{B-50} = -1.3346 * 10^{-4}\Delta P^2 + 5.3070 * 10^{-2}\Delta P - .50047 \tag{3.9}$$

where ΔP is in *psi* and V is in m/sec. For the B-50 and B-75 nozzles, 82% of the data is within 20% of correlation values, while only 22% of the data is within 20% of the B-37 correlation. The droplet velocity for the B-75 is always greater than the B-50 and B-37 values. At higher pressures, the droplet velocities of the B-50 and B-37 start to converge.

Drain [8] has stated that the fractional error in frequency measurement for determining droplet velocity is $\Delta\nu_D/\nu_D = \pm 1/n_f$, where n_f is the number of fringes a particles passes through in the measurement volume. The particle velocity can be calculated from

$$\nu_D = \frac{2v}{\lambda} sin\frac{\alpha}{2} \tag{3.10}$$

where v is the particle velocity, ν_D is the measured signal frequency, λ is the laser beam wavelength, and α is the beam intersection angle. The error in the velocity measurement can then be calculated as

$$\frac{\Delta v}{v} = \frac{1}{n_f}. \tag{3.11}$$

For the PDPA configuration used in the evaluation of the Hago nozzles, $n_f = 26$ and and $\Delta v/v = 4\%$. This error can be reduced using appropriate signal processing and there are other sources of error such as changes in beam intersection angle, errors in velocity offsets, etc., but for a properly set up system, this is the largest source of error and a good estimate of the total error introduced. For a velocity of 5 m/sec, this leads to an error of .2 m/sec.

As can be seen in Fig. 3.25, the spread of data around the 5 m/sec point is much larger than .2 m/sec for all three nozzle types. It can be clearly seen in Figures 3.22, 3.23, and 3.24 that the variations in velocity measurement for any single nozzle can be accounted for from the measurement error, but the variation

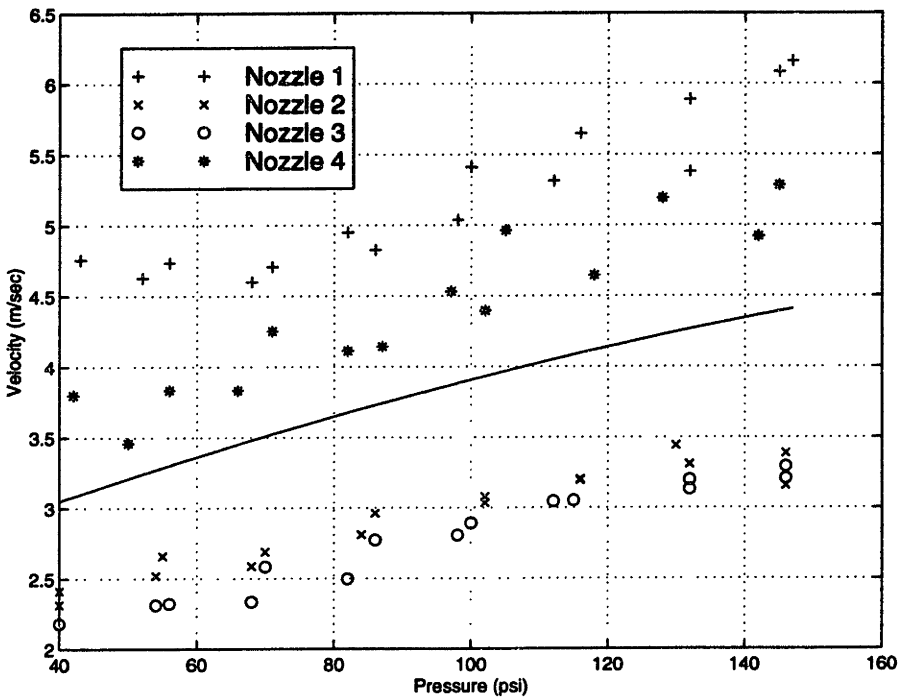

Figure 3.22: Hago B-37. Pressure vs. velocity on nozzle centerline, 5 cm from nozzle.

between nozzles of the same type are too large for just measurement error. Variations from manufacturing between nozzles affect the velocity distributions to a much greater extent than the diameter distributions.

3.2.3 Flow Rate

Figure 3.26 shows the variation of nozzle flow rate with pressure for the Hago B-37 nozzle. Figure 3.27 and Figure 3.28 present the same data for the B-75 and B-50 nozzles. Figure 3.29 is an overlay of the flow data for all three nozzles. A basic inviscid analysis was developed in Section 2.2 to show that the flow rate through a pressure-swirl atomizer is only a function of pressure for incompressible flow [4] and the flow through the nozzle can be expressed as

$$Q = A_c\sqrt{\Delta P} \tag{3.12}$$

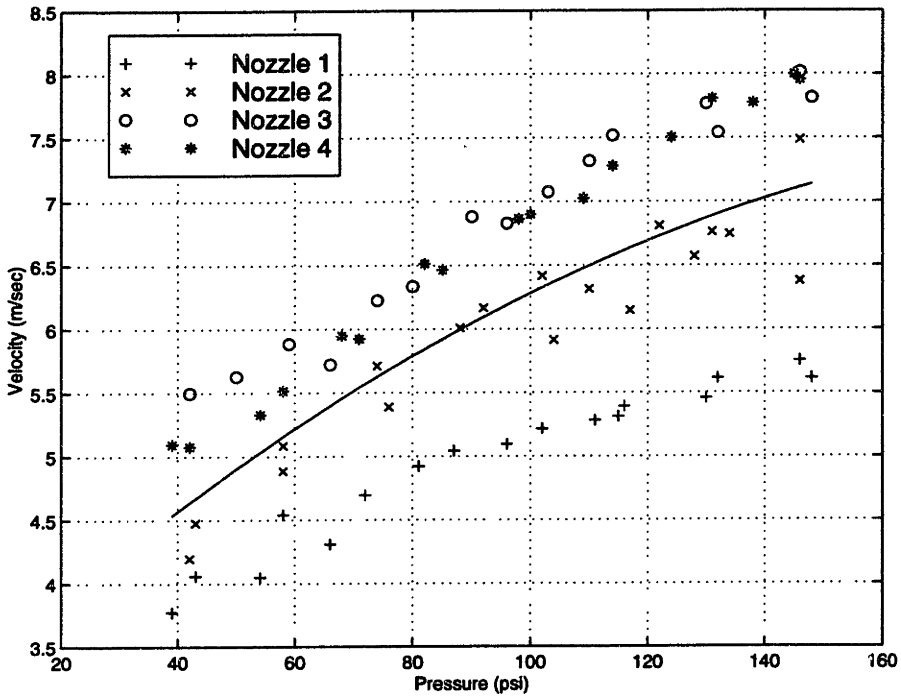

Figure 3.23: Hago B-75. Pressure vs. velocity on nozzle centerline, 5 cm from nozzle.

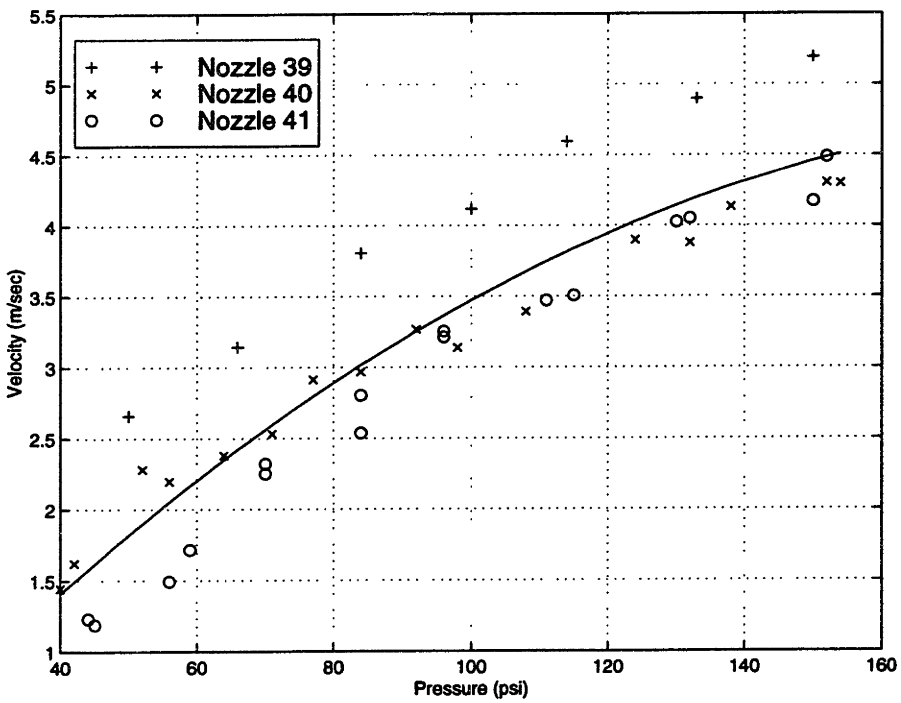

Figure 3.24: Hago B-50. Pressure vs. velocity on nozzle centerline, 5 cm from nozzle.

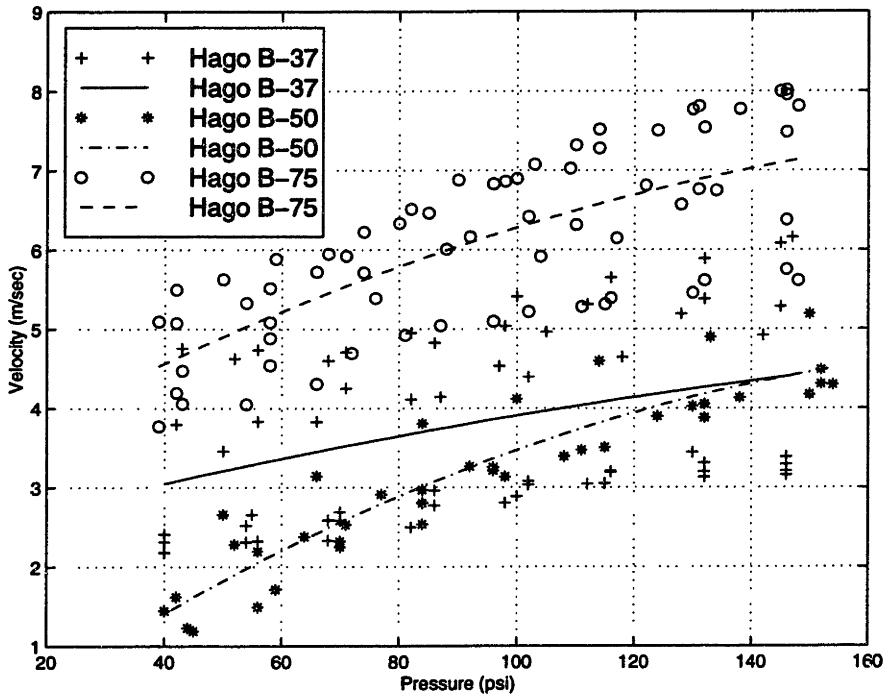

Figure 3.25: Hago B-37, B-50 and B-75. Pressure vs. velocity on nozzle centerline, 5 cm from nozzle. Plot represents data from 4 Hago B-37 nozzles, 3 Hago B-50 nozzles, and 4 Hago B-75 nozzles.

Nozzle Type	A_c for ΔP in kPa	A_c for ΔP in psi
B-37	1.26 $ml/min\sqrt{kPa}$	3.30 $ml/min\sqrt{psi}$
B-50	1.45 $ml/min\sqrt{kPa}$	3.81 $ml/min\sqrt{psi}$
B-75	2.60 $ml/min\sqrt{kPa}$	6.83 $ml/min\sqrt{psi}$

Table 3.2: Nozzle flow rate for Hago nozzles. Gage pressure in kPa or psi.

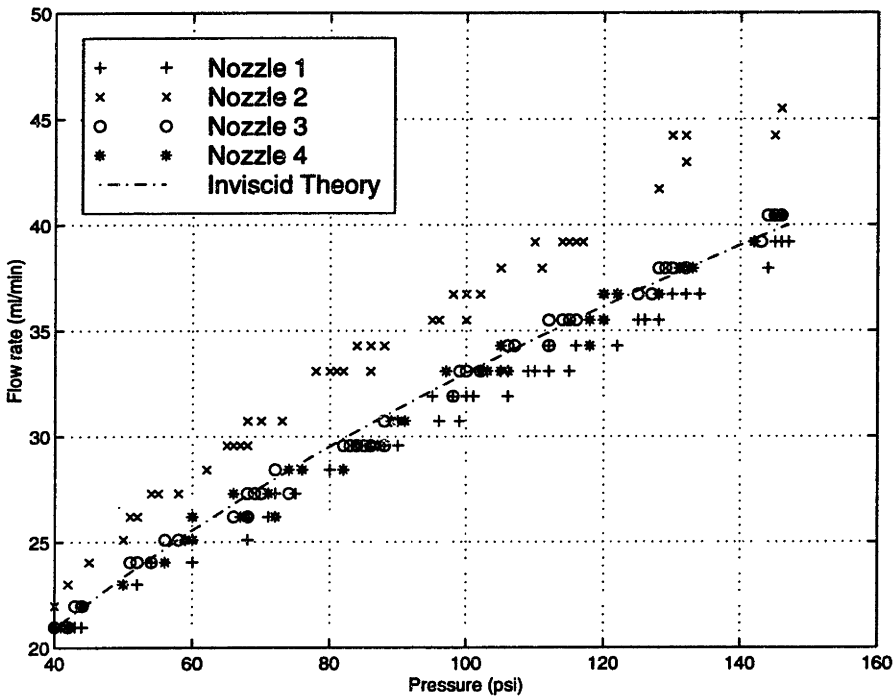

Figure 3.26: Hago B-37. Pressure vs. flow rate.

where A_c is constant for a particular nozzle design and fluid, ΔP is the gage pressure, and Q is the nozzle flow rate in ml/min. The values for A_c are listed in Table (3.2) for all three nozzles and for input units of kPa and psi. The flow rate output is always in ml/min. The inviscid theory for each nozzle type is plotted on the flow rate graphs. The rotameter used to measure the flow rate is accurate to ± 2.2 ml/min, but is repeatable to $\pm .3$ ml/min.

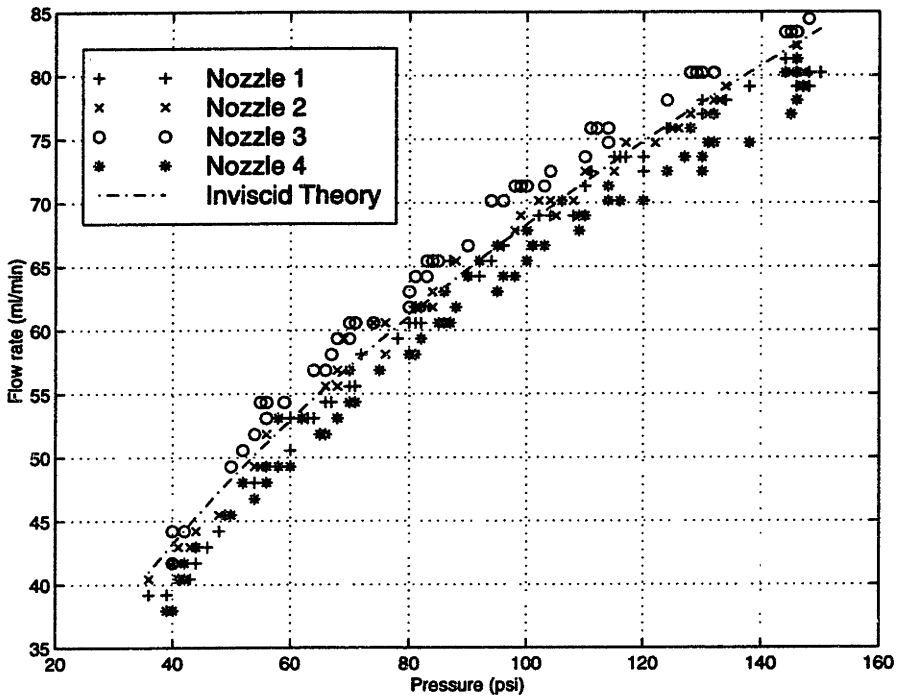

Figure 3.27: Hago B-75. Pressure vs. flow rate.

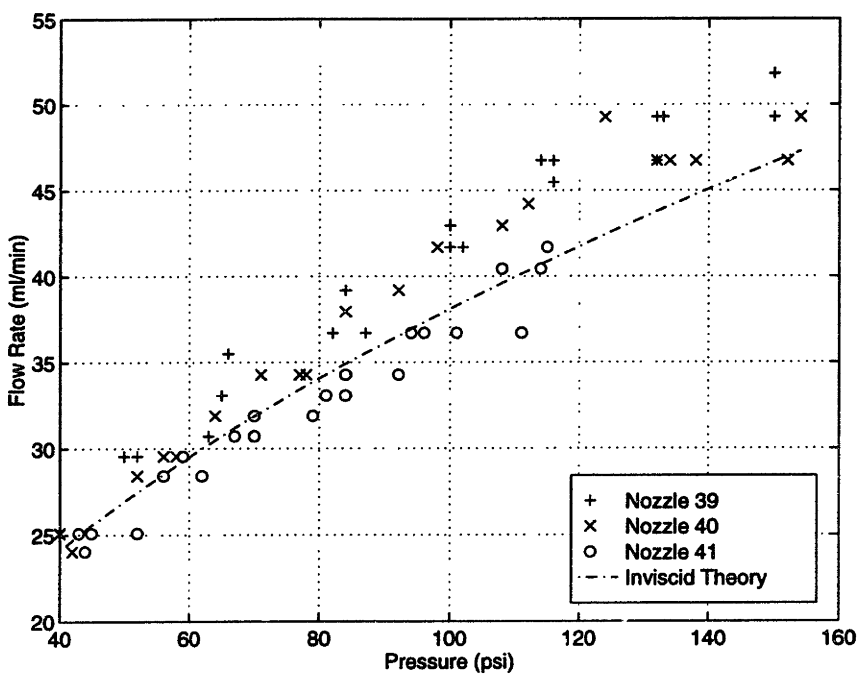

Figure 3.28: Hago B-50. Pressure vs. flow rate.

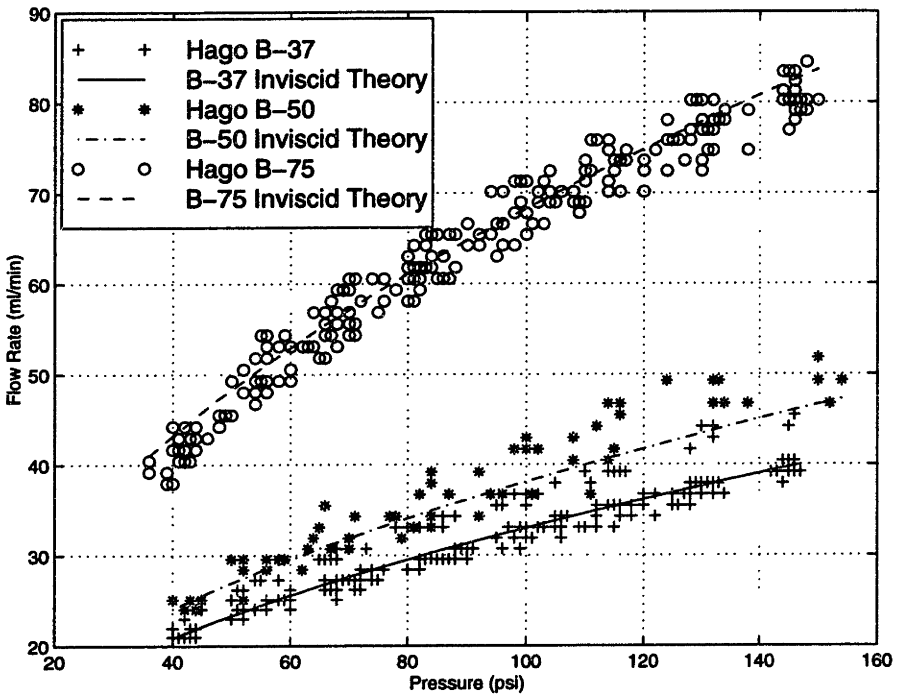

Figure 3.29: Hago B-37, B-50 and B-75. Pressure vs. flow rate. Plot represents data from 4 Hago B-37 nozzles, 3 Hago B-50 nozzles, and 4 Hago B-75 nozzles.

Position	Data Type	Nozzle Type	Within 20%	Within 10%
Nozzle centerline, 5 *cm* from nozzle.	Diameter	B-37	68%	13%
		B-75	91%	75%
		B-50	97%	95%
	Velocity	B-37	22%	5%
		B-75	82%	49%
		B-50	82%	62%
Nozzle centerline, 20 *cm* from nozzle.	Diameter	B-37	42%	18%
		B-75	97%	87%
		B-50	91%	74%
	Velocity	B-37	45%	21%
		B-75	91%	58%
		B-50	80%	46%
Rainout region.	Diameter	B-37	100%	92%
		B-75	97%	54%
		B-50	100%	100%

Table 3.3: Percent of nozzle data within 10% and 20% of mean values.

3.3 Nozzle Comparison

The three different nozzles that have been tested all have similar spray patterns. All of the nozzles produce a sheath of large slower droplets surrounding a core of higher velocity small droplets. The flow splits into a region of central core flow and a rain-out region within $15 - 20$ *cm* of the nozzle.

At high pressures ($> 690\ kPa/100\ psi$), the three nozzles produce droplets with similar SMD distributions on the nozzle centerline close to the nozzle, with SMD values in the range of $15 - 25\ \mu m$. As distance from the nozzle increases, the B-37 diverges with a SMD range of $25 - 50\ \mu m$, while the B-50 and B-75 nozzles remain similar with SMD values in the range of $20 - 30\ \mu m$. At low pressures, the B-50 nozzle produces a smaller SMD than either the B-37 or B-75. This indicates that for low water supply pressures the B-50 will produce better evaporative cooling[1]. Table 3.3 presents the percent of data points for each type of nozzle that are within 20% and 10% of mean values calculated using polynomial curve fits (i.e. equations (3.1) to (3.3) and equations (3.7) to (3.9)). The largest difference between the nozzles is the flow rate. The ratio of flow between any two types of nozzles at any pressure is approximately constant and can be evaluated by taking the ratio of the A_c constants from the inviscid nozzle analysis.

[1] A smaller SMD will increase evaporation rate.

A couple of points need to be made on individual nozzle performance. The B-37 nozzles have the largest variations in SMD from nozzle to nozzle. This can easily be seen in Figures 3.9 and 3.16 where the nozzles seem to fit into two groupings. This is probably due to variations between nozzles introduced in the manufacturing process. The B-37 has the smallest exit orifice of the three nozzles tested, so similar tolerances between nozzles types during manufacturing will produce larger variations as a percent of total orifice size in the B-37 than for the B-50 or B-75[2]. Also, as the nozzles become smaller, viscous effects will play a larger role in the flow patterns and nozzle variations will have a larger effect on spray characteristics.

The SMD distribution on the centerline of the B-75 nozzle, at 20 *cm* from the nozzle, is more uniform and repeatable than that of the B-50 and, especially, that of the B-37. This is because the central core flow of small high velocity drops does not disintegrate as quickly as for the B-50 and B-37. The central core of the B-75 has higher velocities and will have longer penetration depths[3]. This also indicates that the B-75 will be less affected by external air currents than the B-50 or B-37.

3.4 Summary of Nozzle Performance

The Hago B-50 nozzle spray structure was examined using a flow visualization technique, and then the spray was fully characterized using the Phase Doppler Particle Analyzer. The Hago B-37 and B-75 spray clouds were examined at a few key points using the PDPA, so comparisons to the B-50 could be made. The following conclusions can be made about the Hago spray nozzles:

- At all pressures, the nozzles produce a sheath of large particles surrounding a core of small, high velocity particles.
- Within the high velocity central core, increasing pressure produces better quality atomization. Smaller droplets are obtained with a more uniform size distribution. The largest improvement in atomization is obtained between 345 kPa(50 psi) and 690 kPa(100 psi), with only a small additional reduction in droplet SMD from 690 kPa(100 psi) to 1034 kPa(150 psi).

[2]A 5 μm variation in orifice diameter will produce a larger error in orifice area for a small orifice than for a large orifice.
[3]Horizontal distance spray travels in still air.

- Increasing pressure increases the spray cloud invasion length in still air.
- Nozzles are less sensitive to rust and mineral deposits when operated at higher pressures ($\Delta P > 690\ kPa/100\ psi$).
- Pressure variations have little effect on the rain out droplet size.
- The spray distribution beyond 5 to 10 cm from the nozzle is dominated by external air currents, regardless of injection pressure or nozzle type.
- The flow rate for each type of nozzle is given by $Q = A_c\sqrt{\Delta P}$, where ΔP is the gage pressure, Q is the flow rate in ml/min, and A_c is a constant. The values of A_c for the Hago nozzles are

$$B-37 \qquad A_c = 1.26\ (ml/min\sqrt{kPa}) = 3.30\ (ml/min\sqrt{psi})$$

$$B-50 \qquad A_c = 1.45\ (ml/min\sqrt{kPa}) = 3.81\ (ml/min\sqrt{psi})$$

$$B-75 \qquad A_c = 2.60\ (ml/min\sqrt{kPa}) = 6.83\ (ml/min\sqrt{psi})$$

- At low pressures ($\Delta P < 690\ kPa/100\ psi$), the B-50 nozzle produces better atomization with a smaller SMD than the B-37 or B-75.
- At high pressures ($\Delta P \geq 690\ kPa/100\ psi$), the SMD is very similar between all the nozzles.
- The B-75 has higher droplet velocities and longer invasion lengths than the other nozzles.
- The B-37 is more sensitive to variations from manufacturing than the B-50 and B-75.
- The B-37 is more sensitive to scaling and rust deposits due to its very small orifice size.

Chapter 4

Governing Equations

This chapter covers the development of a heat transfer model for a single fiber moving through still air with no spray present. The basic governing equations are discussed and the assumptions made in the model are explained. The first section covers the analysis of the velocity boundary layer. The second section develops an expression for the shape of the thermal boundary layer and solves for the heat transfer from the fiber.

4.1 Velocity Profile and Boundary Layer

The boundary layer equations for laminar, steady state, incompressible flow on a continuous moving fiber in still air are

$$\frac{\partial u}{\partial x} + \frac{\partial v}{\partial y} + \frac{v}{a+y} = 0 \tag{4.1}$$

$$\rho u \frac{\partial u}{\partial x} + \rho v \frac{\partial u}{\partial y} = \mu \left(\frac{\partial^2 u}{\partial y^2} + \frac{1}{a+y} \frac{\partial u}{\partial y} \right) \tag{4.2}$$

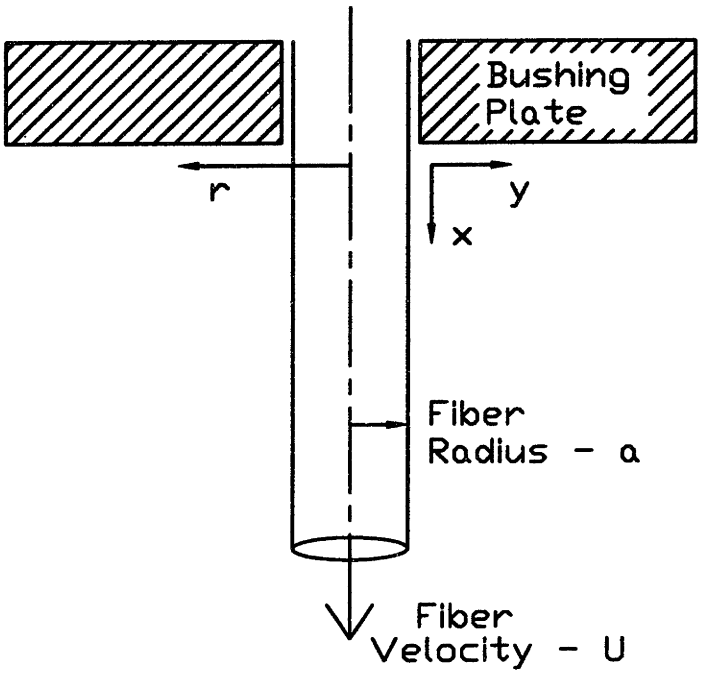

Figure 4.1: Coordinate system

$$u\frac{\partial T}{\partial x} + v\frac{\partial T}{\partial y} = \frac{k}{\rho C_p(a+y)}\frac{\partial}{\partial y}\left((a+y)\frac{\partial T}{\partial y}\right) \tag{4.3}$$

where u is the axial velocity, v is the radial velocity, and the coordinate system is described in Fig. 4.1. The position $y = 0$ corresponds to the fiber surface and $x = 0$ to the fiber bushing plate. The fiber radius and fiber velocity are assumed constant over the length of the fiber[1]. All equations are written in terms of y rather than r to simplify the boundary conditions. Equations (4.1) and (4.2) are subject to the boundary conditions

$$u = U, v = 0 \text{ at } y = 0 \tag{4.4}$$

$$u \to 0, v \to 0 \text{ as } y \to \infty \tag{4.5}$$

[1]Necking region is neglected.

and equation (4.3) is subject to the boundary conditions

$$T(x,y) = T_f(x) \quad \text{at} \quad y = 0 \tag{4.6}$$

$$T(x,y) \to T_\infty \ , \frac{\partial T}{\partial y} \to 0 \quad \text{as} \quad y \to \infty \tag{4.7}$$

The objective of the analysis is to determine the fiber temperature profile $T_f(x)$. Based on the work of Glauert and Lighthill[9] for axial flow over a long cylinder, and the analysis of an infinite cylinder issuing from a slot by Sakiadis[10], a velocity profile of the form

$$\frac{u}{U} = 1 - \frac{1}{\alpha} ln(1 + \frac{y}{a}) \quad \text{for} \quad y \leq \delta(x) \tag{4.8}$$

$$\frac{u}{U} = 0 \quad \text{for} \quad y \geq \delta(x) \tag{4.9}$$

is assumed, where α is a function of x only. By setting $u/U = 0$, the boundary layer thickness δ, can be defined as $\delta = a(e^\alpha - 1)$. Integrating equations (4.1) and (4.2) from the fiber surface to ∞ leads to the momentum integral equation

$$\frac{d}{dx} \int_0^\infty u^2(a+y)dy = -\frac{a\mu}{\rho} \frac{\partial u}{\partial y}|_{y=o} \tag{4.10}$$

The velocity profile (eqn. 4.8) can be substituted into equation (4.10) and the velocity parameter α can be evaluated using the boundary conditions. The resulting relationship between α and x [11] is

$$\frac{2\nu x}{Ua^2} = \frac{e^{2\alpha}-1}{\alpha} + Ei(2\alpha) + ln(2\alpha) + \gamma - 2 \tag{4.11}$$

where $\gamma = .5572..$ is Euler's constant and $Ei(2\alpha)$ is the exponential integral defined by

$$Ei(2\alpha) = \int_{-\infty}^{2\alpha} \frac{e^t}{t} dt. \tag{4.12}$$

Equation (4.11) cannot be explicitly solved for α in terms of x. This requires a different method of solution for all remaining analysis. Rather than attempting to solve for all quantities in terms of x, solutions are obtained in terms of α.

The use of the integral technique to solve for the velocity boundary layer is not exact and the assumption of a logarithmic velocity profile is a source of error in the analysis. The boundary conditions at the fiber surface are satisfied by equation (4.8), but the boundary conditions at $y = \delta$ are not satisfied, i.e.

$$\frac{\partial u}{\partial y}\Big|_{y=\delta} = \frac{-U}{\alpha(x)}\left(\frac{1}{a+\delta}\right) \neq 0. \tag{4.13}$$

The error introduced by this will decrease as distance from the fiber tip increases since as x increases, $\alpha(x)$ and δ increase and the value of equation (4.13) approaches zero. The magnitude of the error at the tip of the fiber can be estimated by finding the local drag coefficient defined as

$$C_D = -2\pi a\mu \frac{\partial u}{\partial y}\Big|_{y=0}/(\mu U) = \frac{2\pi}{\alpha(x)} \tag{4.14}$$

at $x = 0$. Bourne and Elliston [11] have shown that

$$\frac{2\nu x}{Ua^2} \sim \frac{1}{3}\alpha^2 \quad \text{as} \quad \alpha \to 0 \tag{4.15}$$

and the local drag coefficient becomes

$$C_D = .816\pi \left(\frac{Ua^2}{\nu x}\right)^{\frac{1}{2}} \quad \text{as} \quad x \to 0. \tag{4.16}$$

In the limit as $x \to 0$, the local drag coefficient on the fiber should be the same as that on a semi-infinte flat sheet issuing from a slot[2]. Sakiadis [12] developed an exact solution for the case of a semi-infinite sheet:

$$C_D = .8875\pi \left(\frac{Ua^2}{\nu x}\right)^{\frac{1}{2}} \tag{4.17}$$

Comparing equations (4.16) and (4.17) shows that the logarithmic profile causes the local drag coefficient to be underestimated by 8.7% at the leading edge of the fiber. This error will decrease as the distance from the tip of the fiber increases.

Sayles[13] has solved the local drag coefficient for a continous cylinder in axial motion based on dimensionless velocity components and a dimensionless curvature parameter. Sayles presented tabulated data to compare the results from the integral method using a logarithmic profile to his solution calculted using a difference-differential method. The data is presented based on the dimensionless length parameter $s = \nu x/Ua^2$. At $(s = 0)$[3], Salyes' solution matches the results from Sakiadis[12] exact solution for a flat plate and is 8.7% higher than the solution based on a logarthimic velocity profile. For increasing values of s, Sayles' data and the solution start to converge, until the values are within 5.3% for $s = 1000$. This corresponds to a fiber position of 7.3 cm on a 10 μm fiber moving at 60 m/sec. This error will continue to

[2] As $x \to 0$, the radius of curvature becomes very large compared with distance and the cylinder can be modeled as flat plate.
[3] This corresponds to $x = 0$, i.e. the fiber tip.

decrease as the value of x increases.

Beese and Gersten[14] also solved for the skin friction on a circular cylinder moving in a fluid at rest. They solved the Navier-Stokes equations as an asymptotic expansion with respect to the perturbation parameter $\epsilon = 1/\sqrt{Re}$ by using the method of matched asmyptotic expansions, but the tabulated data presented is only valid for very short lengths ($\sim 2.5\ mm$) for the fiber diameters of interest and does not provide practical information for comparison purposes in this case.

A significant amount of work has been performed measuring the drag and heat transfer from long fibers in axial flow [15] [16]. Gould and Smith [17] measured the air drag on syntheic fibers for air speeds up to 100 m/sec. They found that for $Re_a = \rho U a/\mu < 10$, results match those of Glauert and Lighthill [9] developed using the integral method for laminar flow over a long cylinder with an assumed logarithmic profile. For $Re_a > 200$, the experimental data approached theoretical results for fully turbulent boundary layers. The region $10 < Re_a < 200$ was found to be a transitional flow region. The fibers considered in this report fall into the region of $Re_a < 25$ with most fibers satisfying $Re_a < 10$, and laminar flow is assumed for all fibers across the entire boundary layer.

Richelle et al.[18] compared solutions for the viscous boundary layer of a long fiber in axial flow and for an infinite fiber moving through still air. They found a significant theoretical difference between the growth of the boundary layers in the two cases. The data obtained on fibers in wind tunnels[4] is of limited quantitative use for infinite fibers moving through a still medium.

4.2 Heat Transfer and Thermal Boundary Layer

The Karman-Pohlhausen integral technique can also be used to calculate the heat transfer from the fiber. Consider the control volume in Fig. 4.2. Neglecting conduction in the x direction, an energy balance on the boundary layer yields

[4]Fibers in axial flow.

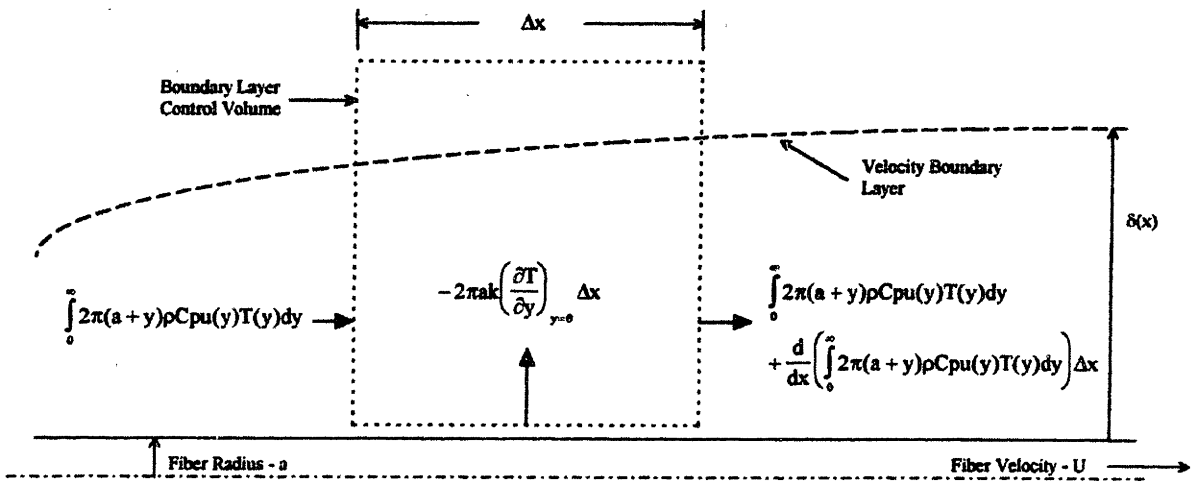

Figure 4.2: Boundary layer control volume.

$$\frac{d}{dx}\int_0^\infty \rho C_p T(y)u(y)2\pi(a+y)dy = -2\pi ak\frac{\partial T}{\partial y}|_{y=0} \tag{4.18}$$

where $u(y)$ is the boundary layer velocity profile, $T(y)$ is the boundary layer temperature profile and k is the thermal conductivity of the air. Another equation is needed to determine the axial variation in fiber temperature. For fibers with diameters less than 200 μm, Papmichael and Miaoulis [19] have shown that the effect of axial conduction can be neglected. By checking the Biot number, it can be shown that radial conduction within the fiber can also be neglected. The Biot number is defined as

$$Bi = \frac{\overline{h_c}r}{k} \tag{4.19}$$

where $\overline{h_c}$ is an average convective heat transfer coefficient, r is a characteristic length (in this case the fiber radius $r = a$), and k is the thermal conductivity of glass. The average convective heat transfer coefficient can be estimated from a bulk energy balance of a drawn fiber under steady state conditions.

$$\overline{h_c} A \overline{\Delta T} = \dot{m}_f \Delta T_f C_{p_f} \tag{4.20}$$

where $A = 2\pi aL$ is the total fiber surface area, $\overline{\Delta T}$ is the average temperature difference between the fiber and the surroundings along the length of the fiber, $\dot{m}_f$ is the mass flow of glass, ΔT_f is the total fiber temperature change, and C_{p_f} is the glass specific heat. The mass flow of glass is given by $\dot{m}_f = \pi a^2 \rho_f U$ where U is the fiber velocity, and the average convective heat transfer coefficient can be calculated from

$$\overline{h_c} = \frac{\rho_f C_{p_f} a U \Delta T_f}{L \overline{\Delta T}}. \tag{4.21}$$

For a 10 μm diameter fiber moving at 60 m/sec, $\overline{h_c} = 2060\ W/m^2K$ for a fiber length of 1 m, a fiber temperature change from 1500 K to 360 K and an environmental temperature of 320 K. The thermal conductivity of glass is 29.4 W/mK, and the Biot number for this case evaluates to $Bi = 3.5 * 10^{-4} << .1$ and radial conduction can be neglected.

For the control volume of the fiber(Fig. 4.3), the energy conservation equation can then be written as

$$\frac{d}{dx}(\pi a^2 \rho_f C_{p_f} T_f U) = 2\pi a k \frac{\partial T}{\partial y}\Big|_{y=0} \tag{4.22}$$

where ρ_f is the fiber density, C_{p_f} is the fiber specific heat, and conduction along and across the fiber is neglected. Defining

$$\Theta(x,y) = T(x,y) - T_\infty \quad \text{and} \quad \Theta_f(x) = T_f(x) - T_\infty \tag{4.23}$$

a temperature profile of the form

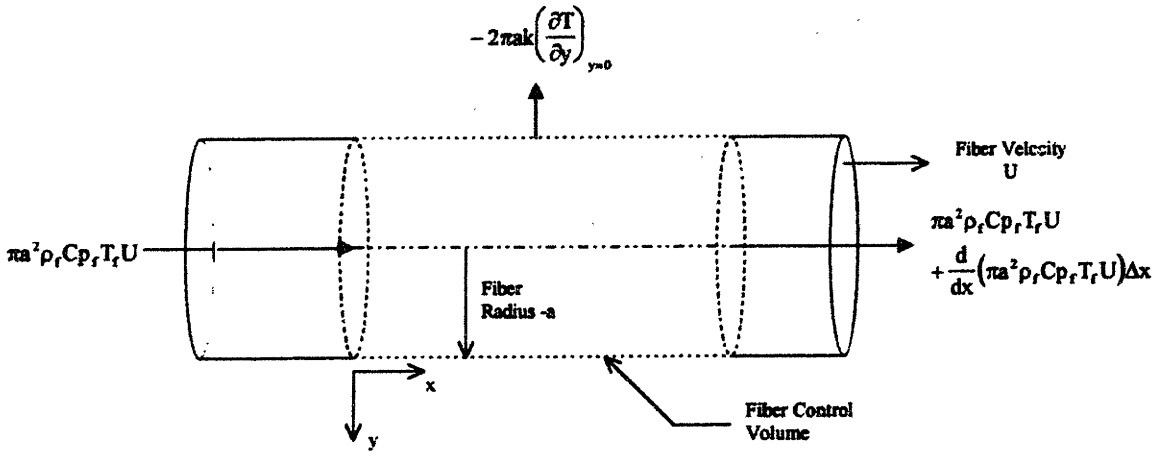

Figure 4.3: Fiber control volume

$$\frac{\Theta}{\Theta_f} = 1 - \frac{1}{\beta}\left(\frac{y}{a} + p\frac{y^2}{a^2} + q\frac{y^3}{a^3}\right) \quad \text{for} \quad y \leq \delta_T \tag{4.24}$$

$$\frac{\Theta}{\Theta_f} = 0 \quad \text{for} \quad y \geq \delta_T \tag{4.25}$$

can be assumed where β is only a function of x, and p and q are constants. The boundary conditions on the temperature profile are

$$\Theta = \Theta_f \quad \text{at} \quad y = 0 \tag{4.26}$$

$$\Theta \to 0, \quad \frac{\partial \Theta}{\partial y} \to 0 \quad \text{as} \quad y \to \infty \tag{4.27}$$

Evaluating the energy equation (eqn. 4.3) at $y = 0$ and substituting Θ for T, it can be shown that

$$U\frac{d\Theta_f}{dx} = \frac{-k\Theta_f}{\rho C_p \beta a^2}(1+2p). \tag{4.28}$$

Evaluating equation (4.22) and substituting for the assumed temperature profile yields

$$k\frac{\partial T}{\partial y}\Big|_{y=0} = \frac{a\rho_f C_{p_f} U}{2}\frac{dT_f}{dx} = \frac{a\rho_f C_{p_f} U}{2}\frac{d\Theta_f}{dx} = \frac{-k\Theta_f}{\beta a} \tag{4.29}$$

which can be used to eliminate all terms containing Θ_f in equation (4.28). The resulting equations can be solved for p

$$p = \frac{\rho C_p}{\rho_f C_{p_f}} - \frac{1}{2} \equiv \eta - \frac{1}{2} \tag{4.30}$$

where η is defined as shown and is of the order of magnitude 10^{-3} for air and glass. The approximation that $p \cong -1/2$ can be made.

Differentiating equation (4.3) with respect to y and evaluating at $y = 0$ reduces to

$$\left[\frac{\partial u}{\partial y}\frac{\partial T}{\partial x} + U\frac{\partial^2 T}{\partial x \partial y}\right]_{y=0} = \frac{k}{\rho C_p}\left[\frac{\partial^3 T}{\partial y^3} - \frac{1}{a}\frac{\partial^2}{\partial y^2} - \frac{1}{a^2}\frac{\partial T}{\partial y}\right]_{y=0}. \tag{4.31}$$

Evaluating this equation and using equation (4.29) to eliminate $d\Theta_f/dx$ yields

$$q = \frac{1}{3} - \frac{1}{3}\eta\left(\frac{1}{\alpha} + \frac{1}{\beta}\right) - \frac{\rho C_p a^2 U}{6k\beta}\frac{d\beta}{dx}. \tag{4.32}$$

Again η is of the order of magnitude 10^{-3}. An order of magnitude of the last term in equation (4.32) can be made by considering individual values. Evaluating air properties at $T_e = 350\ K$ yields $\rho = 1.012\ kg/m^3$, $C_p = 1007\ J/kgK$, and $k = .0300\ W/mK$. The value of β will vary between zero and 7. The value of $d\beta/dx$ can be estimated as $\Delta\beta/\Delta x$ over a short interval. The largest change in β will occur over the initial short interval of fiber length from $x = 0$ to $x = .01\ m$. The change in β over this interval is from 0 to 5 for a 10 μm diameter fiber moving at 60 m/sec. The value of $d\beta/dx$ is then approximately $500/m$. Taking $\beta \sim 1$ over this interval, the final term in equation (4.32) can be estimated as $4 * 10^{-3}$. This value is much less than 1/3, and the approximation $q \cong 1/3$ can be made.

With $p = -1/2$ and $q = 1/3$, the temperature profile becomes

$$\frac{\Theta}{\Theta_f} = 1 - \frac{1}{\beta}\left(\frac{y}{a} - \frac{1}{2}\frac{y^2}{a^2} + \frac{1}{3}\frac{y^3}{a^3}\right) \quad \text{for} \quad y \leq \delta_T \tag{4.33}$$

which is the first three terms of the logarithmic expansion[5], so that the temperature profile takes on the same form as the velocity profile [20].

$$\frac{u}{U} = 1 - \frac{1}{\alpha} ln\left(1 + \frac{y}{a}\right) \quad \text{for} \quad y \leq \delta \tag{4.34}$$

$$\frac{\Theta}{\Theta_f} = 1 - \frac{1}{\beta} ln\left(1 + \frac{y}{a}\right) \quad \text{for} \quad y \leq \delta_T \tag{4.35}$$

Like the boundary layer thickness, a thermal boundary layer thickness δ_T can be evaluated from the temperature profile and becomes $\delta_T = a(e^{\beta} - 1)$. With the velocity and temperature profile, the energy integral (eqn. 4.10) can be evaluated with the assumption that $\delta \leq \delta_T$ (i.e. $Pr \leq 1$) and the resulting equation becomes

[5] $ln(1 + x) = x - \frac{x^2}{2} + \frac{x^3}{3} - \ldots$ for x sufficiently small

$$\frac{d}{dx}\left(\frac{\Theta_f}{\alpha\beta}\left[e^{2\alpha}(\beta-\alpha+1)-(2\alpha\beta+\alpha+\beta+1)\right]\right)=\frac{4k\Theta_f}{\rho C_p a^2 U\beta} \tag{4.36}$$

The factor $d\alpha/dx$ can be eliminated from the evaluation of equation (4.36) by differentiating equation (4.11) with respect to x.

$$\frac{d\alpha}{dx}=\frac{Ua^2}{2\nu\alpha^2}\left[e^{2\alpha}(\alpha-1)+\alpha+1\right] \tag{4.37}$$

Bourne and Dixon [20] have developed a differential equation for β as a function of α only:[6]

$$\frac{d\beta}{d\alpha}=\frac{\beta}{\alpha}\left[\frac{2}{\alpha}-1+\frac{(\alpha-\beta)(\alpha e^{\alpha}-\ sinh\ \alpha)}{\alpha\ cosh\ \alpha-\ sinh\ \alpha}\right]+\frac{2\eta e^{\alpha}}{Pr\ \alpha^2}\left[(1+\beta)\ sinh\ \alpha-\alpha\ cosh\ \alpha-\alpha\beta e^{-\alpha}\right] \tag{4.38}$$

At $x=0$, $\delta=\delta_T=0$ so $\alpha=\beta=0$ is the initial condition on equation (4.38), but at $x=0$ the equation is of an indeterminant form. To evaluate β for small values of α, a series expansion can be used where β can be approximated as

$$\beta=a_1\alpha+a_2\alpha^2+a_3\alpha^3+... \tag{4.39}$$

$$a_1=\frac{1}{2}\frac{(Pr+2)}{Pr}$$

$$a_2=\frac{(Pr-1)(Pr+2)+4\eta}{9\ Pr\ (Pr+1)}$$

[6] All terms containing x, Θ_f and $d\Theta_f/dx$ have been eliminated from the equation.

$$a_3 = \frac{(Pr-1)(Pr+2)(3\ Pr^2 - 4\ Pr - 2) + 60(3\ Pr^2 + Pr + 2)\eta + 360\eta^2}{270(Pr+1)^2(3\ Pr+2)}$$

Equation (4.39) is used to evaluate β for α values from 0 to .08. The results from the series expansion are used as initial condition inputs for equation (4.38), which is integrated for some final value of α and the boundary layer temperature profile at the x coordinate corresponding to α can be found. The heat loss from the fiber can be evaluated by

$$q_c = -2\pi ak\frac{\partial T}{\partial y}\Big|_{y=0}\Delta x = -2\pi ak\left(\frac{-\Theta_f}{\beta a}\right)\Delta x = \frac{2\pi k\Theta_f}{\beta}\Delta x \tag{4.40}$$

with units of *Watts*. This equation can be solved numerically over small intervals of fiber length to obtain the entire fiber temperature profile as a function of x. The numerical solution method will be discussed in detail once the spray model has been developed.

Chapter 5

Spray Cooling of Glass Fibers

This chapter covers the development of the spray cooling model. It extends the boundary layer and heat transfer solutions developed for the no-spray case (Chapter 4). The effect of the water spray is to increase the cooling rate of the glass fibers. Three separate mechanisms are involved. First is the effect of the spray on bulk properties of the system. Second is the localized effect of spray cooling on the individual fiber boundary layers. Third is the effect of spray on radiation transfer to and from the fiber surface.

5.1 Bulk Property Effects

The addition of spray to a fiber bundle system will have two main bulk effects. The first is to increase the bulk specific heat C_{p_e} of the system. The second is the bulk cooling of the air due to evaporative cooling. These effects occur on a large scale and can be studied by neglecting boundary layer effects.

Bulk Specific Heat

The presence of the spray cloud in the air increases the bulk specific heat of the system. This means that for a given quantity of energy transfer from the fiber, there is a smaller increase in bulk temperature than for dry air (no spray) owing to the energy required to warm the droplets. This effect can be estimated by using a very simple model of the fiber and its surroundings. Assume a single fiber with a known and constant

convective heat transfer coefficient h_c. The heat transfer from the fiber is

$$q(x) = 2\pi a h_c[T_f(x) - T_e(x)]\Delta x \tag{5.1}$$

where T_f is the fiber temperature and T_e is the bulk air temperature. Assume the fiber exists within a rectangular cell with adiabatic sides where air is moving at a uniform velocity U_e parallel to the fiber. All energy removed from the fiber during cooling must be stored in the form of a bulk air temperature increase. Assuming uniform velocity and temperature distribution of air within the cell, an energy balance for an incremental length of fiber, Δx, can be written as

$$\frac{d}{dx}\left(\pi a^2 \rho_f C_{p_f} U_f T_f\right)\Delta x = 2\pi a h_c(T_f - T_e)\Delta x = \frac{d}{dx}\left[\rho_e C_{p_e}(z_1 z_2) U_e T_e\right]\Delta x \tag{5.2}$$

where a is the fiber radius, z_1 and z_2 are cell dimensions, ρ_e is the bulk density of the air and water spray, and C_{p_e} is the bulk specific heat. Bulk properties ρ_e and C_{p_e} are dependent on spray density and droplet size. For a 1 m^3 control volume, the bulk density can be found by calculating the mass of water using

$$m_w = \rho_w n_0 \frac{4\pi}{3}\left(\frac{D}{2}\right)^3 \tag{5.3}$$

where n_0 is the droplet density in $drops/m^3$, D is the droplet diameter, and ρ_w is the water density. The mass of air is simply the air density ρ times the air volume, which is essentially 1 m^3. Bulk density is $\rho_e = (m_{H_2O} + m_a)$. Bulk specific heat is given by

$$C_{p_e} = \frac{m_a C_{p_a} + m_w C_{p_w}}{m_a + m_w} \tag{5.4}$$

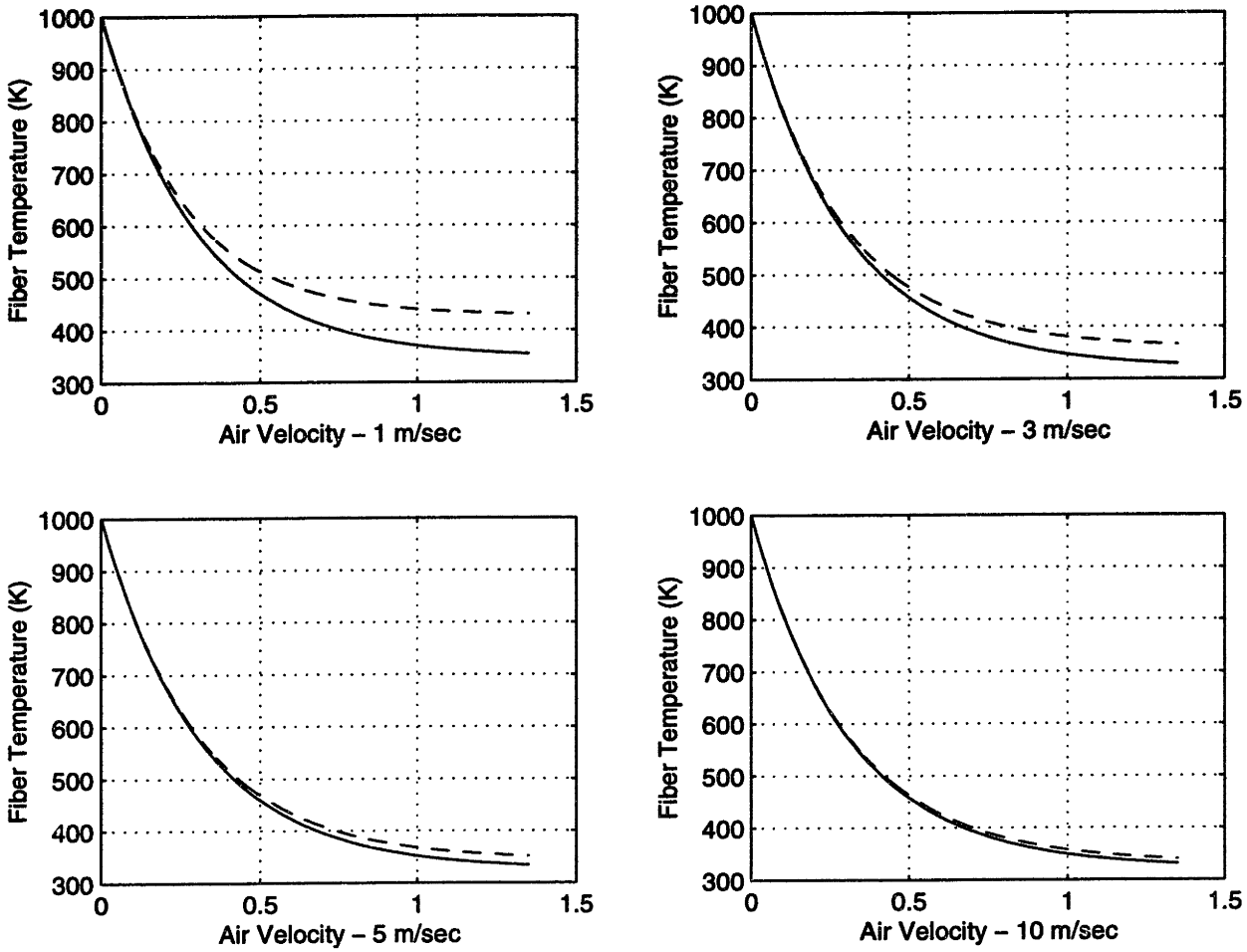

Figure 5.1: Fiber temperature profiles for spray cooled and no-spray operation based on bulk specific heat effects only.

For given initial fiber and bulk temperatures, the temperature profiles for the fiber and air/spray mixture can be calculated. The effect of adding spray to the air is to increase C_{p_e} and ρ_e which will result in a slower increase in bulk temperature. This will maintain a lower ambient temperature (T_e) over the length of the fiber and the heat transfer from the fiber over a given length will be greater. Fig. 5.1 shows the fiber temperature profile for the no-spray and spray cooled case for bulk air velocities from 1 to 10 m/sec. All graphs are for a 10 μm diameter fiber being drawn at 60 m/sec with an initial fiber temperature of 1000 K and an initial bulk air temperature of 320 K. The fiber cell dimensions are 1 cm by 1 cm. The spray cooled condition is for a spray density of 5000 $drops/cm^3$ with a representative drop diameter of 70 μm. The effect

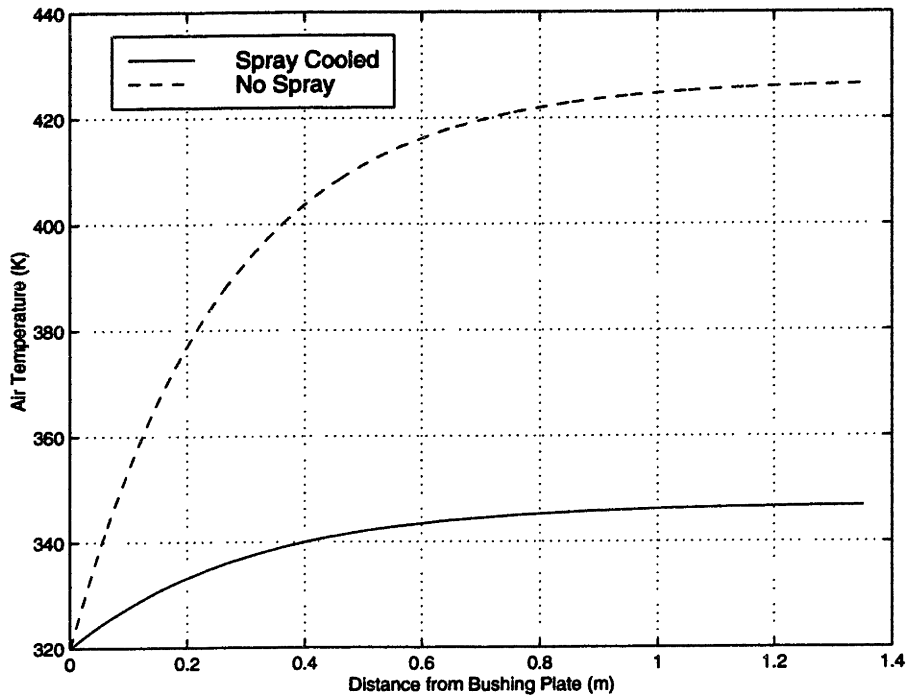

Figure 5.2: Air temperature profile for spray cooled and no-spray operation. (1 m/sec air velocity)

of the spray on the fiber temperature profile is cumulative along the fiber, so bulk specific heat effects have little effect on the region close to the bushing plate where a large portion of the fiber cooling occurs. The effect of spray on the bulk air temperature can be easily seen in Fig. 5.2. This graph is for a bulk air velocity of 1 m/sec and the same spray conditions as stated above. As can be seen in Fig. 5.1, the effect of increasing the bulk specific heat C_{p_e} of the system on fiber temperature profile is reduced with increasing bulk air velocities. At 1 m/sec, the temperature difference at 1 m from the bushing plate is 80 K, but at 3 m/sec the difference is reduced to 25 K and at 5 m/sec the temperature difference is only 10 K. This effect will also depend on the size of the fiber cell (i.e. fiber spacing). The closer the fiber spacing, the smaller the cell size and the greater the effect of bulk specific heat on keeping the bulk air temperature low.

Bulk Evaporation

Evaporative cooling of the air has a similar effect to the bulk C_p in that it increases the driving force $(T_f - T_e)$ by decreasing T_e. The amount of decrease of T_e is dependent on initial T_e values, relative humidity of the

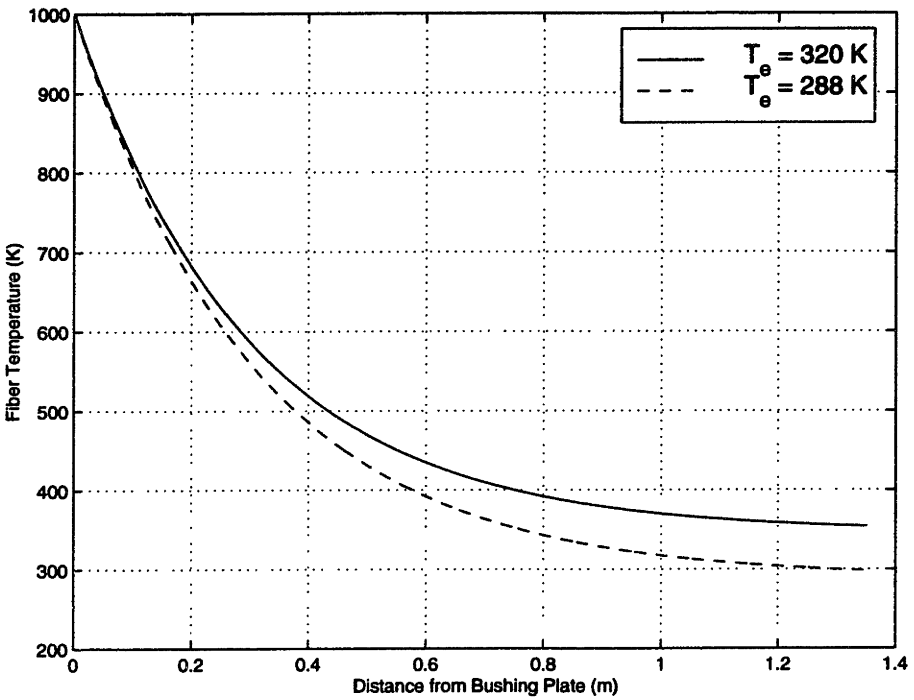

Figure 5.3: Fiber temperature profile for bulk evaporative cooling effects for 0% relative humidity and 1 m/sec bulk air velocity

air, spray density and spray size distribution. The maximum reduction in ambient temperature would be to decrease the temperature to the wet bulb temperature. This value can be quickly calculated using a psychometric chart [21]. For dry air at 323 $K(50°C)$, the wet bulb temperature is 288 $K(18°C)$. Again, assuming a constant h_c and this time assuming a constant T_e, the fiber temperature profile for $T_e = 320\ K$ and $T_e = 288\ K$ is plotted in Fig. 5.3 for an air velocity of 1 m/sec. At 1 m from the bushing plate, the temperature difference is $\sim 50\ K$. Actual cooling of the air will be much less than predicted by wet-bulb temperatures due to nonzero relative humidity and incomplete evaporation. Evaporative cooling will have a much stronger effect at higher ambient temperatures (i.e. near the bushing plate). Here the evaporative cooling will dominate over bulk specific heat effects and will tend to decrease the ambient temperatures.

Combined Bulk Effects

The results from the bulk specific heat and evaporation analysis can be used to simplify the numerical model of the fiber bundle. On the outside of the bundle with slower air velocities where the spray densities

are higher, bulk specific heat effects tend to keep the air temperature level. On the inside of the bundle, lower spray densities are compensated for by higher bulk velocities, which again tends to keep the bulk air temperature level. Near the bushing plate, bulk evaporation will reduce the ambient temperatures more than at other positions in the fiber bundle. The combined effect of bulk specific heat and bulk evaporation will be to make the temperature profile more uniform throughout the fiber bundle and to prevent a large temperature increase of the air due to energy transfer from the fibers.

5.2 Boundary Layer Spray Cooling

With the assumption that no drops touch the surface of the fiber, the effect of evaporation on the thermal boundary layer must be to change the shape of the temperature profile by cooling the air in the boundary layer. Since the convective heat transfer from the surface of the fiber is given by

$$q_c = -2\pi a k \frac{\partial T}{\partial y}\Big|_{y=0} \Delta x \tag{5.5}$$

to increase the cooling rate, the $\partial T/\partial y$ term must increase. The analysis to determine the change in the temperature profile follows very closely the derivation of the no-spray solution. The energy equation in the boundary layer with spray cooling becomes

$$u\frac{\partial T}{\partial x} + v\frac{\partial T}{\partial y} = \frac{k}{\rho C_p}\frac{1}{(a+y)}\frac{\partial}{\partial y}\left((a+y)\frac{\partial T}{\partial y}\right) + \frac{1}{\rho C_p}\dot{q}_e \tag{5.6}$$

where $\dot{q}_e$ is the volumetric heat absorption by evaporation in W/m^3. Assuming that the spray has no effect on the shape of the velocity boundary layer, the velocity profile in the boundary layer can be expressed as

$$\frac{u}{U} = 1 - \frac{1}{\alpha} ln\left(1 + \frac{y}{a}\right) \quad \text{for} \quad y \leq \delta.$$

Since the spray has no effect on the velocity boundary layer, the relationship between x and α remains unchanged, i.e.

$$\frac{2\nu x}{Ua^2} = \frac{e^{2\alpha} - 1}{\alpha} + Ei(2\alpha) + ln(2\alpha) + \gamma - 2.$$

Assume a temperature profile of the same form as before

$$\frac{\Theta}{\Theta_f} = 1 - \frac{1}{\beta}\left(\frac{y}{a} + p\frac{y^2}{a^2} + q\frac{y^3}{a^3}\right) \tag{5.7}$$

where β is a function of x only. The solution $p = \eta - 1/2$ remains unchanged with the addition of evaporative cooling. The solution for q is affected by the presence of the evaporation term. Differentiating equation (5.6) with respect to y, the equation becomes

$$\frac{\partial u}{\partial y}\frac{\partial T}{\partial x} + u\frac{\partial^2 T}{\partial x \partial y} + \frac{\partial v}{\partial y}\frac{\partial T}{\partial y} + v\frac{\partial^2 T}{\partial y^2} = \frac{k}{\rho C_p}\left[\frac{\partial^3 T}{\partial y^3} + \frac{1}{a+y}\frac{\partial^2 T}{\partial y^2} - \frac{1}{(a+y)^2}\frac{\partial T}{\partial y}\right] + \frac{1}{\rho C_p}\frac{\partial}{\partial y}\dot{q}_e(a+y). \tag{5.8}$$

From continuity (Eqn.4.1)

$$\text{at} \quad y = 0, \quad \frac{\partial u}{\partial x} = \frac{\partial U}{\partial x} = 0, \quad v = 0 \quad \rightarrow \quad \frac{\partial v}{\partial y} = 0. \tag{5.9}$$

Using this equation to eliminate radial velocity terms and evaluating equation (5.8) at $y = 0$, it can be shown that

$$\frac{-U}{a}\frac{\partial \Theta_f}{\partial x}\left(\frac{1}{\alpha} + \frac{1}{\beta}\right) + \frac{U\Theta_f}{a\beta^2}\frac{\partial \beta}{\partial x} = \frac{k\Theta_f}{\rho C_p \beta a^3}(1 - 2p - 6q) + \frac{a}{\rho C_p}\frac{\partial}{\partial y}\dot{q}_e\Big|_{y=0}. \tag{5.10}$$

Substituting $p = -1/2$ and using the results from equation (4.29)

$$\frac{d\Theta_f}{dx} = \frac{-2k\Theta_f}{\beta a^2 \rho_f C_{p_f} U} \tag{5.11}$$

to eliminate the $d\Theta_f/dx$ term, q can be found

$$q = \frac{1}{3} - \frac{1}{3}\eta\left(\frac{1}{\alpha} + \frac{1}{\beta}\right) - \frac{Ua^2\rho C_p}{6\beta k}\frac{d\beta}{dx} + \frac{\beta a^4}{6\rho C_p k \Theta_f}\frac{\partial}{\partial y}\dot{q}_e\Big|_{y=0}. \tag{5.12}$$

Again the second and third terms on the right hand side of equation (5.12) are of orders of magnitude 10^{-3} and $4 * 10^{-3}$ respectively as was calculated in Section 4.2 and can be neglected. The last term in equation (5.12) is of the order of magnitude $5 * 10^{-14}$ (see Appendix C) and can also be neglected compared to 1/3. With these values assumed small, the approximation that $q \cong 1/3$ can again be made. With $q = 1/3$, the logarithmic approximation to the temperature profile is

$$\frac{\Theta}{\Theta_f} = 1 - \frac{1}{\beta} ln\left(1 + \frac{y}{a}\right) \quad \text{for} \quad y \leq \delta_T \tag{5.13}$$

$$\frac{\Theta}{\Theta_f} = 0 \quad \text{for} \quad y \geq \delta_T$$

where β is only a function of x. This means that the addition of spray cooling to the thermal boundary layer doesn't affect the logarithmic shape of the temperature profile, but simply changes the thickness of the thermal boundary layer[1].

An evaporation term can be added to the boundary layer control volume (Fig. 4.2) from which the energy integral can be expressed as

$$\frac{d}{dx}\int_0^\infty 2\pi\rho C_p(a+y)u(y)T(y)dy\Delta x = -2\pi ak\frac{\partial T}{\partial y}\Big|_{y=0}\Delta x + \int_0^\infty 2\pi\dot{q}_e(a+y)dy\Delta x \tag{5.14}$$

where $\dot{q}_e$ is the evaporative energy term which is expected to be negative. The integration limits in the left hand side of equation (5.14) become 0 to δ if $\alpha \leq \beta$ ($\delta \leq \delta_T$) and 0 to δ_T if $\alpha > \beta$ ($\delta > \delta_T$). After substituting for the velocity and temperature profiles and evaluating the integral on the left hand side of the equation with the assumption $\delta \leq \delta_T$, equation (5.14) becomes

$$\frac{d}{dx}\left[\frac{1}{4}\frac{a^2\Theta_f U e^{2\alpha}(1-\alpha+\beta)}{\alpha\beta} - \frac{1}{4}\frac{a^2\Theta_f U(2\alpha\beta+\alpha+1+\beta)}{\alpha\beta}\right] = \frac{-ka}{\rho C_p}\left(\frac{-\Theta_f}{a\beta}\right) + \frac{1}{\rho C_p}\int_0^{\delta_T}\dot{q}_e(a+y)dy. \tag{5.15}$$

Expanding the d/dx term in equation (5.15) leads to an expression in $d\alpha/dx$, $d\Theta_f/dx$ and $d\beta/dx$.

$$\frac{1}{4}\frac{a^2\Theta_f U\left(\alpha e^{2\alpha} - e^{2\alpha} + \alpha + 1\right)}{\alpha\beta}\frac{d\beta}{dx} + \frac{1}{4}\frac{a^2\Theta_f U\left(2\alpha e^{2\alpha} - 2\alpha^2 e^{2\alpha} + 2\alpha\beta e^{2\alpha} - e^{2\alpha} - \beta e^{2\alpha} + 1 + \beta\right)}{\alpha^2\beta}\frac{d\alpha}{dx} + \frac{1}{4}\frac{a^2 U\left(e^{2\alpha} - \alpha e^{2\alpha} + \beta e^{2\alpha} - 2\alpha\beta - \alpha - 1 - \beta\right)}{\alpha\beta}\frac{d\Theta_f}{dx} = \frac{k\Theta_f}{\rho C_p\beta} + \frac{1}{\rho C_p}\int_0^{\delta_T}\dot{q}_e(a+y)dy \tag{5.16}$$

Using equation (5.11) to eliminate $d\Theta_f/dx$ and using

[1]The temperature profiles from any two fiber positions can be overlaid simply by applying a scaling factor to one of the profiles.

$$\frac{d\alpha}{dx} = \frac{2\nu\alpha^2}{Ua^2\left(-e^{2\alpha} + \alpha e^{2\alpha} + \alpha + 1\right)}$$

to eliminate $d\alpha/dx$ and to transform $d\beta/dx$ to $d\beta/d\alpha$, a differential equation for β can be found,

$$\frac{d\beta}{d\alpha} = \frac{2\beta}{\alpha\, Pr} + \frac{\eta}{\alpha^2\, Pr}\left(e^{2\alpha} - \alpha e^{2\alpha} + \beta e^{2\alpha} - 2\alpha\beta - \alpha - 1 - \beta\right)$$
$$- \frac{\beta}{\alpha}\frac{\left(2\alpha e^{2\alpha} - 2\alpha^2 e^{2\alpha} + 2\alpha\beta e^{2\alpha} - e^{2\alpha} - \beta e^{2\alpha} + 1 + \beta\right)}{\left(-e^{2\alpha} + \alpha e^{2\alpha} + \alpha + 1\right)} + \frac{2\beta^2}{\Theta_f \alpha k Pr}\int_0^{\delta_T} \dot{q}_e(a+y)dy \quad (5.17)$$

where Pr is the Prandtl number and $\eta = \rho C_p/\rho_f C_{p_f}$. This result is correct as long as the velocity boundary layer δ is smaller than the thermal boundary layer δ_T. This is the normal case for a Prandtl number less than unity. With the addition of spray, the thermal boundary layer will actually start to shrink until the thermal boundary layer will be fully contained by the velocity boundary layer. When this happens, the integration across the boundary layer of equation (5.14) is evaluated from 0 to $\delta_T = a(e^{\beta} - 1)$ rather than 0 to $\delta = a(e^{\alpha} - 1)$. Using the same method used to develop equation (5.17), the differential equation for β becomes

$$\frac{d\beta}{d\alpha} = \frac{-2\alpha\beta}{Pr}\left[\frac{\left(2\frac{e^{2\alpha}}{\alpha} - \frac{e^{2\alpha}-1}{\alpha^2} - \frac{e^{2\alpha}}{\alpha} + \frac{1}{\alpha}\right)}{\left(-2\beta e^{2\beta} - 2\alpha\beta e^{2\beta} + 2\beta^2 e^{2\beta} + e^{2\beta} + \alpha e^{2\beta} - \alpha - 1\right)}\right]$$
$$- \frac{2\alpha\beta^2}{\Theta_f k Pr}\left[\frac{\left(2\frac{e^{2\alpha}}{\alpha} - \frac{e^{2\alpha}-1}{\alpha^2} - \frac{e^{2\alpha}}{\alpha} + \frac{1}{\alpha}\right)}{\left(-2\beta e^{2\beta} - 2\alpha\beta e^{2\beta} + 2\beta^2 e^{2\beta} + e^{2\beta} + \alpha e^{2\beta} - \alpha - 1\right)}\right]\int_0^{\delta_T} \dot{q}_e(a+y)dy$$
$$+ \frac{\eta}{Pr}\left(-e^{2\beta} - \alpha e^{2\beta} + \beta e^{2\beta} + 2\alpha\beta + \alpha + 1 + \beta\right)\left[\frac{\left(2\frac{e^{2\alpha}}{\alpha} - \frac{e^{2\alpha}-1}{\alpha^2} - \frac{e^{2\alpha}}{\alpha} + \frac{1}{\alpha}\right)}{\left(-2\beta e^{2\beta} - 2\alpha\beta e^{2\beta} + 2\beta^2 e^{2\beta} + e^{2\beta} + \alpha e^{2\beta} - \alpha - 1\right)}\right]$$
$$+ \frac{\beta}{\alpha}\frac{\left(-e^{2\beta} + \beta e^{2\beta} + 1 + \beta\right)}{\left(-2\beta e^{2\beta} - 2\alpha\beta e^{2\beta} + 2\beta^2 e^{2\beta} + e^{2\beta} + \alpha e^{2\beta} - \alpha - 1\right)} \quad (5.18)$$

when $\alpha \geq \beta$. We no longer have differential equations for β just in terms of α, as in the no-spray analysis. Now the presence of Θ_f in equations (5.17) and (5.18) prevents direct integration of β with α. Also, the

evaporation term will be shown to be a function of Θ_f. Equations (5.17) and (5.18) can be used to evaluate the change in the thermal boundary layer due to normal boundary layer growth and due to evaporation within the boundary layer. The value of β can be evaluated as a function of α which in turn can be used to evaluate the fiber position. Knowledge of the thermal boundary layer at any point on the fiber can then be used to evaluate the heat transfer from the fiber to the air.

5.3 Radiation Model

In order to estimate the effect of water spray on radiative heat transfer to and from the fiber, a basic analysis of radiation with no spray is needed. The two main modes of radiative heating that affect the fiber cooling are radiative transfer from the bushing plate to the fiber and from the fiber to the surrounding environment. The radiative transfer from the bushing plate to the fiber can be evaluated using a worst case model, and the radiative transfer from the fiber to the environment can be evaluated based on a view factor of 1 from the fiber to its surroundings.

Bushing Plate Radiative Heating

The radiative heat transfer from the bushing plate to a fiber will depend on fiber size, velocity and position on the bushing plate (edge vs. center), as well as size of the bushing plate. Rather than attempting to develop a model for all geometric conditions, a worst case model will be formed that will estimate the maximum amount of heat transfer from the the bushing plate to a drawn fiber. Assuming the bushing plate is a black body[2], the radiative heat transfer is calculated by

$$q_{rad} = \sigma \frac{\left(\frac{A_f \epsilon}{1-\epsilon}\right)(A_p F_{p\to f})T_p^4 + \left(\frac{A_f \epsilon}{1-\epsilon}\right)^2 T_f^4 + \left(\frac{A_f \epsilon}{1-\epsilon}\right)(A_f F_{f\to e})T_e^4}{\left(\frac{A_f \epsilon}{1-\epsilon}\right) + A_f F_{f-e} + A_p F_{p\to f}} - \frac{A_f \epsilon}{1-\epsilon}\sigma T_f^4 \tag{5.19}$$

[2]The bushing plate is made of platinum, and the actual emissivity of a platinum plate is in the range of .054 – .104 [22]. The assumption of the bushing plate as a black body will still be made in order to estimate the largest possible heat transfer to the fiber from radiative heating.

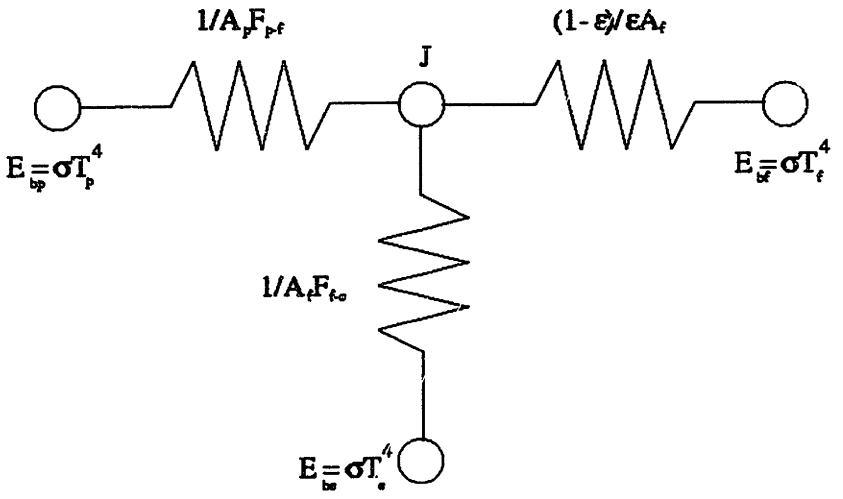

Figure 5.4: Thermal radiation circuit for modeling radiative heat transfer from bushing plate to fiber.

where σ is the Boltzmann constant, T_p is the bushing plate temperature, T_f is the fiber temperature, T_e is the environmental temperature, $F_{p\to f}$ is the radiation view factor from the bushing plate to the fiber, $F_{f\to e}$ is the radiation view factor from the fiber to the environment, ϵ is the fiber emissivity, and A_p and A_f are the bushing plate and fiber surface areas respectively. This equation is obtained by solving the thermal radiation circuit shown in Fig. 5.4 for heat transfer to the fiber surface. The radiation view factor from the bushing plate to the fiber can be calculated by modeling the bushing plate as a round disk with the fiber a cylinder normal to the surface of the disk. According to Rea [23], the view factor is

$$2\pi F_{1-2} = 2\pi F_{f-p} = \cos^{-1}\frac{l^2 - R^2 + r^2}{l^2 + R^2 - r^2} - \frac{r}{2l}\left[\left(\frac{\left(l^2+R^2+r^2\right)^2}{r^4} - 4\left(\frac{R}{r}\right)^2\right)^{\frac{1}{2}}\cos^{-1}\frac{r\left(l^2-R^2+r^2\right)}{R\left(l^2+R^2-r^2\right)}\right] - \frac{r}{2l}\left[\left(\frac{l^2-R^2+r^2}{r^2}\right)\sin^{-1}\left(\frac{r}{R}\right) - \frac{\pi}{2}\left(\frac{l^2+R^2-r^2}{r^2}\right)\right] \quad (5.20)$$

for the geometry shown in Fig. 5.5. The view factor from the bushing plate to the fiber can then be calculated using view factor algebra, i.e.

$$A_f F_{f\to p} = A_p F_{p\to f}. \quad (5.21)$$

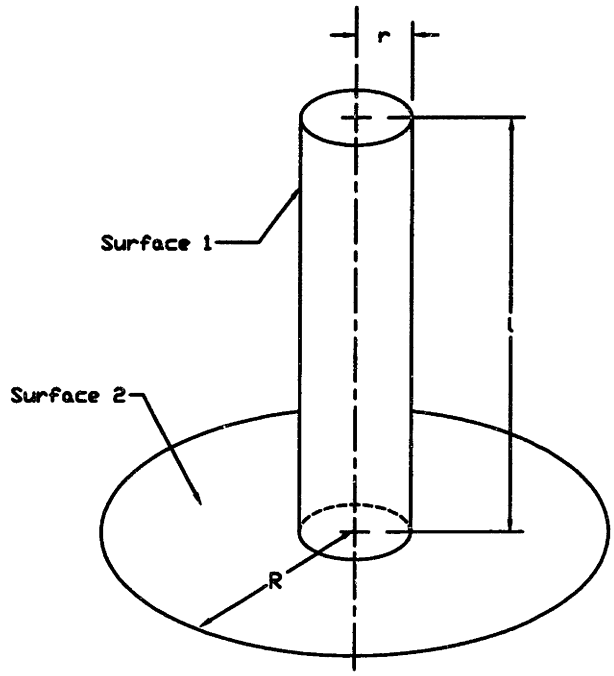

Figure 5.5: Geometry to generate view factor.

The view factor from the fiber to the environment is $F_{f\to e} = 1 - F_{f\to p}$. By selecting a disk with a radius at least the size of the maximum rectangular dimension seen by a fiber at the middle of the bushing plate, the view factor will be at least equal to that of a fiber and rectangular plate[3].

In order to obtain an estimate of the magnitude of temperature increase in the fiber due to radiation, the worst case scenario can be solved for a uniform fiber and environment temperature of 350 K. Over 1 m of fiber length with a 10 μm diameter traveling at 60 m/sec and a bushing plate temperature of 1500 K, the maximum temperature increase[4] of the fiber due to radiative heating from the bushing plate is 12.8 K. The actual temperature increase will be less due to a couple of factors. The fiber temperature is not a uniform 350 K, but has a temperature profile from 1500 K at the base, to 350 K at the tip of the fiber. The bushing plate is not a black surface, so emitted radiative intensity will be less. The actual fiber bundle systems have water cooled radiation shields near the bushing plates. These shields will reduce the view factor between the bushing plate and fiber. While a 12.8 K temperature increase may seem very small for a large unshielded

[3]The calculated radiative heat transfer will actually be greater due to increased bushing plate surface area.
[4]This is for a round bushing plate with a 30 cm radius and a glass emissivity of 0.3.

bushing plate at 1500 K, this can be justified by considering that the surface area of the fiber is very small and also that the residence time[5] ($\sim$ .015 *seconds*) is very small due to the high drawing speeds. To include the radiative heating in a numerical model, the radiative heating over a small incremental length of fiber at any position needs to be calculated. In order to do this, the view factor from the bushing plate to the incremental section of fiber can be calculated using

$$F_{p\to\Delta x} = F_{p\to f_{L+\Delta x}} - F_{p\to f_L} \tag{5.22}$$

where $F_{p\to f_L}$ is the view factor from the bushing plate to the fiber evaluated for a fiber length of L, and $F_{p\to f_{L+\Delta x}}$ is evaluated for a fiber length of $L + \Delta x$.

Fiber to Environment Radiative Cooling

Due to the small surface area of each fiber in the bundle, the view factor from one fiber to another is so small that the radiation view factor between any two fibers is essentially zero and can be neglected. With this assumption, the only two surfaces that the fiber sees are the bushing plate and the environment. Since the environment has a very large surface area compared to the fiber, it can be considered as a black body and the radiation heat transfer from the fiber to the environment can be written as

$$q_{rad} = 2\pi a\epsilon\sigma F_{f\to e}(T_f^4 - T_{env}^4)\Delta x \tag{5.23}$$

with units of $Watts$. This result can be easily incorporated into a numerical solution of the fiber temperature profile. The presence of the radiation shields near the bushing plates will drastically reduce the view factor from the bushing plate to the fiber for fiber positions close to the bushing plate. It has been shown that the radiation heat transfer from the bushing plate to a fiber is small and the presence of the radiation shields will

[5]Time that an incremental length of fiber surface is exposed to radiation.

only reduce this number. This means the dominant form of radiation is from the fiber to the environment and radiation from the bushing plate can be neglected. Therefore the view factor from the fiber to the environment can be considered 1 for all values of x.

Chapter 6

Evaluation of Evaporation Term

This chapter solves for the evaporation term in the boundary layer. It starts with an analysis of evaporation from a single droplet. It then uses these results to develop an expression for the total evaporation rate at any point in a fiber boundary layer. The chapter concludes with justification of the assumptions used to model the boundary layer evaporation.

6.1 Single Drop Evaporation

Calculation of the evaporation rate of a drop of water involves the simultaneous calculation of heat and mass transfer. The evaporation rate is determined by a surface energy balance on the droplet where convective heat transfer just balances the energy of vaporization assuming that the droplet has cooled to the wet bulb temperature. This can be expressed mathematically by

$$h_c(T_e - T_s)A = g_{m1}(m_{1,s} - m_{1,e})h_{fg}A \tag{6.1}$$

where h_c is the convective heat transfer coefficient, T_s is the droplet surface temperature, T_e is the environmental temperature, $g_{m,1}$ is the mass conductance, $m_{1,s}$ is the mass fraction of water in air evaluated at T_s,

$m_{1,e}$ is the environmental mass fraction of water in air, h_{fg} is latent heat of vaporization of water at T_s, and A is the droplet surface area. This equation can be rearranged to find

$$m_{1,e} = m_{1,s} - \frac{h_c}{g_{m1} h_{fg}}(T_e - T_s) \tag{6.2}$$

where the fraction in front of the temperature term, for purely diffusive low rate mass transfer, can be simplified with the heat and mass transfer analogy [24]

$$\frac{h_c / C_{p_{air}}}{g_{m,1}} = \frac{1}{Le} = \frac{1}{1.13} \tag{6.3}$$

where $Le = \rho C_p \mathfrak{D}_{12}/k$ is the Lewis number. The evaluation of the evaporation now becomes an iterative process of picking a T_s and evaluating $m_{1,s}$ using

$$m_{1,s} = m_{1,e} + \frac{C_{p_{air}}}{1.13 h_{fg}}(T_e - T_s) \tag{6.4}$$

and comparing this value of $m_{1,s}$ to equilibrium values of $m_{1,s}$ evaluated at T_s using vapor pressure charts and reference data. Convergence on T_s usually takes three to four iterations depending on the initial guess for T_s.

The mass transfer from the droplet is equal to the rate of change of mass of the droplet.

$$g_{m,1}(m_{1,e} - m_{1,s})A = \frac{d}{dt}\left(\frac{\pi \rho_w D^3}{6}\right) = \frac{\pi \rho_w D^2}{2}\frac{dD}{dt} \tag{6.5}$$

where D is the drop diameter and $A = \pi D^2$ is the drop surface area. In the limiting case where $Re \to 0$ (i.e. a small droplet moving at low speed relative to the air), then

$$\frac{g_{m,1}D}{\rho\mathfrak{D}_{12}} = 2 \tag{6.6}$$

where $\mathfrak{D}_{12}$ is the binary diffusion coefficient of water vapor in air. Solving for the rate of change of the drop diameter with time yields

$$\frac{dD}{dt} = \frac{-4\rho\mathfrak{D}_{12}}{\rho_w D}(m_{1,s} - m_{1,e}) \tag{6.7}$$

which can be integrated to find

$$D^2 - D_0^2 = \frac{-8\rho\mathfrak{D}_{12}}{\rho_w}(m_{1,s} - m_{1,e})t \equiv -k_{evap}t. \tag{6.8}$$

This equation can be solved for diameter as a function of time.

$$D = \sqrt{D_0^2 - k_{evap}t}. \tag{6.9}$$

The evaporation constant, k_{evap}, can be evaluated once the iterative solution for T_s is obtained. This solution for the evaporation constant is for low mass transfer rate theory and starts to break down when the droplet surface temperature approaches $50°C(323\ K)$[24]. With droplet surface temperatures of $50°C$ and higher, the mass transfer from the droplet becomes so large that the resulting velocity field affects heat transfer to the droplet. The motion of the water vapor away from the droplet surface will reduce the heat transfer to the droplet. This means that for high droplet temperatures, low mass transfer rate theory will over estimate the evaporation coefficient and the predicted evaporation rate will be too high. Using low mass theory, a droplet surface temperature of $44°C(317\ K)$ corresponds to ambient conditions of 500 K and 0% relative

humidity. For all ambient temperatures above this point, high mass transfer rate theory must be used to predict the evaporation rate.

Just as in the low mass theory, solution of the evaporation rate in high mass transfer theory requires an iterative approach. The evaporation rate in dry air with 0% relative humidity can be found be simultaneously solving [24]

$$ln\left(\frac{1}{1-m_{1,s}}\right) = \frac{k/C_{pl}}{\rho\mathfrak{D}_{12}} ln\left(1+\frac{C_{pl}(T_e-T_s)}{h_{fg}}\right) \tag{6.10}$$

$$m_{1,s} = m_{1,s}(T_s.P) \tag{6.11}$$

where $m_{1,s}$ is the mass fraction of water vapor in air at the droplet surface temperature T_s. Due to the large temperature gradients involved, the property values in equation (6.10) must be evaluated at a reference temperature. Also, because of the high mass fractions of water vapor at these high temperatures, the properties must be evaluated for air/water vapor mixtures. Dry air property values can no longer be used as in the low mass transfer analysis. Mills [24] recommends use of the a 1/3 rule for evaluation of k, C_{pl}, ρ, and $\mathfrak{D}_{12}$. The reference values are

$$m_{1,r} = m_{1,s} + \frac{1}{3}(m_{1,e} - m_{1,s}) \tag{6.12}$$

$$T_r = T_s + \frac{1}{3}(T_e - T_s) \tag{6.13}$$

where $m_{1,e}$ is the mass fraction of water vapor in air at environmental conditions and is zero for 0% relative humidity. The iterative solution of equations (6.10) and (6.11) yields the droplet surface temperature and water vapor mass fraction $m_{1,s}$. The mass transfer from a droplet is

$$\dot{m} = \frac{2\rho\mathfrak{D}_{12}}{D} ln\left(1 + \frac{m_{1,e} - m_{1,s}}{m_{1,s} - 1}\right) A \tag{6.14}$$

where $A = \pi D^2$ is the droplet surface area and $m_{1,e} = 0$. The rate of change of droplet diameter is

$$D^2 = D_0^2 - \frac{8\rho\mathfrak{D}_{12}}{\rho_w} ln\left(1 + \frac{m_{1,s}}{1 - m_{1,s}}\right) t \equiv D_0^2 - k_{evap} t \tag{6.15}$$

where ρ and $\mathfrak{D}_{12}$ are evaluated for air/water vapor mixtures at the reference temperature T_r defined in equation (6.13). Fig. 6.1 presents the calculated and curve fit data for both low and high mass transfer rate theory for $300\ K \leq T_e \leq 1500\ K$. As can be seen, at higher temperatures, low mass theory can overpredict the evaporation coefficient by a factor of 2. With $T_e = 1500\ K$, high mass transfer rate theory predicts a droplet temperature of $350\ K$ and low mass transfer rate theory predicts a droplet temperature of $361\ K$.

The actual evaporation constant will be somewhere between the two plotted curves in Fig. 6.1. The high mass transfer rate theory predicts evaporation for diffusion into still air, but the drops are actually in a velocity gradient. This velocity gradient will remove the water vapor from around the drop faster than high mass theory predicts. This will reduce the thermal boundary layer thickness which will increase the heat transfer to the drop and therefore the evaporation rate will increase. Low mass rate theory completely neglects the effect of water vapor motion on increasing the thermal boundary layer thickness about the drop. In this case, with a small velocity gradient about each drop, high mass rate theory will underpredict evaporation and low mass rate theory will overpredict, so the actual value will be somewhere between the two curves. The data in Fig. 6.1 have been curve fit to a second order polynomial equation for each theory. The evaporation coefficient k_{evap} can be calculated from

$$k_{evap} = A_1 T(y)^2 + B_1 T(y) + C_1 \tag{6.16}$$

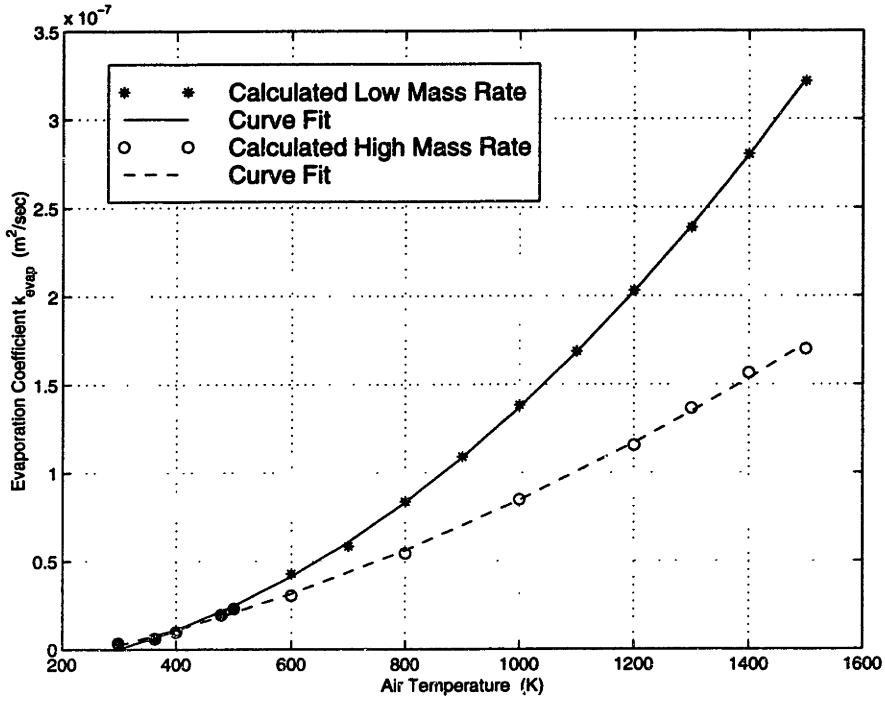

Figure 6.1: Air temperature vs. evaporation constant.

	Low Mass Transfer Rate Theory	High Mass Transfer Rate Theory
A_1	$1.46591 * 10^{-13}$ $[m^2/sec\ K^2]$	$4.98359 * 10^{-14}$ $[m^2/sec\ K^2]$
B_1	$4.76343 * 10^{-12}$ $[m^2/sec\ K]$	$5.26508 * 10^{-11}$ $[m^2/sec\ K]$
C_1	$-1.44065 * 10^{-8}$ $[m^2/sec]$	$-1.80051 * 10^{-8}$ $[m^2/sec]$

Table 6.1: Coefficients for evaporation polynomial.

where $T(y)$ is the ambient temperature in K. The coefficients for high and low mass rate theory are given in Table 6.1.

As will be seen in the results section, which curve fit is used makes no noticeable difference on the final results.

6.2 Boundary Layer Evaporation

With an expression for the evaporation rate from a single drop based on temperature, an expression for the evaporative term within the boundary layer can be developed. Several assumptions need to be made to make

the model manageable. The droplets in the boundary layer are fully entrained and travel at the air velocity corresponding to the radial position of the center of the drop. The evaporation rate is diffusion controlled. The effect of increasing the relative humidity of the air within the boundary layer on evaporation rate is neglected. The transient warm-up time of each drop is short compared to droplet lifetime. The droplets in the boundary layer have a uniform diameter. The droplets in the boundary layer never touch the fiber surface.

The evaporation rate in the boundary layer is proportional to the total droplet surface area, the time duration for evaporation, and the evaporation constant k_{evap}. The total droplet surface area in turn is proportional to the droplet size distribution (SMD) and the droplet density. The time duration is a function of droplet velocity and incremental length of boundary layer over which the evaporation rate is being calculated. The evaporation constant is a strong function of temperature.

Unfortunately, almost all of these parameters vary across the thickness of the boundary layer. The spray density varies from n_0 at the outer edge of the boundary layer to zero at the fiber surface. The droplet velocity is assumed the same as the boundary layer velocity corresponding to the position of the center of the drop and varies from zero at the edge of the boundary layer to U (the fiber velocity) at the surface of the fiber. The temperature, and therefore k_{evap}, varies by up to an order of magnitude across the boundary layer.

This requires the computation of the evaporation rate to be an integral expression over the width of the boundary layer, for a incremental length of fiber Δx. This complicates matters even further because as position along the fiber changes from x to $x + \Delta x$, the temperature and velocity profiles, the boundary layer thickness, and the drop density across the boundary layer all change. Also, as the drops evaporate, the diameter distribution will change.

The item of interest is the total evaporation rate in the boundary layer, and this simply the total droplet surface area times a mass flux due to evaporation. If the interval over which the evaporation rate is calculated is short, then changes in temperature, droplet density and size (i.e. total droplet surface area), and boundary layer thickness are all second order effects on changes in the droplet mass flux compared to evaporation and can be ignored. At the beginning of each interval, the droplet density, temperature, velocity, and boundary

layer thickness are all evaluated locally and then held constant over Δx. To put the problem back into the perspective of the variables associated with the fiber/spray system, the evaporation rate can be expressed as an integral over the boundary layer of the rate of change of the entrained mass of water spray:

$$\int_0^\infty 2\pi \dot{q}_e (a+y) dy \Delta x = \int_0^\infty 2\pi (a+y) \left[\frac{d}{dx} \left(\dot{m}_{drop} \right) \Delta x \right] h_{fg} dy \tag{6.17}$$

where $\dot{m}_{drop}$ is the entrained mass of water spray in the boundary layer and has units $kg/m^2 sec$, and h_{fg} is the latent heat of vaporization. The mass of entrained water at any point along the fiber can be calculated based on the droplet density across the boundary layer. In order to satisfy the assumption that no droplets touch the fiber, a linear droplet density distribution near the fiber is assumed to be of the form

$$n = \frac{n_0 y}{\delta} \tag{6.18}$$

where n_0 is the droplet density ($number\ of\ drops/m^3$) at environmental conditions, and δ is the boundary layer thickness[1]. The mass of water entrained by the boundary layer can now be written as

$$\dot{m}_{drop} = \frac{n_0 y}{\delta} \left[\frac{4\pi}{3} \left(\frac{D}{2} \right)^3 \rho_w \right] \left[U - \frac{U}{\alpha} ln \left(1 + \frac{y}{a} \right) \right] \tag{6.19}$$

where D is the representative droplet diameter of the spray, e.g. Sauter mean diameter SMD. The evaporation term is now simply the change in the total mass of entrained water over a short length Δx. As stated earlier, the velocity, temperature, spray density, and boundary layer thickness are all assumed constant over Δx. The derivative of equation (6.19) now takes on the form

[1] Assuming drops enter the boundary layer with a uniform radial velocity, the closer the drops get to the fiber, the higher their axial velocity. This will result in decreasing droplet density with decreasing distance to the fiber. Additionally, very high temperatures near the fiber will tend to increase the evaporation rate, so that the approximation of no droplets touching the fiber surface seems very reasonable.

$$\frac{d}{dx}(\dot{m}_{drop})_{evap} = \frac{n_0 y}{\delta}\rho_w \frac{\pi}{6}\left(U - \frac{U}{\alpha} ln\left(1+\frac{y}{a}\right)\right)\frac{d}{dx}\left(D^3\right) = \frac{n_0 \rho_w \pi y}{2\delta}\left(U - \frac{U}{\alpha}\left(1+\frac{y}{a}\right)\right)D^2\frac{dD}{dx} \quad (6.20)$$

where the term dD/dx can be evaluated using the equation developed for single drop evaporation (eqn. 6.8). With k_{evap} constant over Δx, then

$$\frac{d}{dx}D = \frac{d}{dx}\left(D_0^2 - k_{evap}t\right)^{\frac{1}{2}} = \frac{1}{2}\left(D_0^2 - k_{evap}t\right)^{-\frac{1}{2}}\left(-k_{evap}\frac{dt}{dx}\right). \quad (6.21)$$

The term dt/dx can be replaced by $1/u(y)$, but this still leaves the t term in the square root. By looking at a control volume, t can be replaced by $\Delta x/u(y)$ for small distances Δx where $u(y)$ can be considered constant. The evaporation constant k_{evap}, can be expressed as a temperature dependent polynomial from a curve fit of the calculated data in Fig. 6.1. As developed in the previous section, a 2nd order equation is used for $k_{evap}(T)$ of the form

$$k_{evap}(T) = A_1 T(y)^2 + B_1 T(y) + C_1.$$

Equation (6.20) now becomes

$$\frac{d}{dx}D = -\frac{1}{2}\left(D_0^2 - \frac{\left[A_1 T(y)^2 + B_1 T(y) + C_1\right]\Delta x}{u(y)}\right)^{-\frac{1}{2}}\left(\frac{A_1 T(y)^2 + B_1 T(y) + C_1}{u(y)}\right) \quad (6.22)$$

where $u(y)$ is the boundary layer velocity profile and $T(y)$ is the boundary layer temperature profile. The change in the entrained mass flow rate in the boundary layer due to evaporation can now be expressed as

$$\frac{d}{dx}\left(\dot{m}_{drop}\right)_{evap} = \frac{-\pi n_0 \rho_w D^2 y}{4\delta} \frac{\left(A_1 T(y)^2 + B_1 T(y) + C_1\right)}{\left[D_0^2 - \frac{\left(A_1 T(y)^2 + B_1 T(y) + C_1\right)\Delta x}{u(y)}\right]^{\frac{1}{2}}} \tag{6.23}$$

and has the units $(kg/m^2 sec)/m$.

Substituting $D^2 = D_0^2 - k_{evap}t$ and simplifying, the evaporation term in the energy integral takes on the form:

$$\int_0^\infty 2\pi(a+y)\dot{q}_e \Delta x dy = -\int_0^\infty \frac{\pi^2 h_{fg} n_0 \rho_w y(a+y)}{2\delta} \left(A_1 T(y)^2 + B_1 T(y) + C_1\right)\left[D_0^2 - \frac{\left(A_1 T(y)^2 + B_1 T(y) + C_1\right)\Delta x}{u(y)}\right]^{\frac{1}{2}} \Delta x dy \tag{6.24}$$

6.3 Justification of Assumptions

Now a model has been developed for the evaporation within the boundary layer, some of the assumptions made to form the model can be checked for validity.

6.3.1 Droplet Entrainment

The acceleration of a drop is based on the drag force exerted by the air flow on the drop. For a spherical drop, the drag force can be evaluated using

$$F_D = -C_D\left(\frac{1}{2}\rho V^2\right)\left(\frac{\pi D^2}{4}\right) \tag{6.25}$$

where the drag coefficient can be estimated [24] from $C_D = 24/Re_D = 24\mu/\rho V D$. Solving

$$F = -3\pi\mu VD = m_{drop}\frac{dV}{dt} = \rho_w\left(\frac{\pi D^3}{6}\right)\frac{dV}{dt} \tag{6.26}$$

for acceleration and integrating from V_0 at $t = 0$ to some final value of V at t yields

$$V = V_0 e^{\frac{-18\mu t}{\rho_w D^2}} = V_0 e^{\frac{-t}{t_{c,acc}}} \tag{6.27}$$

where $t_{c,acc} = \rho_w D^2/18\mu$ is the time constant of droplet acceleration. Since the droplet velocity is an exponential decay, three times $t_{c,acc}$ is enough time for the droplet to achieve 95% of its final velocity. The time constant for drop evaporation can be taken as $t_{c,evap} = D^2/k_{evap}$. The ratio of time constants becomes

$$\frac{3t_{c,acc}}{t_{c,evap}} = \frac{3\rho_w k_{evap}}{18\mu}$$

Near the droplet surface, this ratio will be ~ 1 and on the edge of the boundary layer it will be $\sim .1$. The assumption of fully entrained drops is valid near the outer edge of the boundary layer, but is less accurate close to the fiber surface. This error will cause the evaporation rate to be underestimated. While the drop is being accelerated, the droplet will be subject to a cross flow. This will increase the heat transfer to the drop and the evaporation rate will be higher than calculated. The evaporation rate near the fiber surface[2] is very small due to small cross-sectional area and low droplet density, so the total effect of the error introduced by assuming fully entrained drops will be very small.

6.3.2 Transient Droplet Warm Up

The droplet surface temperature is dependent on the ambient temperature, and will increase as the ambient temperature increases. The time required for a droplet to achieve a steady state temperature can be estimated

[2]This is discussed in length in the results section.

by calculating the convective heat transfer for an average droplet surface temperature. Neglecting the vaporization, the time rate of change of droplet temperature can be calculated by

$$\rho_w C_{p_w} \frac{4\pi}{3}\left(\frac{D}{2}\right)^3 \frac{dT_{drop}}{dt} = 4\pi\left(\frac{D}{2}\right)^2 h_c(T_e - T_{drop}) \tag{6.28}$$

where the convective heat transfer coefficient $h_c = (k/D)Nu$. In the limiting case of $Re \to 0$, $Nu = 2$ for a sphere and

$$\frac{dT_{drop}}{dt} = \frac{12k}{\rho_w C_{p_w} D^2}(T_e - T_{drop}). \tag{6.29}$$

While a time constant can be evaluated for this equation, it is not useful for comparison purposes in this case. The time of interest is the time required for the drop to reach its steady state value where the heat of vaporization is balance by convection. The time constant for equation (6.29) is the time constant for the drop temperature to approach T_e. For a drop in dry air with $T_e = 1000\ K$, the droplet surface temperature evaluated using high mass transfer rate theory is only $340\ K$. For comparison purposes, a rough estimate of the time required for the drop to heat up from an initial temperature[3] of $290\ K$ to the final T_s value of $340\ K$ can be made. For a $70\ \mu m$ diameter drop, equation (6.29) becomes

$$\frac{dT_{drop}}{dt} = (\frac{20.8}{sec})(T_e - T_{drop})$$

which can be evaluated for an average drop temperature of $340 + 290/2 = 315\ K$ to obtain $dT_{drop}/dt = 14248\ K/sec$. The estimated time for the drop to increase from $290\ K$ to $340\ K$ is $t \sim 50\ K/14248\ K/sec = 3.5 * 10^{-3}\ sec$. The droplet life time for a $70\ \mu m$ drop with $T_e = 1000\ K$ is $t = D_0^2/k_{evap} = .057\ sec$. For

[3]Supply water temperature is $\sim 17°C(290\ K)$.

$T_e = 1000\ K$ the droplet life time is an order of magnitude greater than the transient warm up time. The same calculations can be repeated for $T_e = 400\ K$. In this case, the warm up time is .011 *sec* and the droplet life time is .49 *sec*. The assumption of negligible drop warm up time is valid.

6.3.3 Constant Evaporation Coefficient

In the evaluation of the dD/dx term in equation (6.21), k_{evap} was assumed constant over Δx. The full expansion of equation (6.21) is

$$\frac{d}{dx}D = \frac{1}{2}\left(D_0^2 - k_{evap}t\right)^{-\frac{1}{2}}\left(-k_{evap}\frac{dt}{dx} - t\frac{dk_{evap}}{dx}\right). \tag{6.30}$$

Looking at only the last two terms,

$$k_{evap}\frac{dt}{dx} = \frac{k_{evap}}{u} \quad \text{and} \quad t\frac{dk_{evap}}{dx} = \frac{\Delta x}{u}\frac{dk_{evap}}{dx}$$

in order to neglect the $t\ dk_{evap}/dx$ term, it must at least an order of magnitude less than k_{evap}/u. Since k_{evap} is a strong function of temperature, the largest magnitude of dk_{evap}/dx will occur where the value of dT/dx is largest[4], and dk_{evap}/dx can be estimated by $\delta k_{evap}/\delta x$ evaluated over a small distance δx. Looking ahead to the results section and using the data from Fig. 8.1, then

$$\frac{dk_{evap}}{dx} \sim \frac{\delta k_{evap}}{\delta x} = \frac{.8 * 10^{-7} - .5 * 10^{-7}\ m^2/sec}{.1\ m} = 3.0 * 10^{-7}\frac{m^2/sec}{m}$$

over the interval from $x = .1\ m$ to $x = .2\ m$. Since the order of magnitude of k_{evap} is $.1 * 10^{-7}$ to $3 * 10^{-7}$, then as long as the incremental length over which the evaporation rate is evaluated, Δx, is of the order of

[4]The largest temperature gradient in the x direction is on the fiber surface, close to the bushing plate.

magnitude 10^{-2} or less, then $t\ dk_{evap}/dx$ will be at least an order of magnitude less than $k_{evap}\ dt/dx$. The incremental length, Δx, used in the numerical simulation is at the most .001 m, and the assumption that k_{evap} is constant over Δx is valid. Since the assumption is valid for a position on the fiber surface close to the bushing plate where the rate of change of k_{evap} with x is greatest, then the assumption will be valid at all other points in the boundary layer.

6.3.4 Relative Humidity

The assumption of 0 % relative humidity in evaluating droplet evaporation in the boundary layer will cause the evaporation rate to be over estimated. As droplets evaporate, the air in the boundary layer may become saturated with water vapor. Depending on the air temperature, only a certain amount of evaporation can take place before the air becomes fully saturated and evaporative cooling is effectively "shut-down". An estimate of the amount of water required to saturate the air can be made to see if it is reasonable to neglect changes in relative humidity on fiber cooling or to ignore evporative shut down.

The mass flow rate of air in the fiber boundary layer can be found at any point by integrating

$$\dot{m}_{air} = \int_0^{\delta} 2\pi(a+y)\rho \left[U - \frac{U}{\alpha} ln\left(1+\frac{y}{a}\right)\right] dy \tag{6.31}$$

where the value of α can be obtained by solving

$$\alpha = ln\left(\frac{\delta}{a}+1\right)$$

for a given boundary layer thickness δ. An equivalent boundary layer thickness, δ_{equiv} can be defined as the thickness of a uniform sheath of air, moving at the fiber velocity, that yields the same total mass of entrained air as equation (6.31).

$$\dot{m}_{air} = \pi\rho U\left(\delta^2_{equiv} - a^2\right) = \int_0^{\delta} 2\pi(a+y)\rho\left[U - \frac{U}{\alpha}ln\left(1+\frac{y}{a}\right)\right]dy \tag{6.32}$$

In an incremental length of fiber boundary layer (L), the volume of entrained air is

$$Vol_{air} = \pi\left(\delta^2_{equiv} - a^2\right)L. \tag{6.33}$$

The maximum amount of water that can be evaporated into the air can be found be looking at the saturation pressure of water vapor at a given temperature. Assuming a total pressure of 101325 $Pa(1\ Atm)$, the density of water vapor in the air is

$$\rho_{H_2O} = \frac{M_{H_2O}P_{i,H_2O}}{RT} \tag{6.34}$$

where M_{H_2O} is the molecular mass of water vapor, P_{i,H_2O} is the saturation pressure of the water vapor at T, and R is the universal gas constant. The total water mass that can be evaporated is then $m_{H_2O} = \rho_{H_2O}\,Vol_{air}$. If all the energy from the fiber is used to evaporate the spray, then an energy balance can be written as

$$m_{H_2O}h_{fg} = \rho_f C_{p_f}\Delta T_{fiber}\pi\delta^2 L = \rho_f C_{p_f}\Delta T_{fiber}\,Vol_{fiber} \tag{6.35}$$

where h_{fg} is the latent heat of vaporization of water. This procedure can be used to estimate the total energy from the fiber that can be extracted using only evaporation. At 1 m from the bushing plate, the boundary layer is capable of absorbing enough water to cool the fiber by 437 K if the air is at 300 K. This value increases to 1224 K if the air temperature is 320 K and to 4422 K if air temperature is 350 K.

At lower air temperature, these results may be discouraging and seem to indicate that the air will become saturated before the fiber is cooled. The total required temperature change for the fiber is $\sim 1200K$, but the air at lower temperatures can only absorb enough water to cool the fiber by 437 K. In actual operation, evaporation only needs to account for the additional cooling obtained with the spray, not for total cooling of the fiber. Without spray, the fiber will cool due to convection and radiation and a certain temperature profile will be obtained. As will be seen in the results section, the addition of the spray will result in additional cooling of 100 K maximum at 1 m from the bushing plate. This 100 K is certainly less than the 437 K possible by saturating the air. If the air temperature is increased only slightly to 320 K, then 1224 K of cooling is available by evaporative cooling of the air.

Another way to consider this analysis is to look at how much the relative humidity of the air increases to achieve the spray cooling predicted by the model. Assuming that spray cooling is responsible for 100 K of additional fiber temperature drop and the air starts out with 0% relative humidity, then using equation (6.35), the mass of water required to cool the fiber can be calculated. This value can then be converted into a water vapor partial pressure and compared to the saturation pressure. For the 100 K temperature drop and air at 300 K, the relative humidity of the air will increase from 0% to 22.8%. If the air temperature is 320 K, the relative humidity will only increase to 8.2%, and if the air temperature is 350 K, the relative humidity will only increase to 2.2%.

Increasing the relative humidity will slow down the droplet evaporation, which will adversely affect the cooling of the glass fibers, but this analysis shows that evaporation cannot be "shut-down" due to boundary layer saturation, and at higher air temperatures, the relative humidity stays almost constant despite evaporative cooling. The actual boundary layer contains a velocity gradient and crossflow, which will also reduce the effects of increasing relative humidity.

6.3.5 Droplet Contact with Fiber Surface

The assumption of no droplets touching the fiber surface may seem somewhat contrived, especially since direct contact between a droplet and the fiber surface will produce the highest possible cooling rate. The probability of contact between a droplet and fiber surface is small due to a number of factors. The percent

of projected fiber area compared to total cross-sectional area seen by a crossflow is very small. For 10 μm diameter fibers with 1 cm fiber spacing, the total projected fiber area is only .1% of the total area. This reduces the probability of a droplet coming in contact with a fiber.

Each fiber is surrounded by a boundary layer with very steep velocity gradients. The boundary layer will entrain the drops and drag them in the direction of fiber motion, and will act like a buffer layer preventing any drops from coming in contact with the fiber. Also, the fiber surface temperature is greater than the boiling point of water across most of the fiber length, and is much greater than the boiling point of water ($T > 600\ K$) over approximately 1/3 of the fiber length. This will cause rapid evaporation and will shorten the lifetime of any droplets approaching the fiber surface or entrained in the boundary layer. The very short exposure time ($\sim .015\ sec$) of an incremental length of fiber to the spray environment will also reduce the probability of a droplet coming in contact with any one section of fiber.

Some droplets will come in contact with individual fibers and will provide additional cooling on a local basis, but unless the droplet density is very high with large crossflow velocities, evaporative cooling of the boundary layer will remain the primary cooling mechanism and droplet/fiber contact can be neglected. All these arguments become invalid in the short region above the surfactant applicator where the fibers converge into a bundle. Here the high density of spray and fibers, and the lower fiber temperatures will force water onto the fibers and will wet down the bundle, but this region is not the primary area of interest for the cooling of glass fibers and is not considered in this report.

Chapter 7

Numerical Solution for the Fiber Temperature Profile

With all the different possible effects that play a role in the cooling of the glass fibers, the question becomes what needs to be included in a simulation and what can be neglected. As stated earlier, bulk specific heat and evaporation effects can be used to justify the assumption of constant environmental air temperatures. Radiation effects, while estimated to be small, can be easily incorporated into a numerical model and so for completeness are included in all simulations. Obviously, the evaporation within the boundary layer is the last primary effect and should account for the majority of cooling enhancement seen with spray cooling. Solution of the fiber temperature profile for both the no-spray and spray cooled system must be found numerically. MAPLE V Release 4 was chosen to find the numerical solution because of its powerful tools for handling differential equations and numerical integration. In both the no-spray analysis and the spray-cooled analysis, the solution is based on incremental values of α. This chapter covers the numerical solution used to solve the equations for fiber temperature developed in the previous chapters. The first section covers the approach used to solve for the velocity boundary layer and heat transfer from a fiber with no spray present. The second section covers the method for solving the fiber temperature with spray cooling, and the final section discusses the computer program used to run fiber simulations.

7.1 No-Spray Solution

With initial system parameters such as fiber diameter, drawing speed, initial fiber temperature and environmental temperature, values of β are found for α values of .02 to .08 by .02 increments, using the series expansion (eqn. 4.39). Once these initial values are found, equation (5.15) is forward integrated using a Fehlberg fourth-fifth order Runge-Kutta method. For each value of α, the corresponding β and x values are found. The temperature profile of the fiber can be found by computing the temperature drop of the fiber from one position x to the next incremental position $x + \Delta x$. Based on the assumption that β and Θ_f are constant, the temperature change of the fiber due to convection is

$$\Delta T_{conv} = \frac{-2\pi ak\frac{\partial T}{\partial y}|_{y=0}\Delta x}{\pi a^2 \rho_f C_{p_f} U_f} = \frac{-2k\Theta_f}{a^2\beta\rho_f C_{p_f} U_f}\Delta x \tag{7.1}$$

over the increment Δx. The temperature change due to radiation to the environment over the small increment is independent of the convective term and can be found using

$$\Delta T_{rad} = \frac{-2\epsilon\sigma_r(T_f^4 - T_{env}^4)}{a\rho_f C_{p_f} U_f}\Delta x \tag{7.2}$$

where radiative transfer from the bushing plate to the fibers is assumed negligible (Section 5.3) and the view factor from the fiber to the environment is 1. The total temperature drop over Δx is simply $\Delta T_{\Delta x} = \Delta T_{rad} + \Delta T_{conv}$, and $T_{x+\Delta x} = T_x + \Delta T_{\Delta x}$. By incrementing α from 0 to some final value α', the fiber temperature profile along the length of the fiber can be found. The final α value depends on fiber parameters and the length of interest for the temperature profile. As a general rule, a maximum α value of 7 will be sufficient for all applications.

A note needs to be made at this point about the effect of variable properties on the numerical simulation. Due to the large temperature range (300 K - 1500 K) of the system, a procedure is needed to account for variable physical properties of the air. All fiber properties are assumed constant with temperature with

values[1] of $\rho_f = 2562\ kg/m^3$, $C_{p_f} = 1519\ J/kg$, and $\epsilon = 0.3$. Air properties need to be evaluated at an average local boundary layer film temperature for an incremental length Δx. At any point x, the average film temperature

$$T_{film} = T_{env} + \frac{T_f - T_{env}}{2} \tag{7.3}$$

is evaluated. This value is then used to evaluate air density, specific heat, and kinematic viscosity based on polynomial curve fits to tabulated data. The thermal conductivity is evaluated at the fiber surface temperature using a polynomial fit. These values are then used in the evaluation of β and $\Delta T_{\Delta x}$.

7.2 Spray-Cooled Solution

The differential equation for β in the spray cooled case, after expanding the evaporation term, becomes

$$\begin{aligned}\frac{d\beta}{d\alpha} = \frac{2\beta}{\alpha\ Pr} + \frac{\eta}{\alpha^2\ Pr}\left(e^{2\alpha} - \alpha e^{2\alpha} + \beta e^2\alpha - 2\alpha\beta - \alpha - 1 - \beta\right) \\ - \frac{\beta}{\alpha}\frac{\left(2\alpha e^{2\alpha} - 2\alpha^2 e^{2\alpha} + 2\alpha\beta e^{2\alpha} - e^{2\alpha} - \beta e^{2\alpha} + 1 + \beta\right)}{\left(-e^{2\alpha} + \alpha e^{2\alpha} + \alpha + 1\right)} \\ + \frac{2\beta^2}{\Theta_f \alpha k\ Pr}\int_0^{\delta_T} \frac{-\pi h_{fg} n_0 \rho_w y(a+y)}{4\delta}\left(A_1 T(y)^2 + B_1 T(y) + C_1\right) \\ \left[D_0^2 - \frac{\left(A_1 T(y)^2 1 + B_1 T(y) + C_1\right)\Delta x}{u(y)}\right]^{\frac{1}{2}} dy\end{aligned} \tag{7.4}$$

where $\delta_T = a(e^\beta - 1)$ is the thermal boundary layer thickness and $\alpha \leq \beta$. The differential equation for β when $\beta \leq \alpha$ can be similarly expanded. Again, a Fehlberg fourth-fifth order Runge-Kutta method can be used to forward integrate these equations, but a problem arises in the evaluation of the evaporation term. The evaporation integral does not have a closed form solution and must be evaluated numerically. This causes a problem due to the presence of the Δx term. Equation (7.4) is based on an integration from α_i to α_{i+1}, but the evaporation integral is based over an incremental fiber length Δx. In order to get around this

[1] Data provided by PPG Industries Inc.

problem, the fiber position for α_i and α_{i+1} are solved. The two resulting x values are subtracted to find Δx which is then used to evaluate the evaporation integral.

The evaporation integral is evaluated using an adaptive Newton-Cotes method. This method permits specification of accuracy and can be modified to handle singularities without excessive computational loading of the computer system. The procedure for solving for the fiber temperature profile is very similar to the no-spray solution. The simulation is set up to allow for spray insertion at any point x along the fiber. Before spray contact with the boundary layer, the no-spray solution is used to solve for the temperature profile. At the initial point of contact with the spray, the β value from the no-spray solution is used to determine the temperature profile. This profile is assumed constant over the small interval from α_i to α_{i+1}. This profile along with the corresponding x values are used to evaluate the evaporation integral. This numerical result is substituted back into the β differential equation which is then forward integrated to find β_{i+1}. With this value of β, the change in fiber temperature over Δx can again be found using equation (7.1). This value is then used as input to evaluate the evaporation term over the next interval. At each point, the α and β values are compared to determine which differential form for β should be used. This procedure is followed over the length of the fiber to solve for the fiber temperature profile. Variable property effects are handled in the same way as for the no-spray analysis. The droplet diameter at the beginning of any interval Δx is assumed uniform and equal to a preset representative diameter. As stated before in the development of the evaporation model, relative humidity of the air in the boundary layer is assumed constant at zero.

For all fibers considered, α values vary from zero at the beginning of the fiber to values around 7 for fiber lengths of $2-3\ m$. The β values for the no-spray solution remain of the same order of magnitude as α, but with spray cooling the maximum value of β depends on the contact point of the spray with the boundary layer. From the contact point down, the β values of the spray cooled fibers decrease with increasing α and can be an order of magnitude less than α. There is no simple relationship between α and fiber position x due to the complex mathematical relation involving exponentials and the exponential integral function,

$$\frac{2\nu x}{Ua^2} = \frac{e^{2\alpha}-1}{\alpha} + Ei(2\alpha) + ln(2\alpha) + \gamma - 2$$

but x roughly varies with the exponential of α.

7.3 MAPLE V Code

Several points need to be made on the use of MAPLE V to solve for the temperature profiles. The program code is computationally fairly expensive. For a full simulation over 2 meters of fiber length, a P-5 133 MHz computer takes about 45 minutes to complete the calculations. The large part of this computational time is for the numerical integration of the evaporation term. It was for this reason that a Newton-Cotes method was chosen for the integration. Other choices were available including a Curtis-Clenshaw quadrature method with algorithms for handling singularities, but these methods were much more computationally expensive with run times approaching several hours.

The presence of the Δx term in the evaporation integral puts a restriction on the incremental step for α. The Δx term is determined by comparing fiber positions of two consecutive α values. If $(k\Delta x/u) > D_0^2$, then the square root term in the evaporation integral evaluates to an imaginary value and the software cannot evaluate the differential equation. To avoid this problem, the α increment must be kept small to keep Δx small. This results in a large iteration loop used to evaluate the fiber temperature profile and longer program run times.

The evaluation of the evaporation integral is not only the largest computational form in the simulation, it is also the most unstable and least robust. Changing initial system parameters such as spray density or droplet size will often cause a failure in the numerical integration. When this happens, resetting the system and starting the simulation from scratch will often fix the problem. If this does not work, the code calling the numerical integration needs to be modified. In the command line of the spray cooling iteration that states:

$$evapt := \text{evalf}(Int(total, y = 0..(delta), 4,\ NCrule));$$

the digits control can be modified. If the iteration is not working, try decreasing the number 4 one digit

at a time. As a general rule, a value of 2-3 will run most simulations, but in some instances it needs to be reduced to 1. This will cause the integration to be evaluated with a larger error range, but will prevent the system from crashing.

Another note is the placement of the declaration of the differential equation for β. MAPLE V solves differential equations from the initial conditions stated in the equation definition only for the first point evaluated. After this, MAPLE V will evaluate the differential equation from the last calculated point. If β is defined with initial conditions at α_0, then when β is evaluated for the first time, the differential equation solver will start from the initial conditions. The next time the differential equation is called, the program will solve the equation from the last mesh point, not from the initial conditions. Unless the differential equation is unassigned and re-declared, the computer will used the initial values only once. This works fine for the no-spray solution and the differential form of β can be declared outside the iteration loop. For the spray cooled case however, the differential form must be declared within the iteration loop. As the thermal and velocity boundary layers change size, the differential equation changes form and must be redeclared. This causes some additional computation time, but it is small compared to the total computational time.

Chapter 8

Results

This chapter presents and discusses the results from the fiber simulations. It also covers the problem of model validation and sources of errors in the model.

8.1 Model Results

The simulation has been run over a wide range of configurations, but for comparison purposes a baseline was chosen. Baseline conditions are for a 10 μm diameter fiber being drawn at 60 m/sec through still air at 320 K. The initial fiber temperature is 1500 K with a droplet density of 5000 $drops/cm^3$ and a representative Sauter Mean Diameter of 70 μm. The spray was inserted into the fiber boundary layer at $x = 1.8\ cm$ (corresponds to $\alpha = 5.0$). The baseline results for the no-spray and spray-cooled temperature profile are plotted in Fig.8.1. At a fiber position of 1 m the temperature difference between the spray cooled and no spray case is about 90 $K(163°F)$. The fiber temperature at this point for the spray cooled case is 360 K, and 450 K for no-spray cooling.

Before proceeding with more results, a comparison needs to be made between fiber temperature profiles based on evaporation coefficients evaluated using low and high mass transfer rate theory. Fig. 8.2 shows the fiber temperature profiles evaluated under baseline fiber/spray conditions for both high and low mass transfer rate theory. As can be seen, there is no difference between the spray cooled temperature profiles.

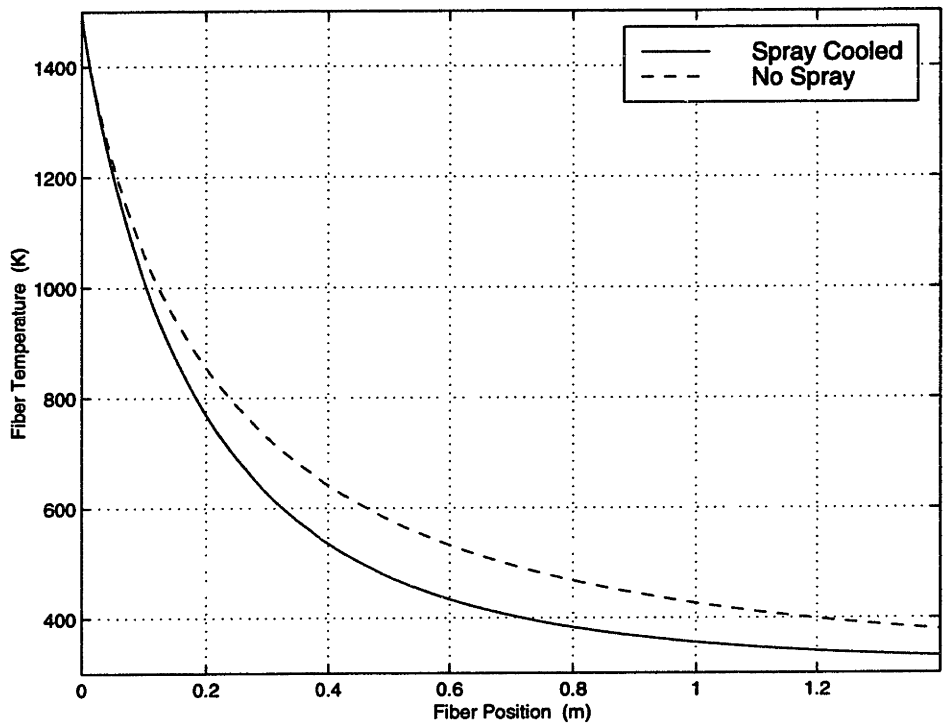

Figure 8.1: Baseline temperature profile for 10 μm fiber at 60 m/sec.

This may not seem to make sense, as the evaporation coefficients from the two theories vary significantly at high temperatures. The evaporation rate is strong function of air temperature, but the total evaporation over an incremental length of boundary layer is the primary point of interest. In the region of the boundary layer where the temperatures are very high, the total area is very small (i.e. proportional to $(y+a)^2$). The majority of the boundary layer volume is in the region where the temperatures are lower[1]. For these temperature ranges, the evaporation coefficients for the high and low mass rate theories are the same. This actually demonstrates a useful point, the majority of the evaporative cooling takes place around the outer edge of the boundary layer, and the evaporation right next to the fiber is very small due to the small cross-sectional area and low droplet density[2].

Simulations were run for different parameter values, and plotted against the baseline results. In Fig. 8.3 the droplet density was varied from 0 to 10000 $drops/cm^3$. As the droplet density was decreased, the

[1] $T(x,y) \sim 400 - 500\ K$

[2] Recall that the droplet density approaches zero as radial position approaches the fiber surface.

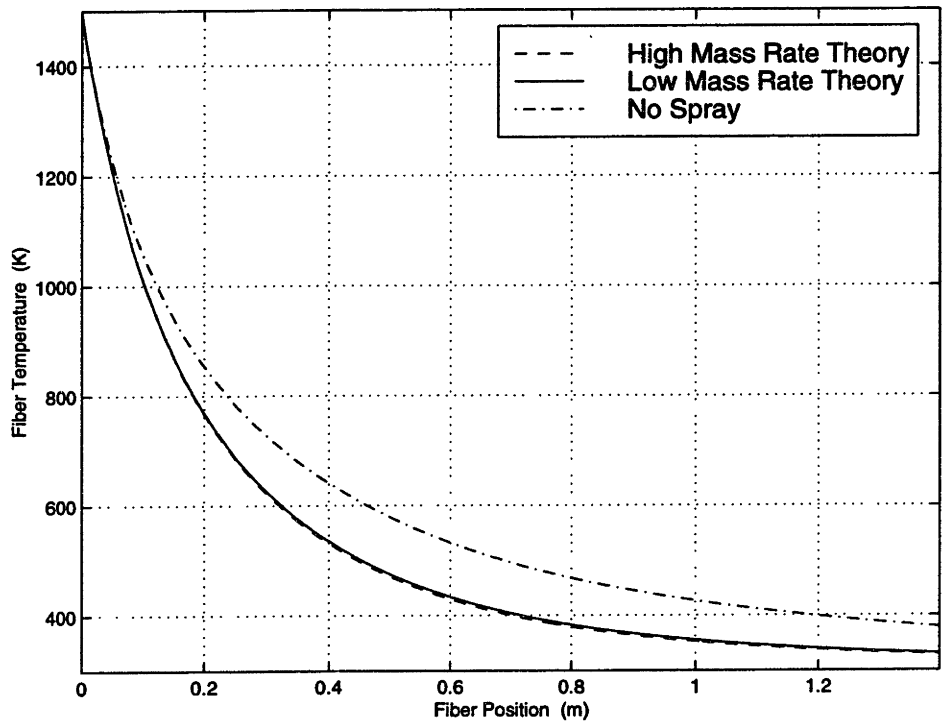

Figure 8.2: Fiber temperature profiles for baseline conditions evaluated using high and low mass transfer rate theory.

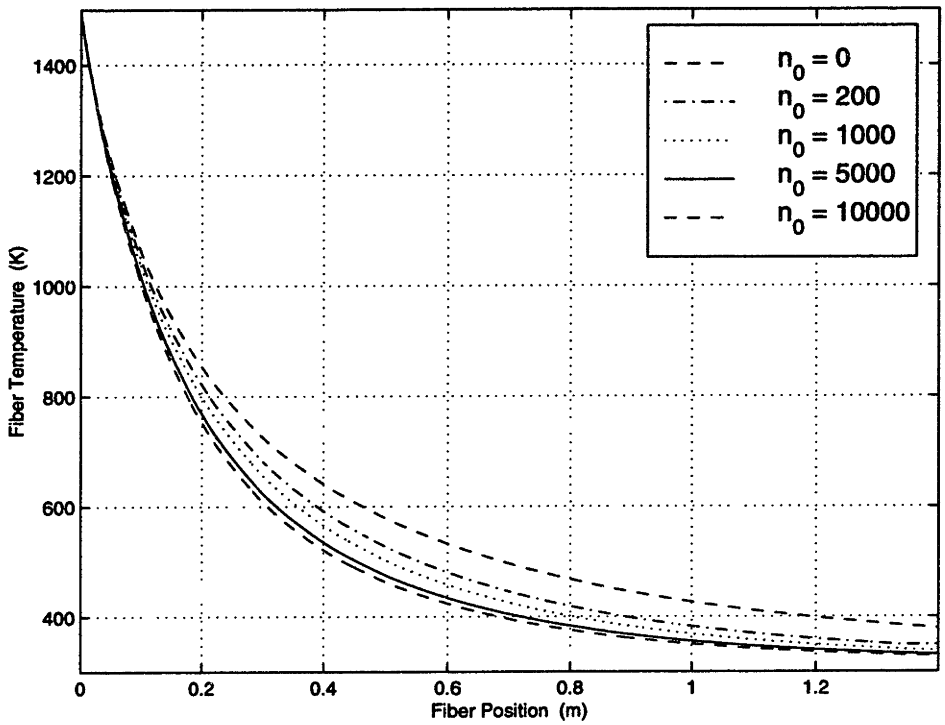

Figure 8.3: Fiber temperature profiles for multiple droplet densities ($drops/cm^3$) with $SMD = 70\ \mu m$.

temperature profile approaches the no spray profile. The largest variation in temperature profile is seen between .2 and .8 m from the bushing plate. After .8 m the spray cooled profiles start to converge and become more uniform despite different spray densities. Spray cooling is a cumulative effect along the fiber, and final temperatures at fiber positions greater than 1 m are fairly independent of spray density. For high values of spray densities, changing the density has almost no effect on the temperature profile anywhere along the fiber. This can be seen easily in Fig. 8.3 for spray densities of 5000 $drops/cm^3$ and 10000 $drops/cm^3$. At no point is the difference in these temperature profiles more than 10 K. To put the droplet density in perspective, a droplet density of 5000 $drops/cm^3$ with Sauter mean diameter of 70 μm is equivalent to have .89 cc of water dispersed in 1000 cc of air.

Fig. 8.4 shows the variation of temperature profile for changes in drop size. For the same droplet density, as drop size increases the surface area available for evaporation becomes larger and the cooling rate should increase. As can be seen, increasing the droplet size while holding the droplet density constant has only a very small effect on the fiber temperature profile. Droplet size is normally tied to droplet density

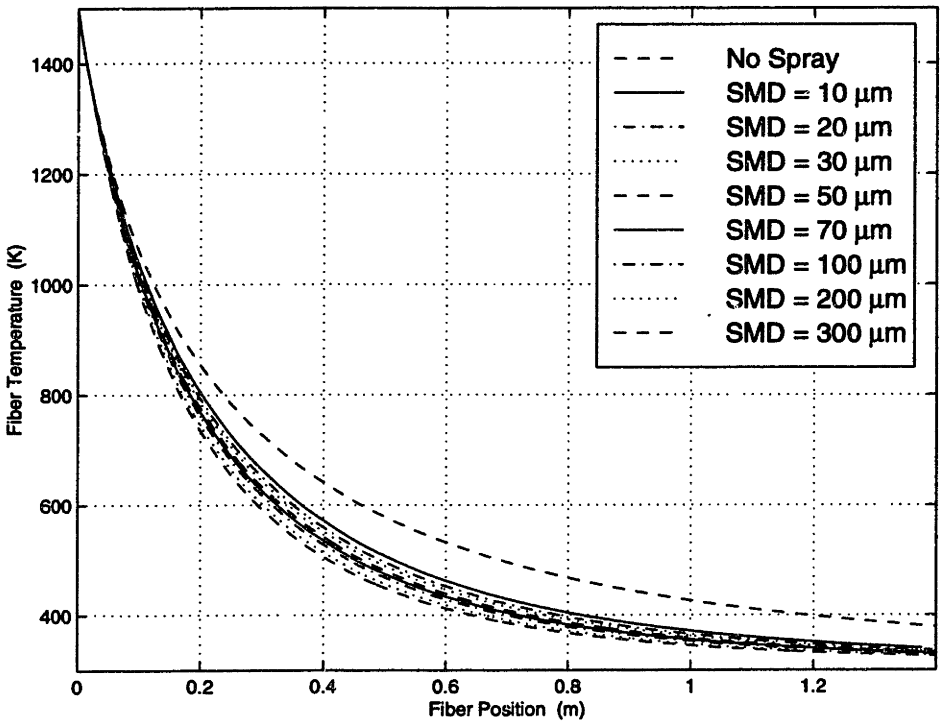

Figure 8.4: Temperature profiles for multiple droplet sizes with droplet density $n_0 = 5000\ drops/cm^3$.

and typically increasing evaporation rate is achieved by atomizing the same amount of water with finer atomization (smaller drop size) which leads to higher drop density. While each individual drop may have a smaller surface area, the increased droplet density to achieve the same amount of total water spray will result in higher overall surface area and a higher evaporation rate. Higher drop density with smaller drops will achieve better cooling than larger drops with lower density for the same water flow rate. Fig. 8.5 shows the variation of temperature profile for varying spray conditions that all have the same total spray volume. As the Sauter mean diameter is decreased, the spray density in increased to keep the ratio of water volume to total air volume constant. As can be seen, the smaller the SMD, the more cooling for the same amount of water.

Despite bulk specific heat and evaporation effects, ambient temperatures will not be constant over the fiber bundles. Fig. 8.6 has the temperature profiles for a 10 μm fiber at 60 m/sec with varying environmental temperatures. There is very little difference in the profiles over the first 20 cm of fiber length despite a 100 K difference in air temperature. Beyond this, the profiles start to diverge as each approaches its steady state

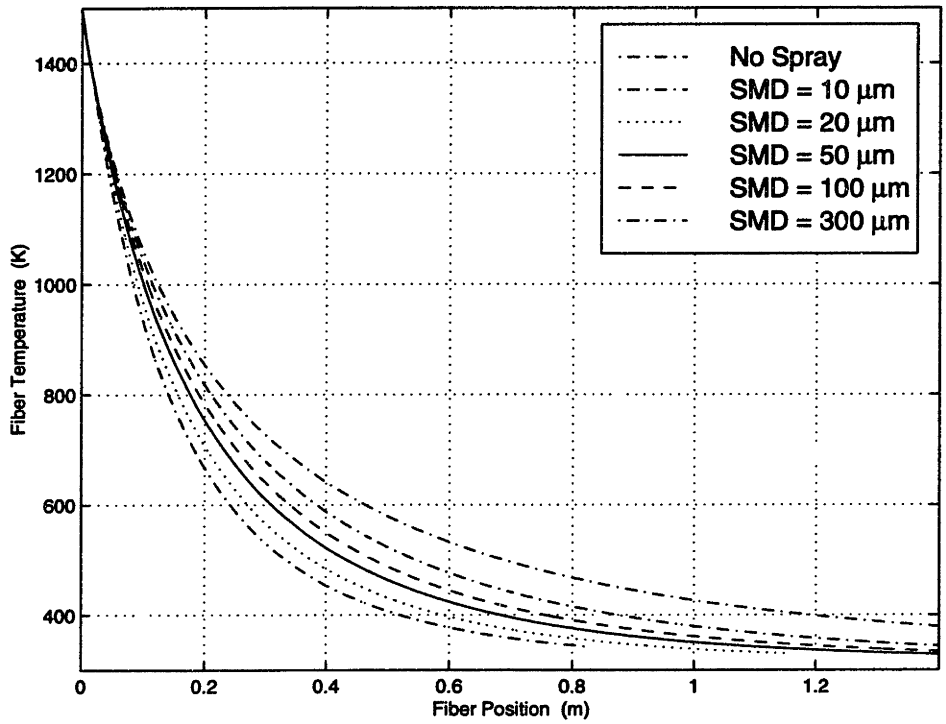

Figure 8.5: Temperature profiles for constant volume of sprayed liquid ($8.98 * 10^{-4}\ m^3\ water/m^3\ air$).

value. Higher air temperatures up near the bushing plate have no effect on the cooling rate of the glass fibers over the initial drawing length . Blowing cool air up towards the bushing plate will not improve the cooling of the fiber, unless it is through increasing the crossflow velocity, and will simply increase the power consumption of the system due to higher convective heat transfer from the bushing plate.

Initial fiber temperature will effect the fiber temperature profile, but Fig. 8.7 shows that for spray cooling of a 10 μm fiber at 60 m/sec, initial fiber temperature has no effect on fiber temperature past .8 m. The evaporation within the boundary layer is a strong function of temperature. As the temperature is increased, the evaporation will increase accordingly, resulting in faster cooling of the fiber until the temperature approaches the steady state value.

Where the spray initially contacts the boundary layer will have an effect on the temperature profile. Fig. 8.8 has the fiber temperature profiles for spray contact points between 1.8 cm from the bushing plate to 71 cm from the bushing plate. The figure shows that beyond 90 cm from the bushing plate, it makes very little difference where the spray contacts the fiber boundary layer. This is useful in that it demonstrates

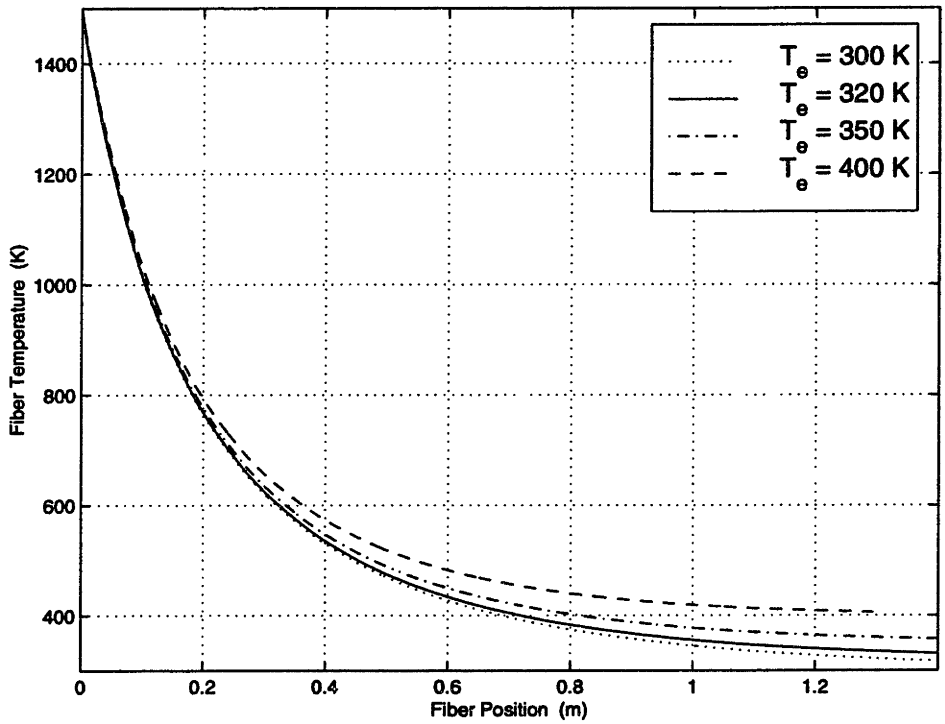

Figure 8.6: Fiber temperature profiles for varying bulk air temperatures.

that final fiber temperature is not sensitive to spray distribution in the vertical direction. If the objective is to simply cool the fiber by the point where the surfactant is applied, then getting spray into the fiber bundle and around each fiber is more important than making sure the spray contacts each fiber at the same x position. If the physical properties of the fiber require a certain cooling rate between two temperatures, then vertical placement of the spray may become critical[3]. For no spray cooling, the thermal boundary layer is always larger than the velocity boundary layer and grows at a much faster rate. At 20 cm the velocity boundary layer is 2 mm thick, but the thermal boundary layer is already 4.2 mm thick. When spray is added to the boundary layer, the thermal boundary thickness is reduced. How much the thermal boundary layer is reduced depends on the amount of evaporation in the boundary layer. The evaporation rate is dependent on the temperature profile, but also on the volume of the boundary layer. When the spray contacts the boundary layer further from the bushing plate, the volume of the boundary layer is much larger and this

[3]If quenching of the fiber must occur before the fiber temperature is reduced below some critical value, where the spray comes in contact with the spray is important.

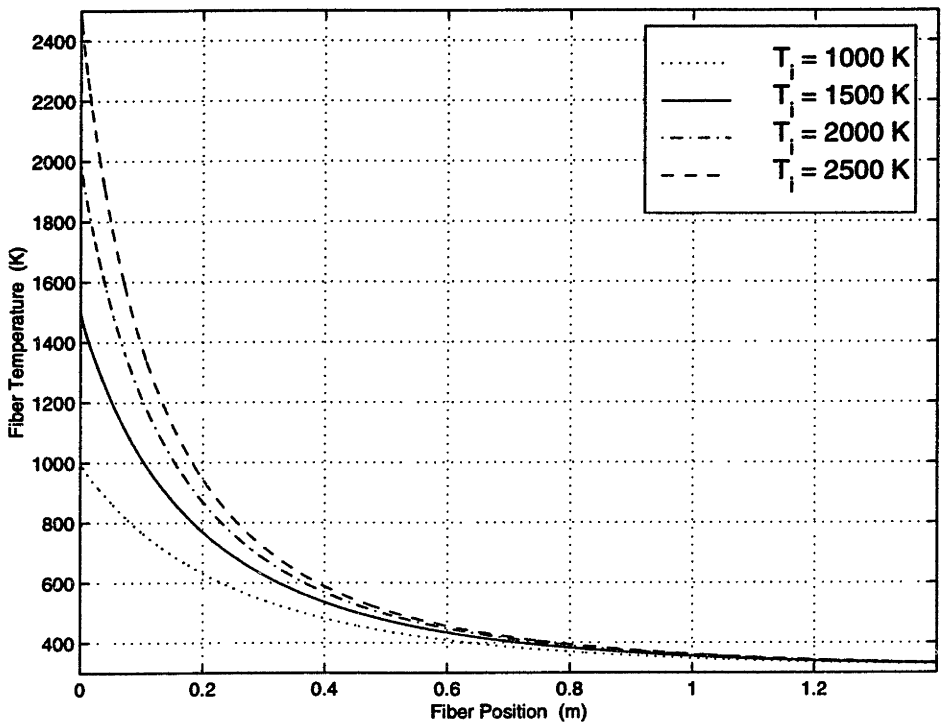

Figure 8.7: Fiber temperature profiles for varying initial fiber temperatures.

overcomes the decrease in temperature. The evaporation rate is initially much larger and this results in a large initial decrease in fiber temperature. This situation does not fully represent what physically actually happens upon spray contact with the boundary layer. The spray cooling model is based on the assumption that as soon as the spray contacts the boundary layer, the spray is distributed across the entire boundary layer. In reality, the spray will take a certain distance to become distributed into the boundary layer and this will increase the distance it takes to shrink the thermal boundary layer shown in Fig. 8.9. Fig. 8.10 shows the evaporation rate as a function of distance for the baseline fiber configuration. Upon initial contact with the spray, the evaporation rate reaches a maximum and then decreases and approaches zero. Again, this in not exactly physically what happens as the spray will take a certain distance to become distributed in the boundary layer.

Another interesting point that can be studied is how to cool the fibers to the required level, but still have dry fibers by the time the surfactant is introduced. To do this, a dry air crossflow can be introduced into the fiber bundle. This will help evaporate any drops left in the boundary layer and prevent any from

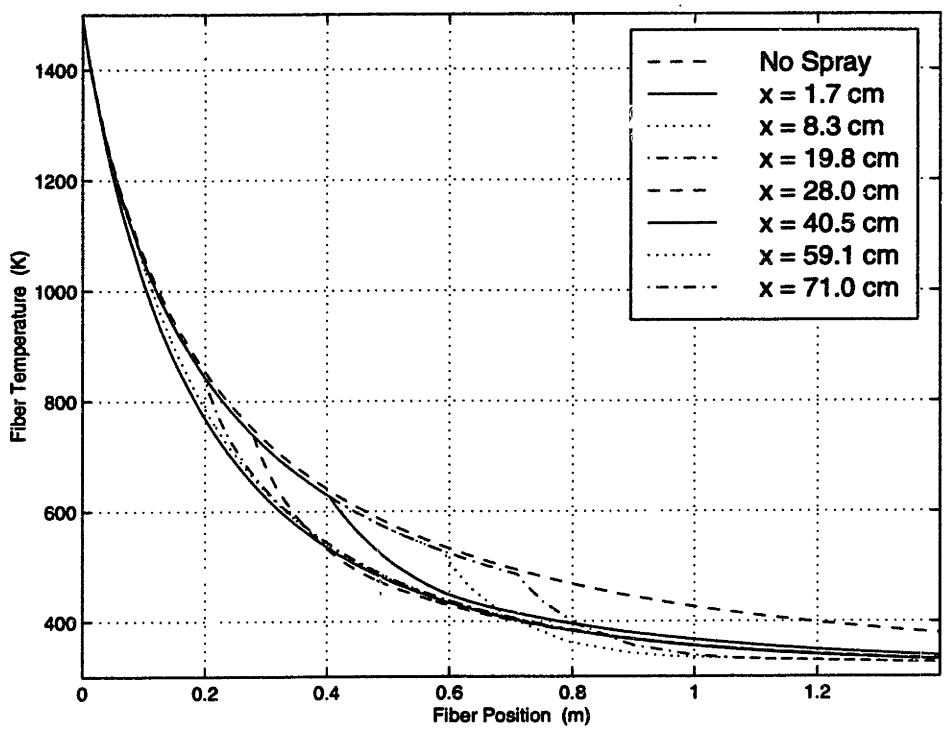

Figure 8.8: Fiber temperature profiles for varying spray contact points.

contacting and sticking to the fiber surface once the fiber temperature is reduced below the boiling point of water. The crossflow needs to be placed such that sufficient cooling of the fiber is already achieved before the spray is removed. Fig. 8.11 shows the fiber temperature profile for a 10 μm fiber at 60 m/sec over a fiber position of .4 to 1.4 m. The spray is removed from the fiber at $x = .6$ m and $x = .8$ m. This has some effect on the fiber temperature at 1 m. For the spray being removed at .6 m, the fiber temperature is 380 K. If the spray is removed at .8 m, the fiber temperature at 1 m is 370 K. This compares to a temperature of 360 K if the spray is left in the boundary layer. These temperatures actually represent worst cases, as when the cross flow is introduced into the fiber bundle, the effective convective heat transfer coefficient will be increased due to the thermal boundary layer being thinner around each fiber. This will increase the cooling of the fiber, and the profiles should not vary much over the case with continued spray cooling.

The effect of spray cooling will vary with the fiber size and drawing speed. Fig. 8.12 shows the fiber temperature profile for a 10 μm fiber being drawn at 30 m/sec. Spray conditions in this case are the same as the baseline, with a spray density of 5000 $drops/m^3$ and a SMD of 70 μm. Compared to the 10 μm

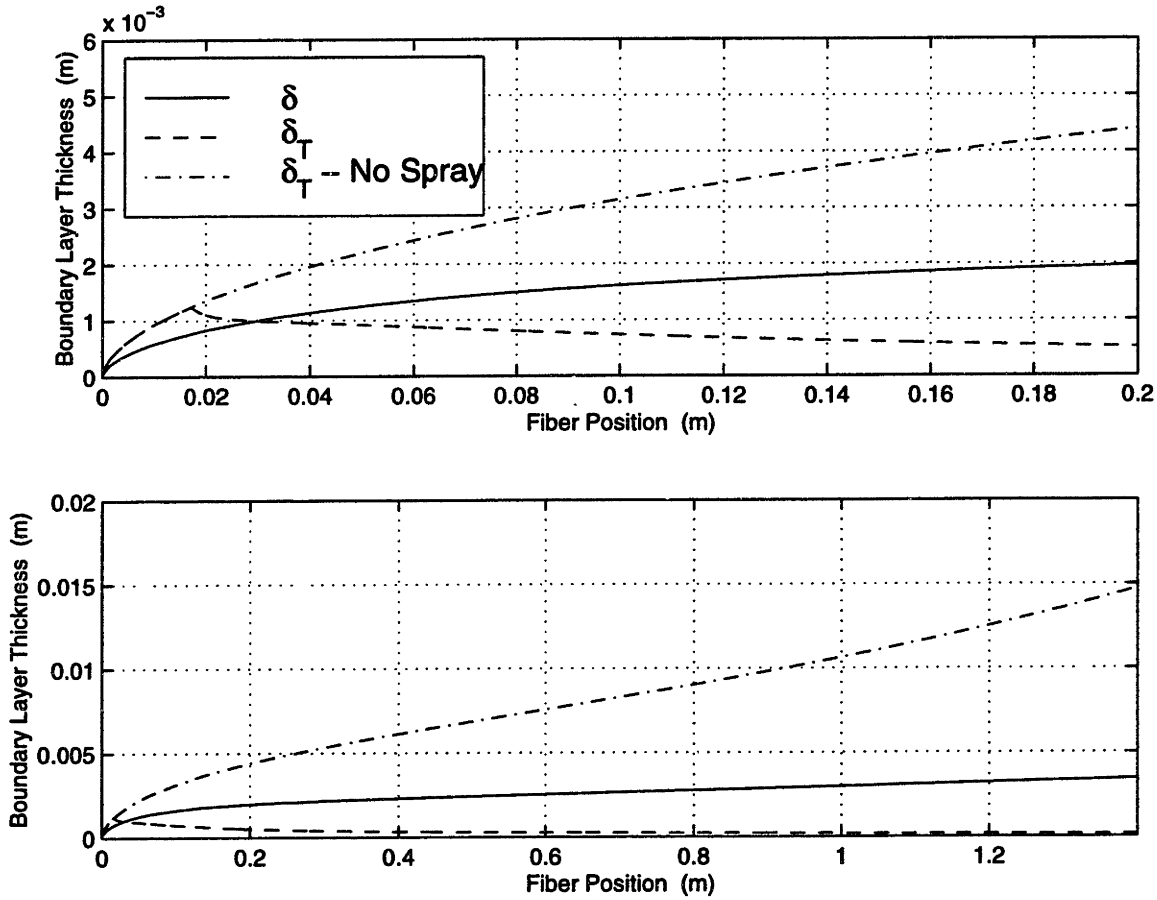

Figure 8.9: Velocity and thermal boundary layer thickness for 10 μm fiber at 60 m/sec.

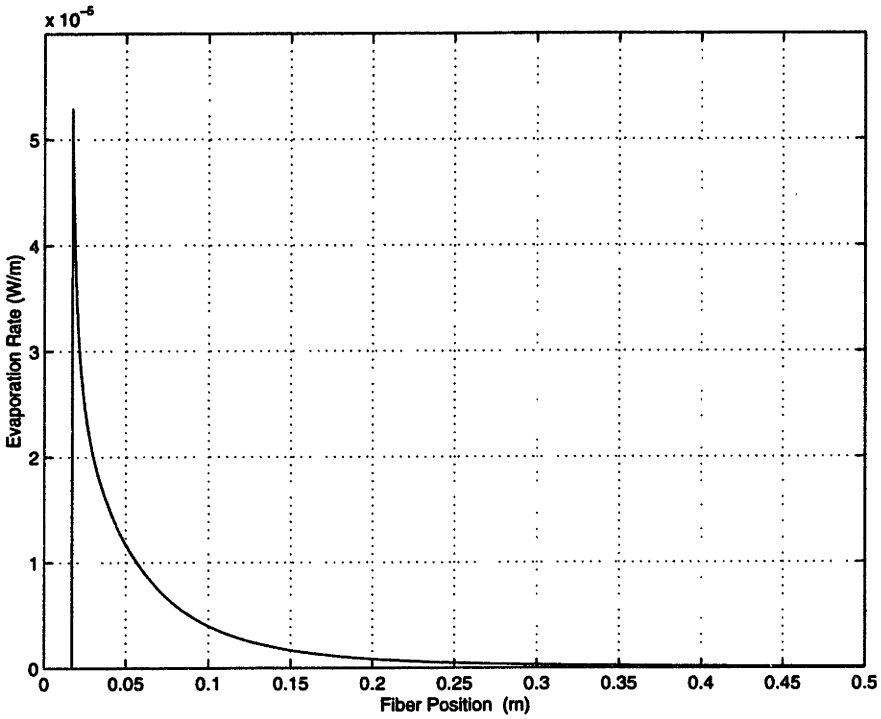

Figure 8.10: Evaporation rate for baseline fiber configuration.

fiber at 60 m/sec, the fiber temperature is reduced more over the same length of fiber. Recalling that the temperature change of the fiber is

$$\Delta T_{\Delta x} = \frac{-2k\Theta_f}{\beta a^2 \rho_f C_{p_f} U_f} \Delta x$$

for a small incremental length Δx. As the fiber velocity decreases, the temperature change over the same incremental length is increased. This can be seen in Fig. 8.12 where the fiber temperature is 380 K at 1 m for the no-spray case at 30 m/sec vs. 440 K for the baseline fiber moving at 60 m/sec. The opposite effect should be seen for a fiber moving faster than the baseline condition. Fig. 8.13 shows the fiber temperature profile for 10 μm fiber moving at 90 m/sec. As expected the fiber temperature at 1 m is higher with a value of 510 K for no spray cooling. The fiber velocity also affects the spray-cooled temperature profile. At 30 m/sec, spray cooling has reduced the fiber temperature to 320 K, but at 90 m/sec the temperature is

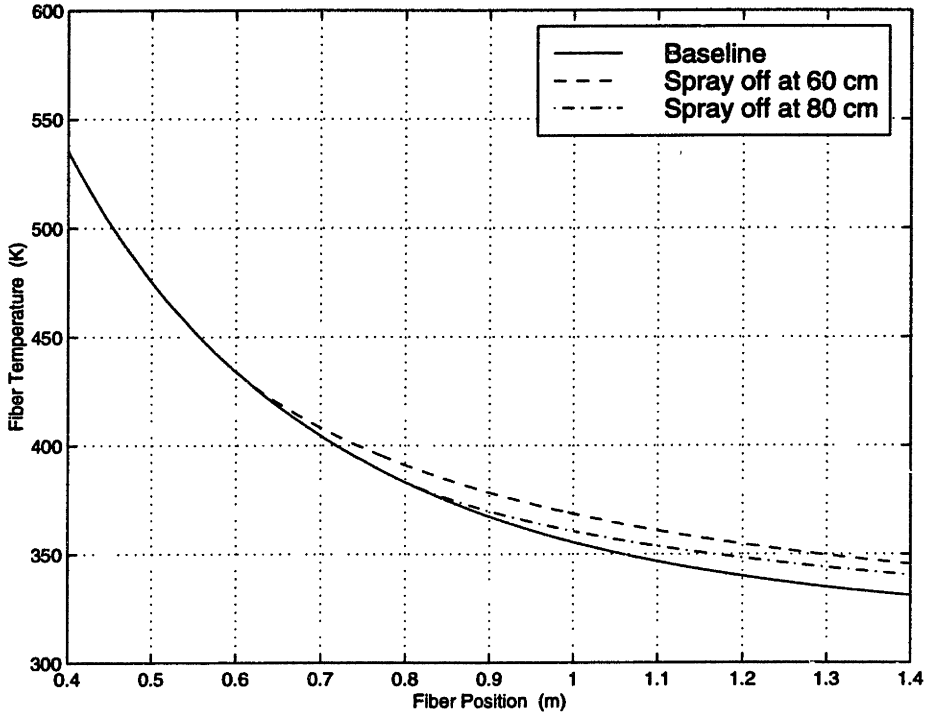

Figure 8.11: Fiber temperature profiles for spray being removed from the boundary layer.

only reduced to 400 K.

Fig. 8.14 shows the fiber temperature profile for a 25 μm fiber being drawn at 10 m/sec. Spray cooling reduces the temperature at 1 m from 490 K to 370 K. Fig. 8.15 shows the temperature profile for a 5 μm fiber being drawn at 50 m/sec. Spray cooling has much less of an effect on this small fiber. With no spray cooling, the fiber has already cooled to the steady state value long before reaching 1 m. By .5 m, the fiber temperature is 320 K with spray cooling and 370 K without.

8.2 Sources of Error and Model Validation

8.2.1 Sources of Error

In the development of the spray cooling model, a number of assumptions were made that will cause errors in the results. Some of these effects will tend to overestimate the temperature of the fibers, some will tend to underestimate the temperature of the fibers. One of the primary sources of error in the model

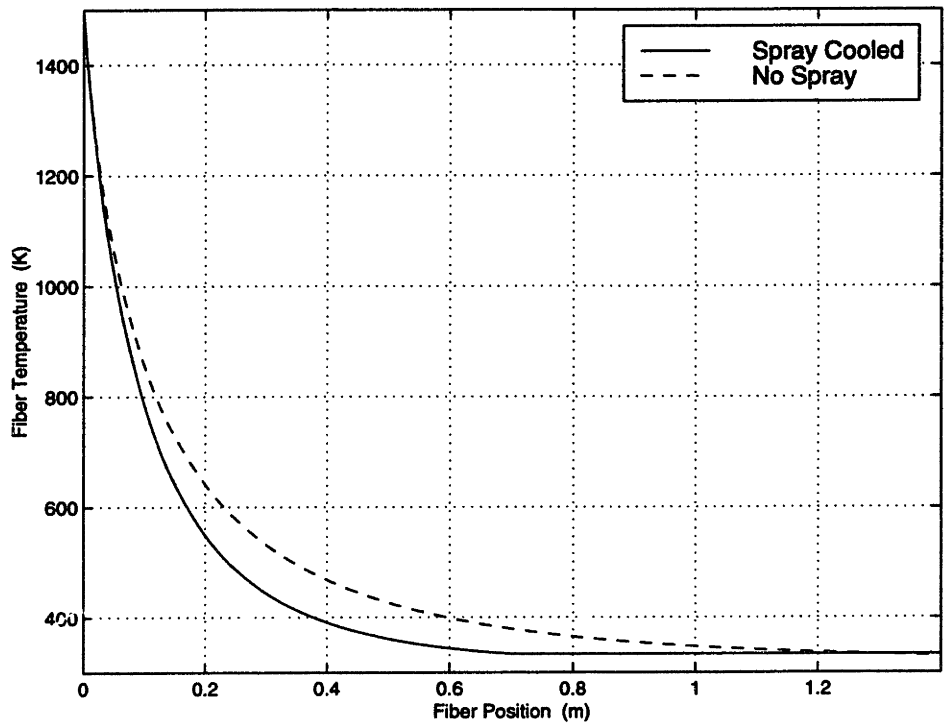

Figure 8.12: Fiber temperature profile for 10 μm fiber at 30 m/sec.

is from neglecting the crossflow in the fiber bundles. The cross-flowing air will increase the heat transfer by decreasing the thickness of the thermal boundary layer and by increasing the drop density within the boundary layer. If the crossflow is sufficiently large, it will effectively strip off the boundary layer, reducing the thermal thickness to a very thin film. As the fibers converge near the surfactant applicator, the air within the bundle will be forced out, creating a crossflow that will increase the heat transfer rate. Unfortunately, the velocity fields for crossflow and induced flow from fiber motion are not vector quantities that can be simply added together. A full momentum analysis of the boundary layer would be required to describe the flow field around the fiber. From this, the evaporation information could be incorporated to account for spray cooling and the fiber temperature profile could be calculated.

Another source of error in the heat transfer model comes from use of the integral method. The Karman-Pohlhausen method assumes a temperature and velocity profile, and then fits this solution to the boundary conditions. This introduces an error into the model that depends on how well the assumed profiles match the actual physical system. Bourne and Elliston [11] estimated correction factors for the logarithmic profiles

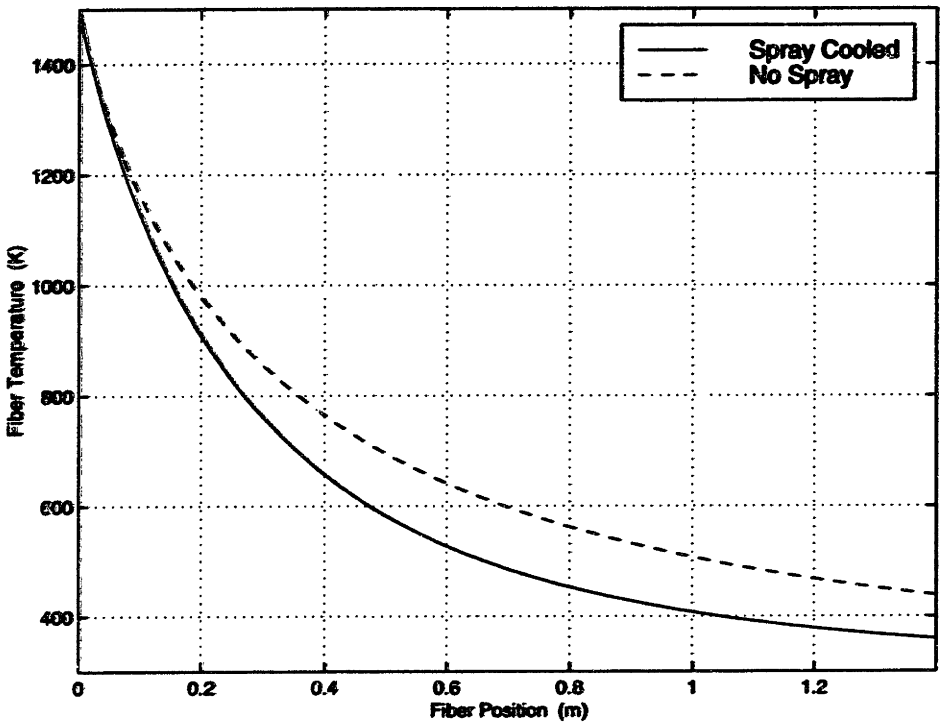

Figure 8.13: Fiber temperature profile for 10 μm fiber at 90 m/sec.

for the no spray solution. For small values of $\nu x/Ua^2$, β is over estimated by 8%, and for large values of $\nu x/Ua^2$, β is over estimated by 2%. This results in the heat transfer from the fiber being underestimated. These correction factors have not been applied to the calculated values from the simulation. Rather, the results from a full finite element analysis of the moving fibers (currently being done at Los Alomos) can be used to correct the simulation values in the no spray case. These corrections will also be input into the spray cooled simulation.

The evaporation rate of the drops will also be underestimated. The calculations were for fully entrained drops in still air. In the boundary layer, the droplets are actually in a velocity gradient, so the drops will tend to be stretched and deformed. This will increase the droplet surface area which will increase the evaporation rate.

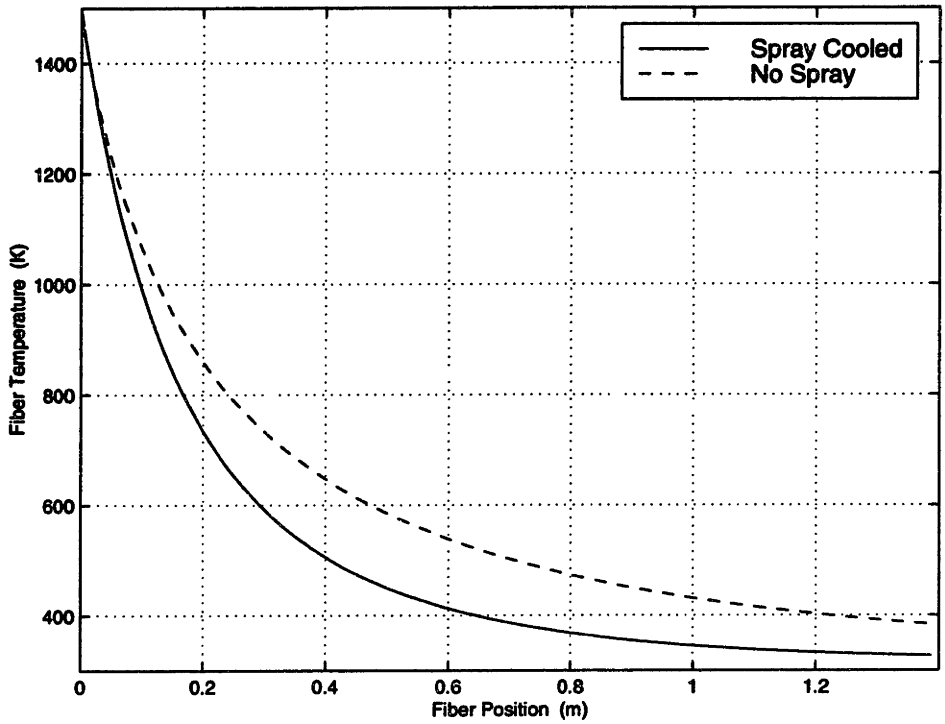

Figure 8.14: Fiber temperature profile for 25 μm fiber at 10 m/sec.

8.2.2 Model Validation

The question arises of how to check the model for validity. The no-spray analysis can be checked by comparison to experimental results and by comparison to a full finite element analysis of the boundary layer. This data can be used to correct the no-spray solution for errors inherent in the Karman-Pohlhausen technique and for errors introduced in the treatment of variable properties. Corrections to the velocity boundary layer can be used directly in the spray-cooling analysis. Results from a suitable finite element analysis and from experimental data can also be used to correct for crossflow effects. Checking the validity of the spray cooling model is much harder. There is at present no easy way to directly measure the temperature profile of a fiber in dry air, and the presence of the spray will only complicate matters. The only means of checking the model is to compare the results from actual fiber runs to those predicted by the theory.

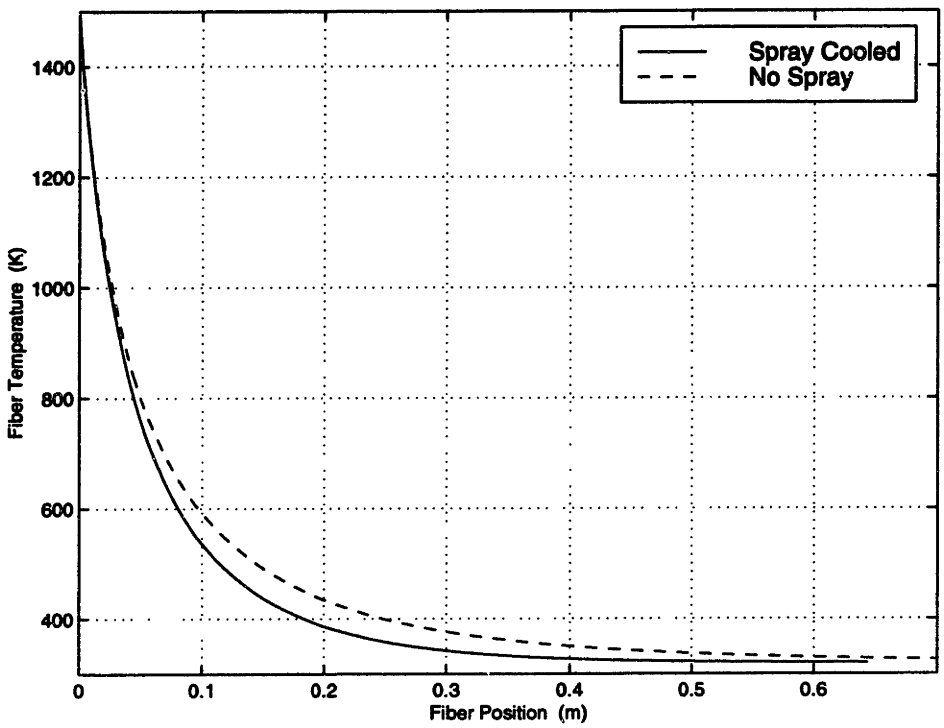

Figure 8.15: Fiber temperature profile for 5 μm fiber at 50 m/sec.

8.3 Conclusions

The following conclusions can be made from the spray cooling model developed in the preceding chapters.

- Bulk specific heat and evaporation effects make the air temperature more uniform across the fiber bundle.
- For a 10 μm fiber being drawn at 60 m/sec, spray cooling reduces the fiber temperature at 1 m from the bushing plate from 450 K to 360 K. This is for an ambient temperature of 320 K, a spray density of 5000 $drops/cm^3$, and a spray Sauter mean diameter of 70 μm.
- The majority of the evaporation in the boundary layer takes place around the outer edge.
- Changes in ambient air temperatures over the first 20 cm of fiber do not affect the fiber temperature profile.
- The initial fiber temperature does not affect the fiber temperature profile beyond 80 cm from the

bushing plate when the fibers are spray cooled.

- Where the spray comes in contact with the fiber boundary layer does not have a large effect on the temperature profile for fiber positions more than 20 *cm* from the point of spray contact.
- The spray increases the rate of heat transfer from the fiber by decreasing the thickness of the thermal boundary layer.
- The additional cooling obtained from the spray is achieved over a fairly short fiber length. The spray can be removed from the boundary layer after this distance without strongly affecting the fiber temperature profile.
- The degree of spray cooling depends on the fiber configuration. Less cooling is achieved with smaller higher speed fibers than for larger, slower fibers.

The spray cooling model suggests that there is an optimal spray configuration that will provide maximum cooling and still allow for drying of the fibers before the surfactant is applied. The main parameters that can be used to modify the fiber temperature profile are the spray density, droplet diameter distribution and the point of contact of the spray with the boundary layer. These variables are functions of spray nozzle type, operating pressure, and nozzle placement. The spray density and point of contact are also strongly affected by the bulk air motion induced by the high velocity fiber bundle. The model developed in this report can be combined with information about spray distributions within fiber bundles and with specific spray nozzle performance data. All this information can then be used to optimize nozzle types, operating pressures, nozzle placement and external air ducting with the objective of providing optimal fiber cooling while still reducing the amount of water on the fibers at the surfactant applicator.

Bibliography

[1] A.H. Lefebvre. *Atomization and Sprays.* Hemisphere Publishing Corporation, New York, 1989.

[2] C.P. Mao and S.G. Cheuch. Numerical analysis of pressure swirl atomizers. *Proceedings of the Fifth International Conference on Liquid Atomization and Spray Systems*, pages 225 – 232, 1991.

[3] N. Tokuoka, Y. Yamaguchi, M. Takada, and F. Zhang. The spray structure from swirl atomizers (part 1:general structure of the spray). *Proceedings of the Fifth International Conference on Liquid Atomization and Spray Systems*, pages 233 – 240, 1991.

[4] A.J. Yule and J.J. Chinn. Swirl atomizer flow: Classical inviscid theory revisited. *Proceedings of the Sixth International Conference on Liquid Atomization and Spray Systems*, 1994.

[5] C.F. Edwards and K.D. Marx. Application of poisson statistics to the problem of size and volume flux measurement by phase-doppler anemometry. *Proceedings of the Fifth International Conference on Liquid Atomization and Spray Systems*, pages 653 – 660, 1991.

[6] H.C. Lewis, D.G. Edwards, M.J. Goglia, R.I. Rice, and L.W. Smith. Atomization of liquids in high velocity gas streams. *Ind. Eng. Chem.*, 40(1):67 – 74, 1948.

[7] T. Nonn and P. Haugen. Uncertainties in phase doppler measurements of sprays. *Proceedings of the Sixth International Conference on Liquid Atomization and Spray Systems*, pages 467–474, 1994.

[8] L.E. Drain. *The Laser Doppler Technique.* John Wiley and Sons, New York, 1980.

[9] M.B. Glauert and M.J. Lighthill. The axisymmetric boundary layer on a long thin cylinder. *Proc. R. Soc.*, A320:188–203, 1955.

[10] B.C. Sakiadis. Boundary-layer behavior on continuous solid surfaces: III. The boundary layer on a continuous cylindrical surface. *A.I.Ch.E. Journal*, 7(3):467–472, 1961.

[11] D.E. Bourne and D.G. Elliston. Heat transfer through the axially symmetric boundary layer on a moving circular fibre. *Int. J. Heat Mass Transfer*, 13:583 – 593, 1970.

[12] B.C. Sakiadis. Boundary-layer behavior on continuous solid surfaces: II. The boundary layer on a continuous flat surface. *A.I.Ch.E. Journal*, 7(2):221–225, 1961.

[13] Richard E. Sayles. Approximate solution for the viscous boundary layer on a continuous cylinder. *A.I.Ch.E. Journal*, 36(12):1917–1919, 1990.

[14] Eckard Beese and Klaus Gerten. Skin friction and heat transfer on a circular cylinder moving in a fluid at rest. *Journal of Applied Mathematics and Physics*, 30:117–127, 1979.

[15] D.E. Bourne and D.R. Davies. Heat transfer through the laminar boundary layer on a circular cylinder in axial incompressible flow. *Quart. Journ. Mech. and Applied Math*, 11:52–66, 1958.

[16] L.R. Glicksman. The cooling of glass fibres. *Glass Technology*, 9(5):131–138, 1968.

[17] J. Gould and F.S. Smith. Air-drag on syntheic-fibre textile monofilaments and yarns in axial flow at speeds up to 100 metres per second. *J. Text. Inst.*, 1, 1980.

[18] E. Richelle, R. Tasse, and M.L. Riethmuller. Momentum and thermal boundary layer along a slender cylinder in axial flow. *Int. J. Heat and Fluid Flow*, 16(2):99–105, 1995.

[19] H. Papamichael and I.N. Miaoulis. Axial heat conduction effect in the cooling of optical fibres. *Glass Technology*, 32(3):102 – 108, 1991.

[20] D.E. Bourne and H. Dixon. The cooling of fibres in the formation process. *Int. J. Heat Mass Transfer*, 24:1323 – 1332, 1971.

[21] Kenneth Jr. Wark. *Tables and Figures to Accompany Thermodynamics.* McGraw-Hill Publishing Co., New York, 1988.

[22] Michael F. Modest. *Radiative Heat Transfer.* McGraw-Hill, Inc., New York, 1993.

[23] Samuel N. Rea. Rapid method for determining concentric cylinder radiation view factors. *AIAA*, 13(8):1122–1123, 1975.

[24] A.F. Mills. *Heat and Mass Transfer.* Irwin, Chicago, 1995.

Appendix A

MAPLE V Code Description

Due to poor documenting capabilities within MAPLE V code, this section will describe in detail the program written to solve for the fiber temperature profile. Each section below corresponds with a section from the code.

A.1 Declare Initial Parameter Values

The first section declares the constants that describe the physical system and are the main controls for adapting the simulation to match physical systems. Table A.1 lists the variables that are declared in this section.

A.2 Define Array Structures

This section declares the array structures used to store evaluated data. Two different size arrays are declared. *Xunaff* and *Tunaff* are both declared to a length of 701 elements. These arrays are used to store position and temperature data for the no spray analysis. All remaining variables are declared to a length of 2761 elements. These arrays are listed in Table A.2. The constants A_1, B_1, and C_1 are used in the polynomial estimation of k_{evap}. Initial values for the first 5 values in the arrays are declared. This must be done due to the presence of the series expansion of β for initial values of α. No temperature or position change is

nospray	- sets initial point of contact of spray with boundary layer (divide by 100 to find α value for initial spray contact)
Tenv	- environmental (bulk) air temperature (K)
n[o]	- spray density ($drops/m^3$)
rho[w]	- water density (kg/m^3)
rho[f]	- fiber density (kg/m^3)
Cp[f]	- fiber specific heat ($J/kg\ K$)
rad	- fiber radius (m)
U	- fiber velocity (m/sec)
Ti	- initial fiber temperature (K)
sigma	- Prandlt number
SMDO	- Sauter mean diameter - initial drop diameter (m)
hfg	- latent heat of vaporization (J/kg)
rho[a]	- air density at Ti (kg/m^3)
Cp[a]	- air specific heat at Ti ($J/kg\ K$)
epsilon	- glass fiber emissivity
sig	- Boltzman's constant ($5.67 * 10^{-8}\ W/m^2K^4$)
Tbp	- bushing plate temperature (K)
spoff	- distance below which no spray is in fiber boundary layer (m)
top	- *for* loop parameter to reduce iteration length

Table A.1: Computer model input variables.

x[ ]	- fiber position
T[ ]	- fiber temperature
falpha[ ]	- velocity profile parameter
fbeta[ ]	- temperature profile parameter
evap[ ]	- evaporation integral
hcon[ ]	- convective heat transfer coefficient
hrad[ ]	- effective radiation heat transfer coefficient

Table A.2: Data arrays.

assumed over these initial values, and they are effectively just null place holders.

A.3 Series Expansion

This section contains the series expansion for evaluation of β for values of α less than .08. The output from this section is used as initial conditions on $d\beta/d\alpha$. The initial values are set as *alphaini* and *betaini*.

A.4 Define Differential Equation

This section defines the differential equation $d\beta/d\alpha$ for the no spray analysis, with the initial conditions from the series expansion. The method of evaluation can be changed by modifying the

$$type = numeric$$

command in the declaration line. This form invokes a Fehlberg fourth-fifth order Runge-Kutta method. Other differential equation solution methods are available in MAPLE. To obtain more information on the different methods type *? dsolve* at the command prompt. The differential solution is assigned the call sequence $F(\alpha)$.

A.5 No Spray Solution

This section contains the *for* loop used to solve for the no spray fiber temperature profile. *Tref* is the average film temperature that is used to evaluate variable air properties. *Ei* calls the exponential integral function and *gamma* is defined as Euler's constant. At a number of points within the *for* loop, numeric evaluation of equations must be forced using the *evalf(")* command. Unless otherwise directed, MAPLE V will not evaluate symbolic variables such as e^2 or γ unless specifically directed to do so. This can result in array variables that are defined by past array variables to take on forms with 100 plus elements if numeric evaluation is not forced on each iteration of the loop.

A.6 Spray Solution

In the *for* loop declaration, the initial point is automatically set be the value of *nospray* set at the beginning of the program. The final value of the loop is set by the constant *top* and is adjustable from a minimum of *nospray* to a maximum of 2760. This value can be change to make the program more efficient. Depending on the fiber size, speed, etc., the α range over which the temperature profile must be calculated can change. For the most efficient use of computational time, set the value of *top* such that it calculates the temperature profile only for the length of interest. It will take some iteration to find the best value for each particular fiber configuration, but should remain fairly constant for variations in spray and air properties.

A.7 Evaluation of Evaporation Term

The evaporation integral is evaluated using an adaptive Newton-Cotes numerical method. If another method of calculation is desired, simply change *NCrule* to the method desired. A description of the other methods available in MAPLE V can be found by typing *? Int(numeric)* at a command prompt. As stated in the main report, the digit control (number before *NCrule*) can be modified to increase or decrease accuracy. If problems are encountered with the numerical integration, try decreasing the digit number. The conditional statement right after the numerical integration is used to stop evaporative cooling in the boundary layer after the set point *spoff*. This enables the program to simulate spray cooling over a narrow region of fiber length.

A.8 Evaluation of β

The next conditional statement is used to declare the differential equation $d\beta/d\alpha$ depending on the relative thickness of the thermal and velocity boundary layers. Once the next β value has been calculated, the temperature change in the fiber is evaluated in the same way as for the no-spray analysis.

xunaff.dat	- position data for no-spray cooling
Tunaff.dat	- temperature data for no-spray cooling
x.dat	- position data for spray cooling
T.dat	- temperature data for spray cooling
evap.dat	- evaporation integral evaluation
beta.dat	- temperature profile coefficient
alpha.dat	- velocity profile coefficient

Table A.3: Ouput data structure.

A.9 Define Remaining Array Values

This final *for* loop is used to fill out the data arrays. Depending on the value of *top*, the data arrays will contain null spaces at the end that will cause problems when trying to plot the data or when writing the data to a file. By filling in these remaining values, the data arrays can be declared to the same length each run, but computations only need to be performed over the interval of interest. This limits the required modifications of the code for different runs, but permits greater flexibility. Also in this section, the data is written to secondary arrays that MAPLE can use to generate plots and also write the data to external data files that can be read and analyzed using other programs. The data arrays that are written are listed in Table (A.3). These data files will be written to the computer's hard disk. Which directory these files end up in, depends on the configuration of each particular system.

Appendix B

MAPLE V Program

The following is the program used to calculate the fiber temperature profile. The program is written for MAPLE V Release 4. Full desciptions of the various parts and variable definitions are given in Appendix A.

```
Glass Fiber Spray Cooling Model Simulation
```

Matthew Sweetland - Massachusetts Institute of Technology

Rohsenow Heat Transfer Laboratory

Prepared for PPG Industries Inc.

```
> restart;
> with(linalg):
Declare initial parameter values
> nospray:=500;Tenv:=320;n[o]:=5000*100^3;rho[w ]:=989;
> rho[f]:=2562;Cp[f]:=1519;rad:=5*10^(-6);U:=60 ;Ti:=1500;sigma:=.69;
> SMD0:=70*10^(-6);
> hfg :=2389000;rho[a]:=.354;Cp[a]:=1130;
> BP:=.3;epsilon:=.3;sig:=5.6698*10^(-8);Tbp:=1 500;
> spoff:=2;top:=2100;
Define array structures
> x:=array(1..2761);T:=array(1..276i):
```

```
> falpha:=array(1..2761):fbeta:=array(1..2761):
> evap:=array(1..2761):xunaff:=array(1..701):Tu naff:=array(1..701):
> hcon:=array(1..2761);hrad:=array(1..2761);
> A1:=.00000146590746*10^(-7);B1:=.000047634290 81*10^(-7)
> ;C1:=-.14406585960386*10^(-7);
> T[1]:=Ti:T[2]:=Ti:T[3]:=Ti:T[4]:=Ti:T[5]:=Ti
> :Tunaff[1]:=Ti:Tunaff[2]:=Ti:Tunaff[3]:=Ti
> :Tunaff[4]:=Ti:Tunaff[5]:=Ti:Trad[1]:=Ti
> :Trad[2]:=Ti:Trad[3]:=Ti:Trad[4]:=Ti:
> Trad[5]:=Ti:evap[1]:=0:evap[2]:=0:evap[3]:=0:  evap[4]:=0:evap[5]:=0
> :falpha[1]:=0:falpha[2]:=0:falpha[3]:=0:falph a[4]:=0:falpha[5]:=0:
> hcon[1]:=0:hcon[2]:=0:hcon[3]:=0:hcon[4]:=0
> :hcon[5]:=0:hrad[1]:=0:hrad[2]:=0
> :hrad[3]:=0:hrad[4]:=0:hrad[5]:=0:
> x[1]:=0:x[2]:=0;x[3]:=0:x[4]:=0:xunaff[1]:=0
> :xunaff[2]:=0;xunaff[3]:=0:xunaff[4]:=0:
```

Series expansion

```
> eta := rho[a]*Cp[a]/rho[f]/Cp[f]:
> a1:=1/3*(sigma+2)/sigma:
> a2:=((sigma-1)*(sigma+2)+6*eta)/(9*sigma*(sig ma+1)):
> a3p:=((sigma-1)*(sigma+2)*(3*sigma^2-4*sigma- 2)
> +60*(3*sigma^2+sigma+2)*eta+360*eta^2):
> a3:=a3p/(270*(sigma+1)^2*(3*sigma+2)):
> matrix(4,1,beta):
> i:=1:for alpha1 from .02 by .02 to .08
> do fbeta[i]:=a1*alpha1 + a2*alpha1^2 + a3*alpha1^3:
> falpha[i]=alpha1:
> i:=i+1:  od:
```

```
> alphaini:=alpha1-.02;

> betaini:=fbeta[4];
```

Define differential equation

```
> eqn1 :=dbeta/dalpha*(2/sigma -1 +

> (dalpha-dbeta)*(dalpha*exp(dalpha) - sinh(dalpha))

> /(dalpha*cosh(dalpha) - sinh(dalpha))) +

> 2*eta*exp(dalpha)/sigma/dalpha^2*((1+dbeta)*sinh(dalpha)

> -dalpha*cosh(dalpha) - dalpha* dbeta*exp(-dalpha));

> aF:=dsolve({diff(dbeta(dalpha),dalpha)

> = eqn1,dbeta(alphaini)=betaini},dbeta(dalpha),

> type=numeric, output = listprocedure);

> F:=subs(aF,dbeta(dalpha)):
```

No spray solution

```
> for i from 5 to 700

> do

> alpha:=i*.01+.04;falpha[i]:=alpha;

> Tref:=(T[i-1]-Tenv)/2 + Tenv;

> nu:=(6.233484448*10^(-5)*(Tref)^2 +

> .06474918445028*Tref-10.06637883213627)*10^(-6):

> temp:=(U*rad^2/2/nu)*((exp(1)^(2*alpha)-1)/al pha

> - Ei(2*alpha)+ln(2*alpha) +gamma-2);

> x[i]:=evalf('):xunaff[i]:=x[i]:

> rho[a]:=8.5*10^(-13)*((Tref)^4)-4.37119*10^(- 9)*((Tref)^3)

> +8.21348630*10^(-6)*((Tref)^2) -

> 6.92623*10^(-3)*(Tref)+2.6094279:

> Cp[a]:=1.6*10^(-10)*(Tref)^4 - 7.7437*10^(-7)*(Tref)^3

> +1.2404*10^(-3)*(Tref)^2- .58086*Tref + 1088.37:

> keff:=-5.53047*10^(-9)*(T[i-1])^2+6.4535*10^( -5)*T[i-1]+.0080407;
```

```
> eta := rho[a]*Cp[a]/rho[f]/Cp[f];
> fbeta[i]:=F(alpha);
> deltaTx:= 2*keff/fbeta[i]/rho[f]/Cp[f]/rad^2/U*(T[i-1] - Tenv);
> qradenv:=epsilon*sig*(T[i-1]^4 - Tenv^4)*2*Pi*rad*(x[i] - x[i-1]);
> hcon[i]:=keff/rad/fbeta[i];
> hrad[i]:=epsilon*sig*(T[i-1]^4 - Tenv^4)/(T[i-1]-Tenv);
> deltrad:=(-qradenv)/rho[f]/Cp[f]/rad^2/U/Pi:
> evap[i]:=0;
> temp:=T[i-1] - deltaTx*(x[i]-x[i-1])
> +deltrad;T[i]:=evalf(");Tunaff[i]:=T[i-1];
> od
> :
```

Spray solution

```
> readlib(unassign):
> unassign('eqn1');unassign('aF');unassign('eta ');
> unassign('F');unassign('keff');
> asum:=(((nospray*.01)+.04)-nospray*.001);
> count:=0;
> for i from (nospray+1) to top
> do
> alpha:=i*.001+asum:falpha[i]:=alpha:
> Tref:=(T[i-1]-Tenv)/2 + Tenv;
> nu:=(6.233484448*10^(-5)*(Tref)^2 +
> .06474918445028*Tref-10.06637883213627)*10^(- 6):
> temp:=(U*rad^2/2/nu)*((exp(2*alpha)-1)/alpha -
> Ei(2*alpha)+ln(2*alpha) +gamma-2):
> x[i]:=evalf("):
> rho[a]:=8.5*10^(-13)*((Tref)^4)-4.37119*10^(- 9)*((Tref)^3)
```

```
> +8.21348630*10^(-6)*((Tref)^2) - 6.92623*10^(-3)*(Tref)+2.6094279:
> Cp[a]:=1.6*10^(-10)*(Tref)^4 - 7.7437*10^(-7)*(Tref)^3
> +1.2404*10^(-3)*(Tref)^2- .580861*Tref + 1088.47:
> keff:=-5.53047*10^(-9)*(T[i-1])^2+6.4535*10^( -5)*T[i-1]+.0080407:
> eta := rho[a]*Cp[a]/rho[f]/Cp[f]:
> thetat:=T[i-1]-Tenv:
> beta:=fbeta[i-1];
> theta[f]:=T[i-1]-Tenv:
> alpha:=falpha[i]:
> deltax:=x[i]-x[i-1];diffx:=.00001;
```

Evaluation of evaporation term

```
> delta:=rad*(exp(beta)-1);Ty:=Tenv+thetat*(1-1 /beta*ln(1+y/rad));
> u:=(U-U/alpha*ln(1+y/rad));k:=A1*Ty^2+B1*Ty+C 1;total:=
> Pi/4*n[o]*hfg/(rad*(exp(alpha)-1))*rho[w]
> *(SMDO^2-k*diffx/u)^(1/2)*(rad+y)*y*(-k);
> evapt:=evalf(Int(total,y=0..(delta),3,_NCrule ));
> evapt2:=evapt*(x[i]-x[i-1])/diffx;
> evap[i]:=evapt;
> dbetini:=fbeta[i-1]:dalphini:=falpha[i-1]:
> unassign('eqn2'):unassign('aF1'):unassign('F1 '):
> unassign('dalpha');unassign('dbeta');
> alpha:=falpha[i];
> if (x[i]>spoff) then
> evapt2:=0;evap[i]:=0;
> fi;
```

Evaluation of beta

```
> if (beta>alpha) then
> eqn2:=2*dbeta/dalpha/sigma + 2*dbeta^2/thetat
```

```
>  /dalpha/keff/sigma*evapt2+eta/dalpha^2/sigma
>  *(exp(2*dalpha)-exp(2*dalpha)*dalpha+
>  exp(2*dalpha)*dbeta-2*dalpha*dbeta-dalpha-1-d beta)
>  -dbeta/dalpha*(2*exp(2*dalpha)*dalpha-
>  2*exp(2*dalpha)*dalpha^2+2*exp(2*dalpha)
>  *dalpha*dbeta-exp(2*dalpha)-exp(2*dalpha)
>  *dbeta+1+dbeta)/(-exp(2*dalpha)
>  +exp(2*dalpha)*dalpha+dalpha+1)
>  :
>  else
>  eqn2:=-2*dbeta*dalpha/sigma*(2*exp(1)^(2*dalp ha)
>  /dalpha-(exp(1)^(2*dalpha)-1)/dalpha^2
>  -exp(2*dalpha)/dalpha+1/dalpha)/(-2*exp(2*dbe ta)
>  *dbeta-2*exp(2*dbeta)*dalpha*dbeta+2*exp(2*db eta)
>  *dbeta^2+exp(2*dbeta)+exp(2*dbeta)*dalpha-dal pha-1)
>  -2*dalpha*dbeta^2/thetat/keff/sigma*(2*exp(1) ^
>  (2*dalpha)/dalpha-(exp(1)^(2*dalpha)-1)/dalph a^2
>  -exp(2*dalpha)/dalpha+1/dalpha)/(-2*exp(2*dbe ta)
>  *dbeta-2*exp(2*dbeta)*dalpha*dbeta+2*exp(2*db eta)
>  *dbeta^2+exp(2*dbeta)+exp(2*dbeta)*dalpha-dal pha-1)
>  *evapt2+eta/sigma*(-exp(2*dbeta)-exp(2*dbeta)
>  *dalpha+exp(2*dbeta)*dbeta+2*dalpha*dbeta
>  +dalpha+1+dbeta)*(2*exp(1)^(2*dalpha)/dalpha
>  -(exp(1)^(2*dalpha)-1)/dalpha^2-exp(2*dalpha)
>  /dalpha+1/dalpha)/(-2*exp(2*dbeta)*dbeta-
>  2*exp(2*dbeta)*dalpha*dbeta+2*exp(2*dbeta)
>  *dbeta^2+exp(2*dbeta)+exp(2*dbeta)*dalpha-dal pha-1)
>  +dbeta/dalpha*(-exp(2*dbeta)+exp(2*dbeta)
>  *dbeta+1+dbeta)/(-2*exp(2*dbeta)*dbeta-
```

```
> 2*exp(2*dbeta)*dalpha*dbeta+2*exp(2*dbeta)
> *dbeta^2+exp(2*dbeta)+exp(2*dbeta)*
> dalpha-dalpha-1)
> :
> fi;
> aF1:=dsolve({diff(dbeta(dalpha),dalpha) =
> eqn2,dbeta(dalphini)=dbetini},dbeta(dalpha)
> , type=numeric, output = listprocedure):
> F1:=subs(aF1,dbeta(dalpha)):
> fbeta[i]:=F1(alpha);
> beta:=fbeta[i]:
> theta[f]:=T[i-1]-Tenv;beta:=fbeta[i]:
> deltaTx:= 2*keff/fbeta[i]/rho[f]
> /Cp[f]/rad^2/U*(T[i-1] - Tenv):
> xnext:=x[i];
> qradenv:=epsilon*sig*(T[i-1]^4
> - Tenv^4)*2*Pi*rad*(deltax);
> deltrad:=(-qradenv)/rho[f]/Cp[f]/rad^2/U/Pi:
> temp3:=T[i-1]-deltaTx*(deltax)+deltrad:
> temp4:=evalf(");T[i]:=temp4:
> hrad[i]:=epsilon*sig*
> (T[i-1]^4 - Tenv^4)/(T[i-1]-Tenv);
> hcon[i]:=keff/rad/fbeta[i];
> count:=count+1;
> od
> :
```

Define remaining array values

```
> for i from top to 2760
```

```
> do x[i+1]:=x[i]+.001:T[i+1]:=T[i];
> Trad[i+1]:=Trad[i];hrad[i+1]:=hrad[i];
> hcon[i+1]:=hcon[i];evap[i+1]:=evap[i];
> fbeta[i+1]:=fbeta[i];falpha[i+1]:=falpha[i];o d:
> xunaff[701]:=xunaff[700]+.001;
> Tunaff[701]:=Tunaff[700];
> result[air]:=augment(xunaff,Tunaff):
> result[evap]:=augment(x,T):
> with(plots):with(plottools):
> ap:=listplot(result[air],title='Radiation Model'):
> ep:=listplot(result[evap],linestyle=4):
> display({ap,ep},
> view = [0..(2),300..1500],abels=[Position, Temperature]);
> result[xunaff]:=augment(xunaff):
> result[x]:=augment(x):
> result[Tunaff]:=augment(Tunaff):
> result[T]:=augment(T):
> result[evap]:=augment(evap):
> result[beta]:=augment(fbeta):
> result[alpha]:=augment(falpha):
> writedata('xunaff.dat',result[xunaff],float);
> writedata('x.dat',result[x],float);
> writedata('T.dat',result[T],float);
> writedata('Tunaff.dat',result[Tunaff],float);
> writedata('evap.dat',result[evap],float);
> writedata('beta.dat',result[beta],float);
> writedata('alpha.dat',result[alpha],float);
> x[nospray];
```

Appendix C

Order of Magnitude Estimate for Solution of Temperature Profile

An estimate of the order of magnitude of the last term in equation (5.12) is needed to see if the term can be neglected compared to 1/3. The term is

$$\frac{\beta a^4}{6\rho C_p k \Theta_f} \frac{\partial}{\partial y} \dot{q}_e \Big|_{y=0} \tag{C.1}$$

The initial part of equation (C.1) is easy to calculate using representative values. Evaluating air properties at $T_e = 350\ K$ yields $\rho = 1.012\ kg/m^3$, $C_p = 1007\ J/kgK$, and $k = .0300\ W/mK$. Using a low value for the fiber temperature defect $\Theta_F = 100\ K$, and for a 10 μm diameter fiber moving at 60 m/sec with $\beta \sim 7$, then

$$\frac{\beta a^4}{6\rho C_p k \Theta_f} = 2.4 * 10^{-25} \tag{C.2}$$

Evaluation of the partial fraction in equation (C.1) takes somewhat more effort. Differentiating both sides of equation (6.24) with respect to y and substituting $k_{evap} = A_1 T(y)^2 + B_1 T(y) + C_1$ yields

$$2\pi(a+y)\dot{q}_e\Delta x = -\frac{\pi^2 h_{fg} n_0 \rho_w y(a+y)}{2\delta} k_{evap}\left[D_0^2 - \frac{k_{evap}\Delta x}{u(y)}\right]^{\frac{1}{2}}\Delta x \tag{C.3}$$

which can be solved for $\dot{q}_e$ to obtain

$$\dot{q}_e = -\frac{\pi h_{fg} n_0 \rho_w y}{4\delta} k_{evap}\left[D_0^2 - \frac{k_{evap}\Delta x}{u(y)}\right]^{\frac{1}{2}}. \tag{C.4}$$

Taking the partial differential of equation (C.4) with respect to y produces

$$\begin{aligned}\frac{\partial}{\partial y}\dot{q}_e = &-\frac{\pi h_{fg} n_0 \rho_w}{4\delta} k_{evap}\left[D_0^2 - \frac{k_{evap}\Delta x}{u(y)}\right]^{\frac{1}{2}} - \frac{\pi h_{fg} n_0 \rho_w y}{4\delta}\frac{\partial k_{evap}}{\partial y}\left[D_0^2 - \frac{k_{evap}\Delta x}{u(y)}\right]^{\frac{1}{2}} \\ &- \frac{\pi h_{fg} n_0 \rho_w y}{4\delta} k_{evap}\frac{1}{2}\left[D_0^2 - \frac{k_{evap}\Delta x}{u(y)}\right]^{-\frac{1}{2}}\left[-\frac{\partial k_{evap}}{\partial y}\frac{\Delta x}{u(y)} - \frac{k_{evap}}{u(y)^2}\frac{\partial u}{\partial y}\right]\end{aligned} \tag{C.5}$$

As long as the partial derivatives in the last two terms of this equation evaluate without a y in the denominator, then these terms will drop out when equation (C.5) is evaluated at $y = 0$. Expanding the partial differentials:

$$\frac{\partial k_{evap}}{\partial y} = \frac{\partial}{\partial y}\left(A_1 T(y)^2 + B_1 T(y) + C_1\right) = 2A_1 T(y)\frac{\partial T}{\partial y} + B_1\frac{\partial T}{\partial y} \tag{C.6}$$

where $\partial T/\partial y$ is evalated as

$$\frac{\partial T}{\partial y} = \frac{-\Theta_f}{a\beta}\frac{1}{\left(1+\frac{y}{a}\right)} \tag{C.7}$$

and the partial derivative of $u(y)$ can be similarly computed as

$$\frac{\partial u}{\partial y} = \frac{-U}{a\alpha} \frac{1}{\left(1 + \frac{y}{a}\right)} \tag{C.8}$$

Substituting these equations into equation (C.5) and evaluating at $y = 0$ yields a simplified equation of the form

$$\frac{\partial}{\partial y} \dot{q}_e \Big|_{y=0} = -\frac{\pi h_{fg} n_0 \rho_w}{4\delta} k_{evap} \left[D_0^2 - \frac{k_{evap} \Delta x}{u(y)} \right]_{y=0}^{\frac{1}{2}} \tag{C.9}$$

At $y = 0$, $u(y) = U = 60\ m/sec.$ Take $\Delta x = .01\ m$, and $D_0 = 70\ \mu m$. From Figure 6.1, the value of $k_{evap} \sim 3 * 10^{-7}\ m^2/sec.$ Using $h_{fg} = 2316000\ J/kg$, $n_0 = 5000\ drops/cm^3 = 5 * 10^9\ drop/m^3$, $\rho_w = 999\ kg/m^3$, and $\delta = 1\ mm$, then

$$\frac{\partial}{\partial y} \dot{q}_e \Big|_{y=0} \sim -2.0 * 10^{11}. \tag{C.10}$$

This value may seem large, but remember, it is the second part of equation (C.1), which can now be evaluated to

$$\frac{\beta a^4}{6\rho C_p k \Theta_f} \frac{\partial}{\partial y} \dot{q}_e \Big|_{y=0} = 2.4 * 10^{-25} \ * \ -2.0 * 10^{11} = -4.8 * 10^{-14}. \tag{C.11}$$

This value is much less than 1/3, and can be neglected.

THESIS PROCESSING SLIP

FIXED FIELD: ill. _____ name _____

index _____ biblio _____

▶ COPIES: (Archives) Aero Dewey (Eng) Hum

Lindgren Music Rotch Science

TITLE VARIES: ▶☐ _____

NAME VARIES: ▶☐ _____

IMPRINT: (COPYRIGHT) _____

▶ COLLATION: 147 l.

▶ ADD: DEGREE: _____ ▶ DEPT.: _____

SUPERVISORS: _____

NOTES:

cat'r: date:

page:

▶ DEPT: M. E. ▶ J134

▶ YEAR: 1998 ▶ DEGREE: ~~M.~~ S.M.

▶ NAME: SWEETLAND, Matthew